Australian Government
Department of Defence
Defence Science and
Technology Organisation

Survivability of a Propellant Fire inside a Simulated Military Vehicle Crew Compartment: Part 1 - Baseline Study

Andrew H. Hart, Blair C. Lade and Garry R. Hale

Weapons and Countermeasures Division
Defence Science and Technology Organisation

DSTO-RR-0392

ABSTRACT

A number of combat vehicles carry their propelling charges and high explosive filled projectiles inside the crew compartment. Such arrangements give rise to questions about the prospects of crew survival in an unplanned munitions initiation event owing to co-habitation of the crew with an on-board magazine. DSTO has undertaken an experimental study to investigate this concern. A trials structure was developed whereby a range of propelling charge types and storage configurations were initiated in a simulated military vehicle crew compartment. The trials structure was fitted out with simulated personnel instrumented to enable the threats from the thermal, ejecta and pressure environment created by the propelling charge event to be assessed. The trial results indicated that the thermal and ejecta threats posed the greatest risk to crew survival. The effectiveness of a range of hazard mitigation techniques was also assessed and this is addressed in *Part 2* of this report.

Published by

Weapons Systems Division
DSTO Defence Science and Technology Organisation
PO Box 1500
Edinburgh South Australia 5111 Australia

Telephone: 1300 DEFENCE
Fax: (08) 7389 6567

AR-015-620
June 2013

APPROVED FOR PUBLIC RELEASE

Survivability of a Propellant Fire inside a Simulated Military Vehicle Crew Compartment: Part 1 - Baseline Study

Executive Summary

A number of combat vehicles carry their propelling charges and high explosive filled projectiles inside the crew compartment. To permit the provision of informed advice on future acquisition programs, the Capability Development Group tasked DSTO to investigate the prospects of crew survival in the event of an unplanned munitions initiation event owing to the co-habitation of the crew with an on-board magazine. After initial modelling work indicated that a propelling charge fire would indeed subject the crew to a hazardous and potentially life-threatening environment, a trial was conducted in mid-2010 to experimentally ascertain the survivability of the crew when exposed to such an event.

A trials structure was developed whereby a propelling charge fire was initiated in a simulated military vehicle crew compartment, and simulated personnel were instrumented with a range of heat flux gauges and pressure sensors. This data was then fed into models to predict burn levels and intrathoracic overpressure effects. Threats to crew personnel from ejecta were also investigated.

Three propelling charge module types in four different module configurations were tested over the course of the trial and it is these experiments that are the focus of *Part 1* of this report. A range of hazard mitigation techniques were also assessed in the trial. These included: the use of a MIL-STD automatic fire suppression system; personnel clothing configurations; and propelling charge storage tube confinement modification. *Part 2* of this report addresses the effectiveness of these hazard mitigation strategies.

The trial results indicated that the thermal and ejecta threats posed the greatest risk to crew survival. In the absence of a fire suppression system, a single propelling charge storage tube event will create a thermal environment that will cause severe respiratory and skin burn damage with a minimal probability of survival and will also pose a sympathetic cook-off risk for other stored munitions in the crew compartment. Ejecta in the form of unburnt propellant grains and/or propelling charge modules posed a life threatening risk to crew for all baseline tests conducted using a storage tube configuration considered representative of that used in a representative military vehicle. While the generated pressure in the crew compartment was found to pose a hazard in certain instances, it was secondary to the thermal and ejecta effects.

An evaluation of the suitability of widely used skin burn damage heuristics, which are based on time-weighted energy absorption and ambient temperature parameters, was also made using burn damage predictions from the transient heat flux measurements collected over the course of the trial.

This page is intentionally blank

Authors

Andrew H. Hart
Weapons Systems Division

Andrew Hart completed a Bachelor of Engineering (Chemical) degree at the University of Adelaide in 2001. Andrew commenced work for DSTO in 2002 as a member of Weapons Propulsion Group where his work initially focussed on R&D relating to cast-composite rocket motors. The emphasis of his work then shifted to gun propellants, and for the past 8 years he has been involved in a wide range of gun propellant related research activities in support of defence acquisition programs and is currently the DSTO S&T Advisor for JP2086 'Mulwala Redevelopment Project'..

Blair C. Lade
Weapons Systems Division

Blair Lade has been an instrumentation technician for over 40 years and been involved in the many aspects of instrumentation and data recording throughout his career. From earthquake, radiation and process monitoring through to live and studio sound recording, cinema engineering and photography, accuracy, reliability and repeatability have always been the driving forces.

For the last 13 years he has been the instrumentation officer at DSTO's static rocket motor firing site at Edinburgh South Australia and has developed and maintained the instrumentation systems and electronics for the site.

Garry R. Hale
Weapons Systems Division

Garry Hale completed an Associate Diploma in Electronic Systems Maintenance during his 20 years of service in the Royal Australian Navy. He has extensive experience in the support, maintenance, operation, and technical instruction of a variety of electronic systems. Including: missile control systems; gun control systems; Radar; Sonar; and, communications equipment. As such he is familiar with military procedures and requirements on exercise and in warlike operational zones. Since 2005 he has been working as a research assistant and technical officer for DSTO. He is currently studying a Bachelor of Science at the University of South Australia.

Contents

Nomenclature

A	Area (m^2)
AFESS	Automatic Fire Suppression System
ASII	Adjusted Severity of Injury Index
ATC `	Alternative top zone propelling charge module
B	Burn level pre exponential constant (s^{-1})
BCM	Bottom zone propelling charge module
BCS	Sodium bicarbonate, $NaHCO_3$
C	Empirical constant
C_p	Specific heat at constant pressure (J/kg.K)
CWV	Chest wall velocity (m/s)
D	Projectile diameter (cm)
ΔE	Activation energy for skin (J/mole)
e	Thermal effusivity ($J/m^2.K.s^{0.5}$)
F	Radiation shape factor
FM200	1,1,1,2,3,3,3-heptafluoropropane, C_3F_7H. Also called HFC-227ea.
Fo	Fourier number
G	Blood perfusion rate ($m^3/s/m^3$ tissue)
Gr	Grashof number
g	Gravity (m/s^2)
HE	High explosive
HF	Hydrogen fluoride
HFS	Omega HS-4 heat flux sensor
h	Heat transfer coefficient
J	Damping coefficient (N.s/m)
K	Spring constant (N/m)
k	Thermal conductivity (W/m.K)
L	Length (m)
LOAEL	Lowest Observable Adverse Effect Level
M	Mass (kg)
m	Empirical constant
n	Empirical constant
Nu	Nusselt number
P	Pressure (kPa)
Pr	Prandtl number
q″	Heat flux (W/m^2)
R	Universal gas constant (J/mole.K)
RH	Relative humidity
RHS	Rectangular Hollow Section
t	Time (s)
T	Temperature (K)
T1	Ambient room temperature, roof-height position (K)
T2	Ambient room temperature, mid-height position (K)
T3	Ambient room temperature, floor-height position (K)
TCM	Top zone propelling charge module
UTS	Ultimate tensile strength (MPa)

v	Velocity (m/s)
V	Initial lung volume (m^3)
W	Mass of target, used in Blunt Force Trauma correlation (kg)
x	Skin depth (m)
α	Thermal diffusivity (m^2/s)
Ω	Burn damage parameter
δ	Air gap thickness (m)
ε	Emissivity
σ	Stefan-Boltzmann constant ($W/m^2.K^4$)
γ	Polytropic gas exponent
μ	Viscosity (kg/m.s)
ρ	Density (kg/m^3)

Subscript

c	Core
cond	Conduction
conv	Convection
f	Film
o	Initial
rad	Radiation

1. Introduction

A number of combat vehicle platforms carry their propelling charges and high explosive (HE) filled projectiles inside the crew compartment.

To permit the provision of informed advice on future acquisition programs, the Capability Development Group tasked DSTO to investigate the prospects of crew survival in the event of an unplanned munitions initiation event owing to concerns about the co-habitation of the crew with an on-board magazine.

2. Background

Three propelling charge module types, representative of those used in particular armoured military vehicles, were considered in this study: a top zone propelling charge module (TCM), an alternative top zone propelling charge module (ATC), and a bottom zone propelling charge module (BCM). All propelling charge modules considered utilise a combustible case filled with propellant and a centre-core igniter train, see Figure 1. Both the BCM and TCM contain the same propellant formulation and centre-core ignition train design, but the propellant grain geometry and propellant mass is different for the two modules so that required ballistic performance and firing range profiles can be met. Each BCM weighs approximately 2.5 kg, of which 80% by mass is propellant. A single TCM weighs approximately 8.5 kg.

The ATC is a high-zone propelling charge filled with reduced sensitivity propellant and has a centre-core igniter tube assembly consisting of black-powder coated propellant. The ATC is of a comparable mass to a BCM.

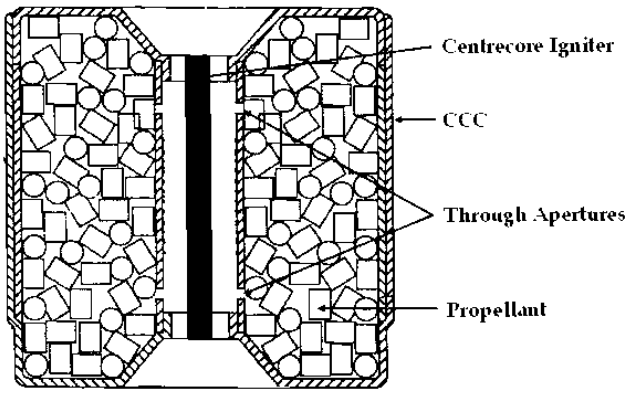

Figure 1: Schematic of a modular charge system representative of that used in the trial

The layout of the hull of a representative armoured vehicle that was simulated in the trial is depicted in Figure 2. Propelling charge storage canisters run along the side walls of the hull, and HE filled projectiles also occupy the hull. A single propelling charge storage canister can hold up to 1xTCM, 3xBCM or 3xATC.

The scope of the present study covers the effect of a propelling charge magazine fire on crew survivability. The effect of unintentional initiation of the HE filled projectiles has not been considered. It was assumed that should projectile initiation occur, the effect on both crew and platform survivability would be catastrophic. Further, the probability of projectile initiation from an external threat will in many threat scenarios be lower than that of the propelling charges. This is, in part, due to the larger presented area of the crew compartment that is occupied by the propellant. However, it is important to note that the environment created by a propelling charge event inside the crew compartment may be such that the sympathetic reaction of other stored munitions, including the HE filled projectiles, is a real possibility.

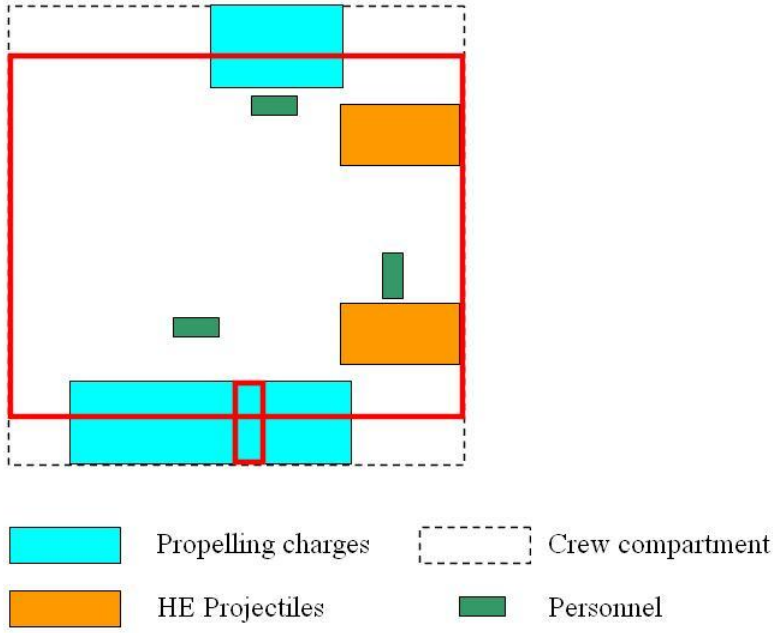

Figure 2: Cross-sectional area of crew compartment simulated in trial (larger red outline), hull ammunition storage locations, and position of the three simulated crew personnel. The position of the storage tube represented in the trial structure is shown with the smaller of the two red outlines.

To address the likelihood of crew survival during a propelling charge fire inside the crew compartment, the following hazards were considered the most relevant:

- Thermal environment
- Pressure environment
- Ejecta in the form of unburnt propellant grains, unconsumed propelling charge modules and/or storage tube fragments and components
- Compartment toxicity

The methods used to quantify the effects of these stimuli on the crew are described in section 3.

Prior to designing the trial, an initial modelling assessment of the thermal and pressure environments generated in the crew compartment from the initiation of a number of propelling charge configurations was performed. A two-phase interior ballistics code jointly developed by DSTO and the University of Queensland, known as *Casbar*, was used for the modelling. The crew compartment was simulated using an axisymmetric geometry of equivalent internal volume [1]. One of the conclusions from the modelling was that the focus of an experimental trial should be on the consequences of a single storage tube event, as the simultaneous initiation of any further munitions would result in an environment where the prospect of survival would be minimal.

3. Hazard Assessment Methodologies

3.1 Thermal

From a survivability perspective, the effect of the thermal environment on the respiratory system and on the level of sustained skin burn damage must be considered.

The skin is made up of three primary layers: the epidermis, which is the outermost layer of the skin; the dermis; and then the hypodermis, which is comprised of subcutaneous fatty tissue (see Figure 3). The thickness of these layers varies from person to person and also with position on the body. A typical range of skin layer thickness is taken from reference [2], and provided in Table 1, along with the physical properties of the skin layers used for skin burn modelling [3].

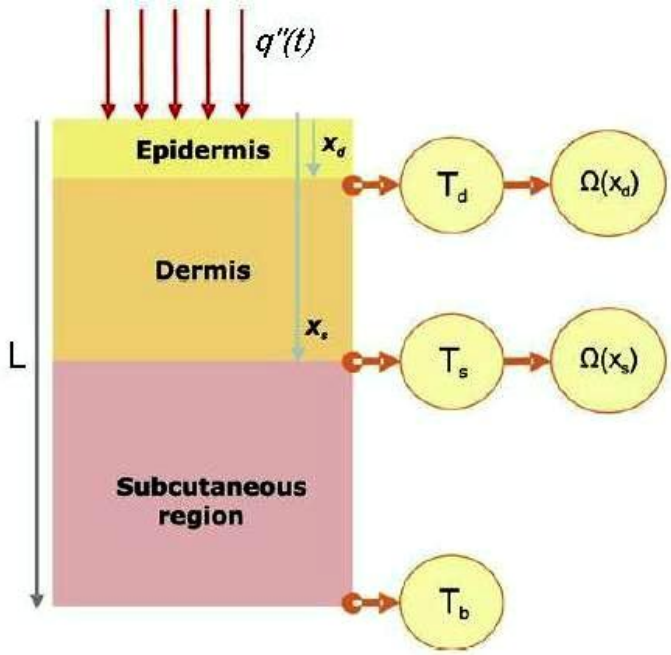

Figure 3: Schematic of skin structure, adapted from [4]

Table 1: Physical properties of the skin used in the burn prediction modelling, the skin thickness in brackets correspond to ranges quoted in the literature.

Parameter	Skin Layer		
	Epidermis	**Dermis**	**Subcutaneous tissue**
Thickness (mm)	0.08 (0.075-0.15)	2 (1-4)	10 (0-20)
ρ (kg/m^3)	1200	1200	1000
k (W/m.K)	0.255	0.523	0.167
C_p (J/kg.K)	3600	3230	2760
		Blood	
G (m^3/s/m^3 tissue)	0	0.00125	0.00125
ρ (kg/m^3)	1060	1060	1060
C_p (J/kg.K)	3770	3770	3770

The interface between the epidermis and dermis is referred to as the basal layer (denoted with subscript *d* in Figure 3), and it is at this interface where second degree burns occur. Third degree burns occur when the dermis is destroyed and the level of burn damage is evaluated at the dermal base (denoted with subscript *s* in Figure 3).

In accordance with ISO 13506 [3], a first order Arrhenius rate proposed by Henriques and Moritz [5] and reproduced in equation (1), was used to model the destruction rate at the basal layer and dermal base. Integrating equation (1) over the time that the skin layer of interest is above 44°C gives the total burn damage, Ω:

$$\frac{d\Omega}{dt} = B\exp\left(-\frac{\Delta E}{RT}\right) \tag{1}$$

$$\Omega = \int B\exp\left(-\frac{\Delta E}{RT}\right)dt \tag{2}$$

Where B and $\frac{\Delta E}{R}$ are skin layer specific kinetic parameters, see Table 2.

First degree burns are said to occur when Ω at the basal layer reaches 0.53 and second degree burns when Ω at the basal layer reaches 1.0. Third degree burns occur when Ω at the dermal base reaches 1.0 [5].

In equations (1) and (2), ISO 13506 [3] recommends using kinetic parameters developed by Stoll and Chianta [6] for the epidermal layer, and the parameters developed by Takata [7] for the dermal and subcutaneous layers. These kinetic parameters are summarised in Table 2.

Table 2: Kinetic parameters used in burn damage calculations

Skin layer	Skin T (°C)	Kinetic Parameter	
		B (s^{-1})	$\Delta E/R$ (K)
Epidermis	<50	2.185×10^{124}	93534.9
	>50	1.823×10^{51}	39109.8
Dermis/subcutaneous	<50	4.32×10^{64}	50000
	>50	9.39×10^{104}	80000

Application of equation (2) requires that the temperature-time profile of the skin at the basal layer and dermal base is known. Mathematical models of heat transfer in the skin assume a transient one-dimensional heat transfer condition. The general equation, including a blood perfusion parameter to account for the body's ability to react to heat, as proposed by Pennes [8], is provided in equation (3).

$$\left(\rho C_p\right)_{skin} \frac{\partial T}{\partial t} = k_{skin} \frac{\partial^2 T}{\partial x^2} - G\left(\rho C_p\right)_{blood} \left(T - T_c\right) \tag{3}$$

The following boundary conditions are employed:

At the skin surface, x=0, t>0:

$$-k_{skin} \frac{\partial T}{\partial x} = q^{"}\left(t\right) \tag{4}$$

At the base of the subcutaneous layer, x=L, t>0:

$$T = T_c = 37°C$$

In equations (3) and (4), ρ, C_p and k are the relevant thermal properties of the skin, or blood in the case of the blood perfusion parameter, G, and T is the temperature of the skin at a skin depth of x. The incident heat flux at the skin surface is denoted q''.

A parabolic temperature distribution between 32.5°C at the surface and 37°C at the base of the subcutaneous layer, as used by Torvi and Dale [9], was used to describe the initial temperature distribution of the skin.

Equation (3) was solved with respect to skin temperature by applying a centred finite difference method to the second derivative term, and a forward finite difference method to the first derivative. A centred finite difference method was applied to the boundary condition of equation (4). The resultant expressions for the internal nodes and exposed surface are presented in equations (5) and (6) respectively.

$$T_i^{l+1} = Fo\left(T_{i+1}^l + T_{i-1}^l\right) + T_i^l\left(1 - 2Fo\right) - \frac{Fo\Delta x^2 \left(G\rho C_p\right)_{blood}}{k_{skin}} \left(T_i^l - T_c\right) \tag{5}$$

$$T_0^{l+1} = T_0^l + 2Fo\left(\frac{q^{"}\Delta x}{k_{skin}} + T_1^l - T_0^l\right) \tag{6}$$

where:

i=distance step
l=time step

and the Fourier number, $Fo = \frac{k\Delta t}{\rho C_p \Delta x^2} = \frac{\alpha \Delta t}{\Delta x^2}$ (7)

To ensure solution stability with equations (5) and (6), *Fo* must be less than 0.5. The heat flux input condition for the burn prediction model was sampled at 100 Hz. Coupled with the physical properties of the three modelled skin layers, this sets the minimum number of spatial nodes required for each of the three skin layers. Solution stability and best comparison with experimentally and theoretically determined 2nd and 3rd degree burn prediction models was achieved with the epidermis, dermis and subcutaneous layers sub-divided into 2, 25 and 270 spatial nodes respectively. A comparison between the model and experimentally determined time to 2nd degree burns [6] is made in Figure 4, and shows good agreement between the aforementioned model and the empirical and theoretical data of other researchers.

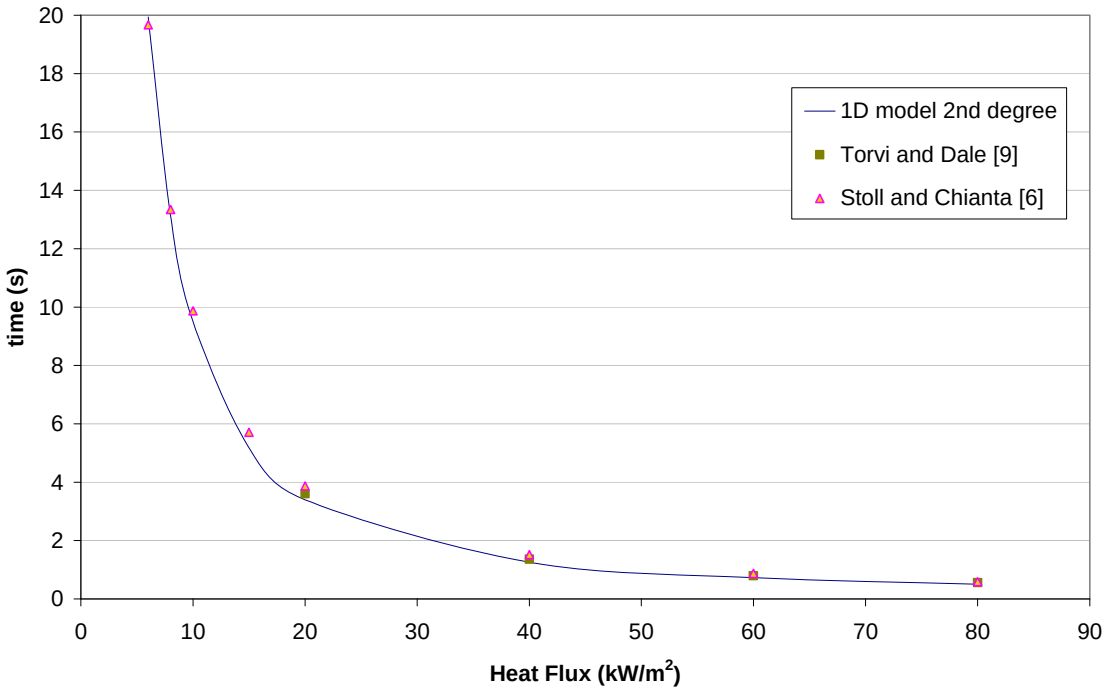

Figure 4: Comparison between the developed model and results from other workers for time to 2nd degree burns when exposed to a constant heat flux

Experimental data for 3rd degree burns is very limited, and so the model was compared with data generated from the predictive model developed by Torvi and Dale [9] which is cited in ISO 13506 [3], see Figure 5. Whilst there are slight differences in time to 3rd degree burns between the two described theoretical models, the differences are sufficiently small that they have a minimal influence on the skin burn damage data presented as part of this study.

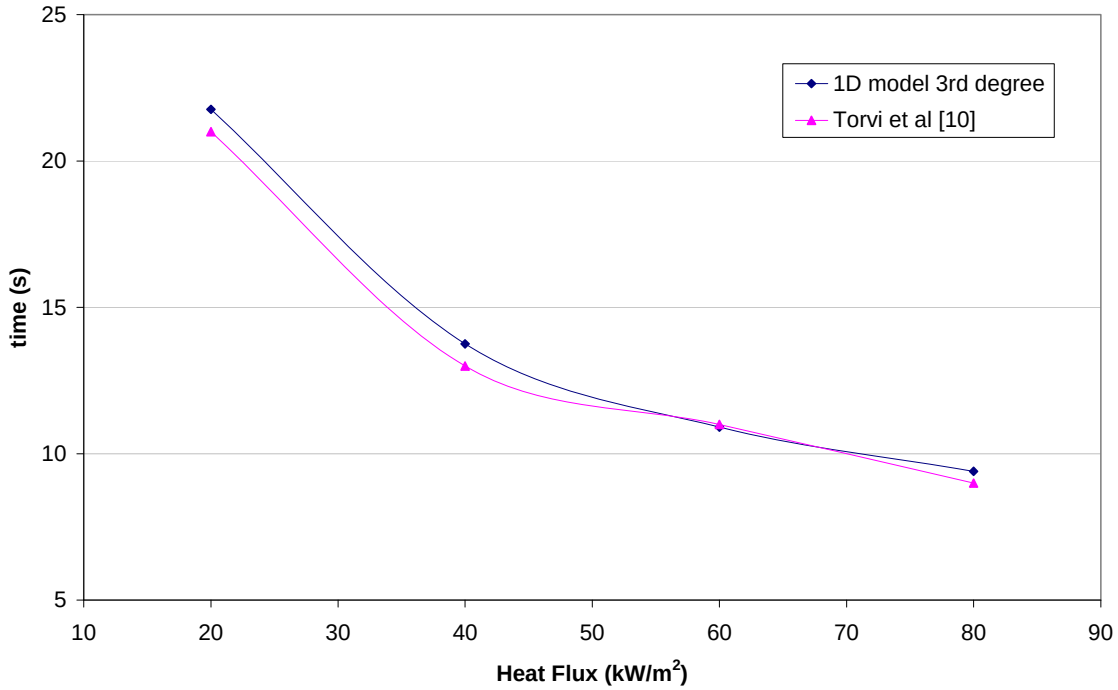

Figure 5: Comparison between the developed model and results from Torvi et al [10] for time to 3rd degree burns

The output from the developed model provides skin temperature profiles at the basal layer and dermal base, and time to 1st, 2nd and 3rd degree burns. An example of the output is provided in Figure 6 for one of the heat flux measurements made over the course of the trial. For this particular example, the incident heat flux causes 2nd and 3rd degree burns after 4.8 and 15 s respectively.

Alternative, more simplistic criteria for 2nd degree burn prediction also exist. For example, the US Army Surgeon General provides heuristics suggesting that a *T-t* integral of 1316°C.s over a 10 s exposure period, or an energy absorption level of 160 kJ/m^2 over the same time duration is required for 2nd degree burns [11]. Burn damage is not only a function of total energy absorption, but also the rate of energy absorption. As such, there is no one energy absorption level at which a given level of burn damage will occur. For this reason, the use of predictive models that use the transient heat flux profile are required if accurate burn level predictions are to be made. A comparison between burn damage predicted from the 1D-model against these heuristics is provided in Appendix C and shows that, for a cursory assessment of the likely burn severity, heuristics such as those specified by the US Army Surgeon General are a good predictor of 2nd degree burn damage.

The probability of death resulting from skin burns is a function of the surface area of the body affected by a given severity of burn coupled with the physiological characteristics of the individual. Hymes *et al* [12] developed a probability function for burn injury mortality based on data from more than 3000 burn injury patients treated in the West Midlands Regional Burns Unit in the UK between 1971 and 1980. The model accounts for the surface area of the body with second degree burns (or worse) and the age of the patient. Plotting Hymes' probability function for a 25 year-old gives the result shown in Figure 7.

Respiratory damage associated with the inhalation of hot gas is a significant hazard to the personnel inside the crew compartment in a propelling charge fire scenario. In full-scale fire tests of five residential dwellings undertaken to establish human tenability limits, Pryor [13] indicated that 149°C was a maximum ambient temperature limit for escape. Spieth *et al* [14] evaluated human hazard limits in experiments simulating aircraft crash fire situations and from their work indicated that 203°C was the maximum air temperature able to be tolerated by the human respiratory tract. As the 149°C threshold represented a more conservative limit, it was this value that was used to determine platform escape times from a respiratory damage perspective.

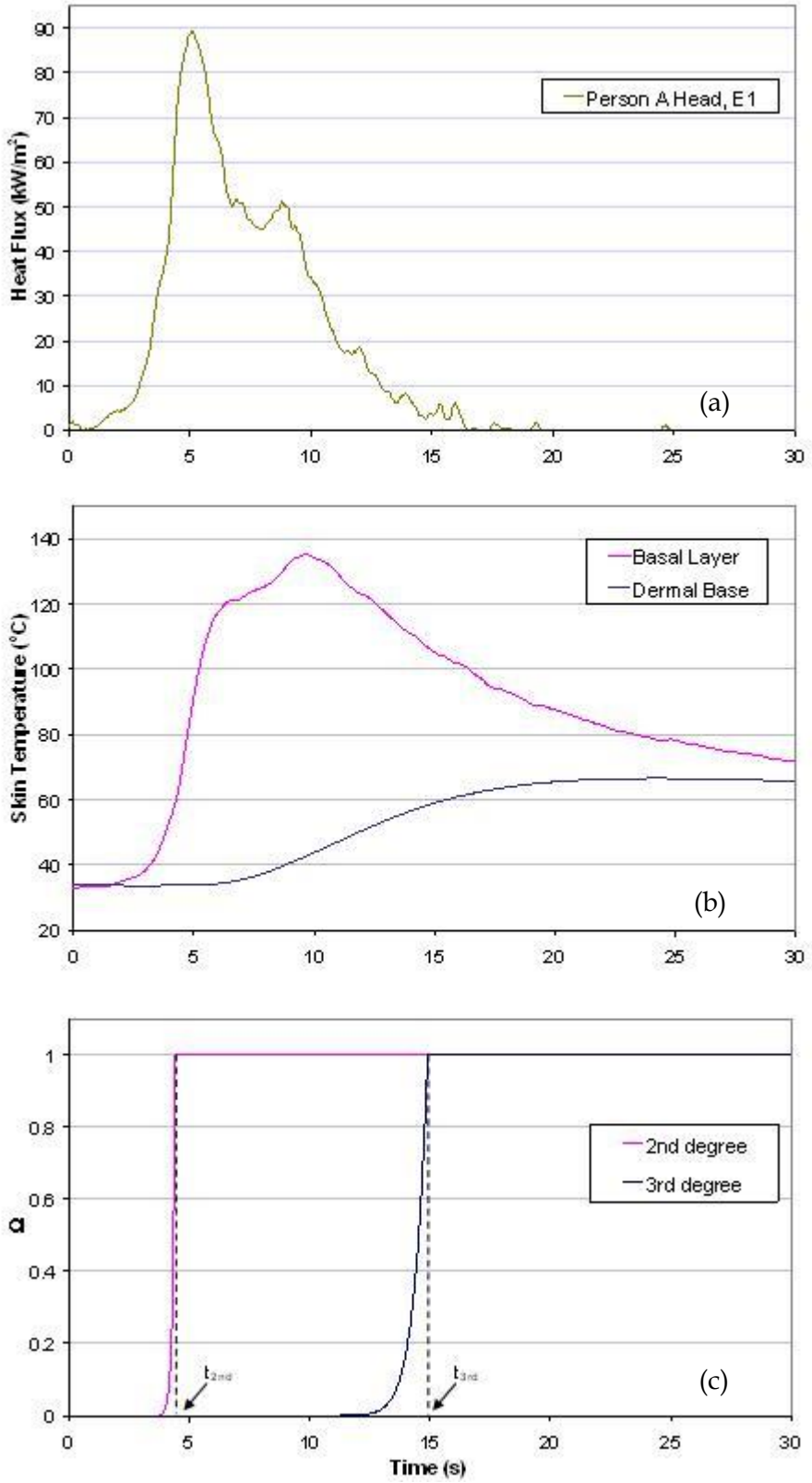

Figure 6: (a) Heat flux input from Experiment 1, and (b) skin temperature and (c) burn damage parameter showing the predicted exposure time to 2nd and 3rd degree burns

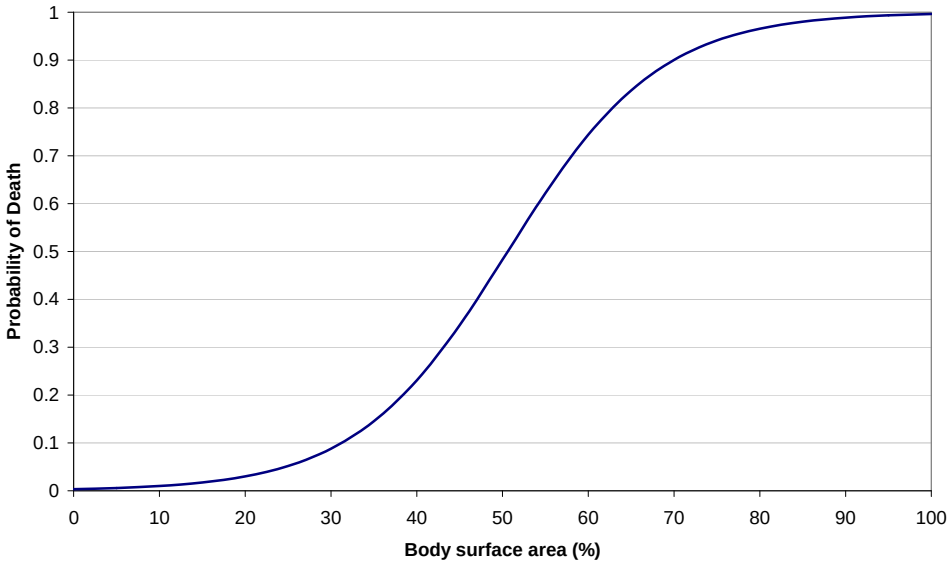

Figure 7: Probability of burn injury mortality for a 25 year-old as a function of body surface area affected by 2nd degree burns (or worse) using the model of Hymes et al.

3.2 Pressure

Non-auditory overpressure effects on simulated personnel in the crew compartment were assessed using an injury prediction methodology developed by Axelsson and Yelverton [15]. This model is considered one of the best currently available for non-auditory blast injury assessment in complex blast environments [16]. As a means of predicting the severity of injuries sustained by organs in the thorax and abdomen after exposure to complex blast environments, Axelsson and Yelverton developed an empirical model based on blast loading experiments conducted on sheep in an enclosed room [17]. To quantify the blast loading experienced by the thorax of the sheep, experiments were repeated using a cylinder, approximating the size of the sheep, with four pressure gauges mounted around its circumference. Data from 177 of the 255 sheep subjected to complex blast waves was used to develop a transfer function between the blast loading recorded on the cylinder and the severity of injury sustained by the sheep.

Yelverton [18] applied an alphanumeric pathology scoring system for the damage sustained by the intrathoracic organs of the sheep to obtain an Adjusted Severity Injury Index (*ASII*), which was then correlated with the calculated chest wall velocities (*CWV*) as per equation (8).

$$ASII = \left(0.124 + 0.117 CWV_{\max}\right)^{2.63} \qquad (8)$$

In equation (8), CWV_{max} is the average maximum inward chest wall velocity of the four pressure measurements made for each person. The *CWV* is calculated using equation (9) which, by treating the thorax as a dampened mass-spring system, provides a relationship between overpressure, *P(t)*, and chest displacement, *x*.

$$M\frac{d^2x}{dt^2}+J\frac{dx}{dt}+Kx=A\left[P(t)+P_o-P_o\left(\frac{V}{V-Ax}\right)^{\gamma}\right] \qquad (9)$$

The constants for use in equation (9), for a 70 kg mammal, are provided in Table 3. The improved Euler method was used to solve equation (9) and this is described in Appendix D.

Table 3: Constants for use in Axelsson and Yelverton's thorax model, based on 70 kg mammal [15]

Parameter	Units	Value
Effective area, A	m^2	0.082
Effective mass, M	kg	2.03
Initial lung volume, V	m^3	0.00182
Damping coefficient, J	N.s/m	696
Spring constant, K	N/m	989
Polytropic gas exponent, γ	-	1.2

The injury level category as a function of *ASII* and CWV_{max} is reproduced in Table 4.

Table 4: Intrathoracic injury levels with corresponding ASII and CWV values, reproduced from [15].

Injury Level	*ASII*	CWV_{max} (m/s)
None	0.0-0.2	0.0-3.6
Trace to slight	0.2-1.0	3.6-7.5
Slight to moderate	0.3-1.9	4.3-9.8
Moderate to extensive	1.0-7.1	7.5-16.9
>50% lethality	>3.6	>12.8

The most sensitive part of the body to overpressure is the auditory system. Whilst non-life threatening, a 50% probability of ear drum rupture occurs at 100 kPa overpressure, but can occur at overpressure levels as low as 35 kPa [19].

3.3 Ejecta

Hazards to personnel associated with ejecta strike were addressed using blunt force trauma data correlations developed by Clare *et al* [20] at Edgewood Arsenal in the 1970's. In their work, Clare *et al* subjected a range of animal species to thoracic impact from a suite of blunt projectiles and used the observed response of the animals to develop a number of kinetic energy based, lethality range correlations. This work uses a four-parameter model based on data collected from the blunt force impact of five different projectile velocity/dimension/mass combinations on the thorax of goats. The developed correlation is based on 46 data points. The correlations for the discriminate lines bounding the 50% lethality zones are provided below [20].

Upper bound:

$$\ln(WD) = \ln(Mv^2) - 7.61 \quad (10)$$

Lower bound:

$$\ln(WD) = \ln(Mv^2) - 8.1 \quad (11)$$

Where: W is the mass of the target in kilograms and was assumed to be 70 kg; D is the diameter of the projectile in centimetres; M is the mass of the projectile in grams; and, v is the projectile velocity in metres per second.

From the correlation, velocities of the likely sources of ejecta in the trial that would be required for a 50% lethality range were calculated. These velocities are summarised in Table 5.

Whilst the storage tube end-caps are a source of ejecta, they were not considered in this analysis, as the end-caps used in the trial were designed to create a realistic level of tube confinement rather than to represent the mass and geometry of the end-caps used in any specific platform.

Table 5: Ejecta velocities for 50% lethality for unburnt propellant grains and propelling charge modules.

Object	$v_{50\% \text{ lethality range}}$ (m/s)
BCM propellant	203-274
BCM	28-40
TCM propellant	136-186
TCM	15-22
ATC propellant	210-284
ATC module	28-39

The eye is the most sensitive organ to ejecta strike. Parametric studies of varying levels of eye injury resulting from impact from a range of blunt projectiles travelling at velocities between 2 and 122 m/s, found that normalised energy was the most significant predictor of ocular injury [21]. The most severe form of eye injury is globe rupture, and this was found to occur at a normalised energy level of 23771 kg/s^2. Considering the propellant grains above, this normalised energy level is achieved at velocities of 30, 35 and 40 m/s for the TCM propellant, BCM propellant and ATC propellant respectively.

3.4 Compartment Toxicity

A propelling charge fire inside the crew compartment will create appreciable quantities of propellant combustion products, the main constituents of which are CO, CO_2, H_2, H_2O and N_2. All of these will displace and dilute the ambient oxygen concentration and species such as CO and CO_2 are toxic in their own right.

In addition, automatic fire suppression systems (AFESS) are almost universally employed in armoured vehicle crew compartments. Typically the fire suppressant used is a fluorocarbon-based chemical. As discussed in [22], the high temperature decomposition products of such chemicals are highly toxic, and the suppression agent displaces oxygen and is toxic in its own right above certain concentration levels. To reduce the hazards associated with compartment toxicity, the incorporation of automatic compartment ventilation systems that operate shortly after AFESS discharge are commonly employed. Because of this, the threat posed to crew survival by compartment toxicity was assumed secondary relative to the immediate thermal, pressure and ejecta threats that could be created in a propelling charge event.

4. Experimental

4.1 Trials Structure

4.1.1 Simulated Crew Compartment

A dimensioned layout of the trials structure is provided in Figure 8. The trials structure has internal dimensions of 3.3 m long x 2.5 m wide x 2.3 m high to give a volume, in the absence of clutter, of 19.0 m^3.

Because of the large cross-sectional area of the crew compartment that is occupied by propelling charges (see Figure 2), there is no single propelling charge tube position and crew position that would best describe the spatial relationship between the personnel and the initiated propelling charge. As such, the position of the propelling charge storage tube highlighted in Figure 2 was selected for replication in the trials structure as it was considered to represent the worst-case scenario from the perspective of crew survival as it maximises the proximity of the three personnel to the propelling charge event.

The clutter that would be present inside the crew compartment (i.e control panels, seats, stowage compartments) was not represented in the trials structure as they are platform specific and their inclusion was considered beyond the scope of this study. However, as the internal dimensions of the trials structure are representative of typical armoured vehicle crew compartments, scope exists to run future trials with representative clutter added should outcomes from this work indicate a need to do so. Implications of the absence of clutter on the hazards posed to the crew in a propelling charge event are addressed in section 6.

Preliminary modelling of ignition of 3xBCMs in a propelling charge storage tube indicated peak pressures at the base of the tube of 16 MPa [1]. Due to uncertainty over certain assumptions made during the modelling process, coupled with a safety margin for design purposes, average pressure acting over the base of the tube was taken as 45 MPa. Acting over the base of the tube, this corresponds to a force of 950 kN. The design of a tube recoil system to accommodate this load and its effective integration with the trials structure in the time that was available to undertake this work program was not feasible. To overcome this, the trials structure was oriented with the propelling charge storage tube mounted on the floor. Hence, the trials structure internal geometry was designed to represent that of an actual platform

lying on its side. In effect, the floor of the trials structure is equivalent to the side wall of the crew compartment. This is illustrated in Figure 9.

The propelling charge storage tube, described in section 4.1.4, was mounted on a 350 grade steel baseplate. The baseplate was fitted with a PCB 111A23 pressure transducer and has a slotted recess to house the igniter; this is shown in Figure 10. The storage tube was attached to the baseplate via a clamping ring assembly that was bolted into the baseplate. To dampen the recoil forces transmitted to the floor of the trials structure, the baseplate was separated from the floor by a 10 mm thick pad of neoprene rubber. Both were bolted to the floor using 4 x M16 bolts.

The propelling charges were initiated via a match-head that consisted of a 1 g SR371C filled silk bag attached to a Davey Bickford 2001 series electric igniter.

The trials superstructure was fabricated with 25 mm thick steel plate, supported in a frame consisting of lengths of 150x150x6 mm and 125x75x6 mm Rectangular Hollow Section (RHS), and stiffened externally with 350 grade 150 UB I-beams. Including the internal bracing afforded by the simulated personnel inside the trial structure (see section 4.1.3) the simulated crew compartment was designed to withstand an internal static pressure of 230 kPag before yield. A rendered image and photograph of the trials superstructure is provided in Figure 11.

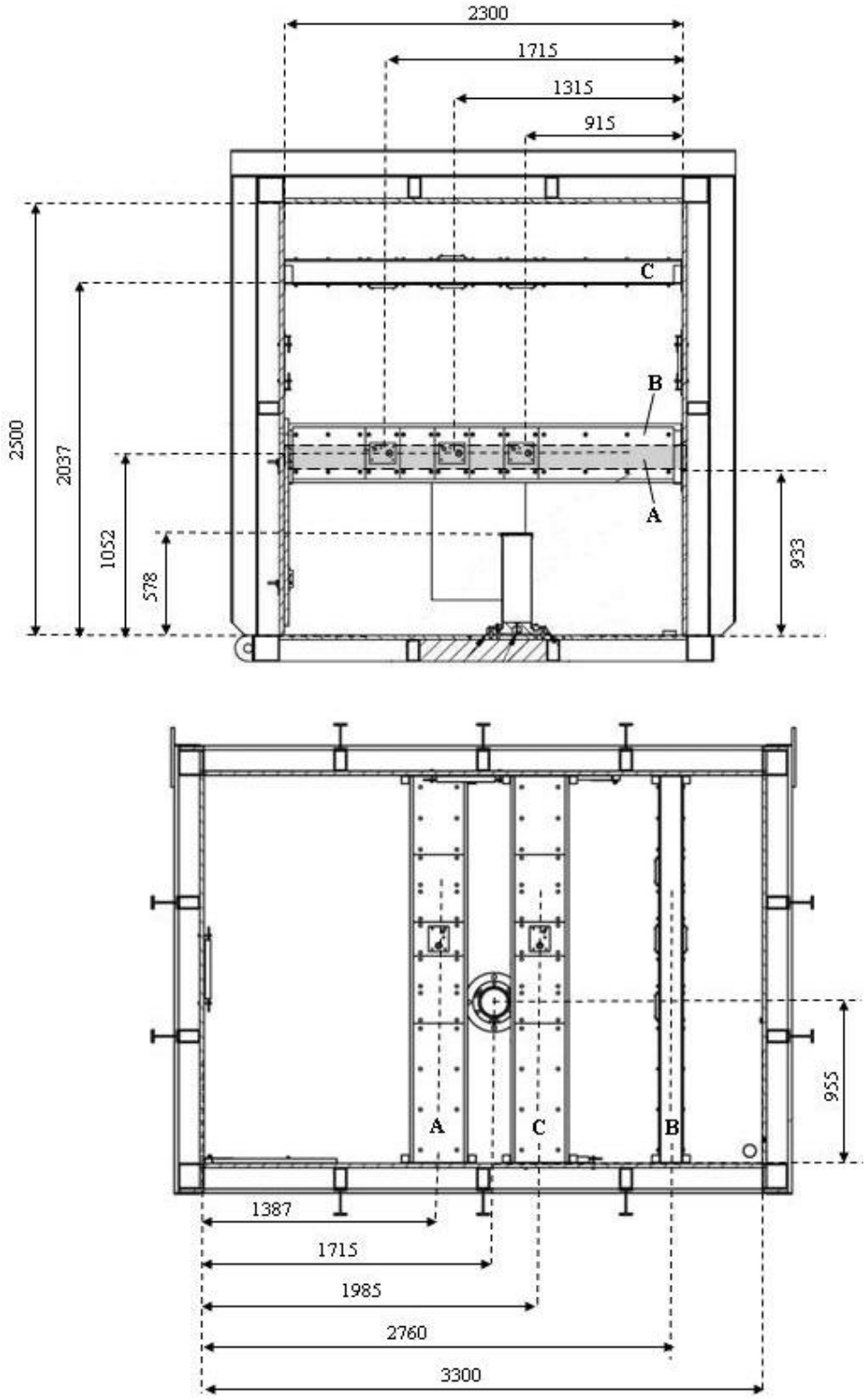

Figure 8: End-on view (top) and top-down view (bottom) schematics of the trials structure. The designation given to the three simulated personnel (A, B and C) and structure dimensions (in mm) are also shown.

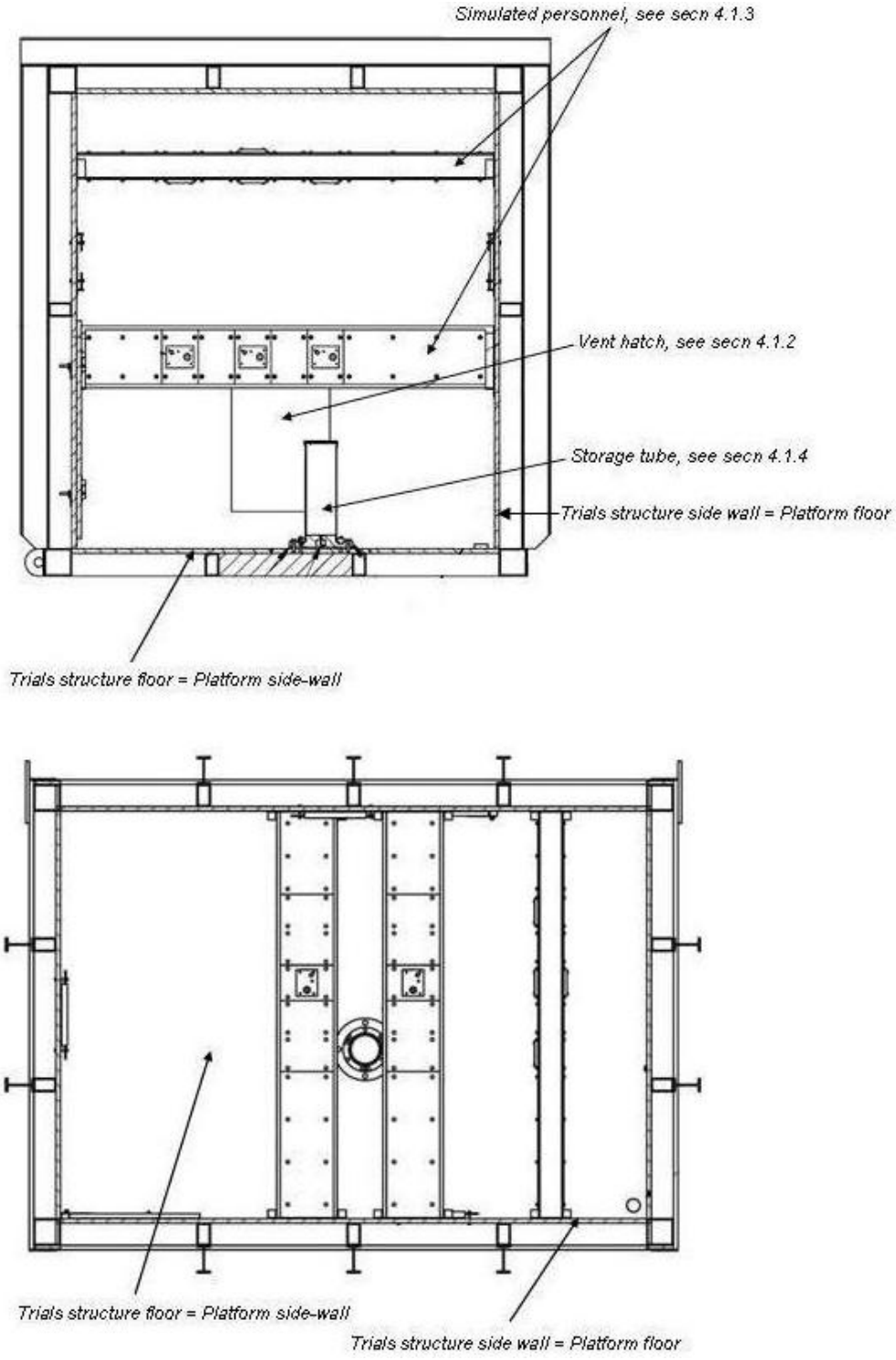

Figure 9: End-on view (above) and top-down view (below) schematics of the trials structure showing its orientation relative to the actual platform

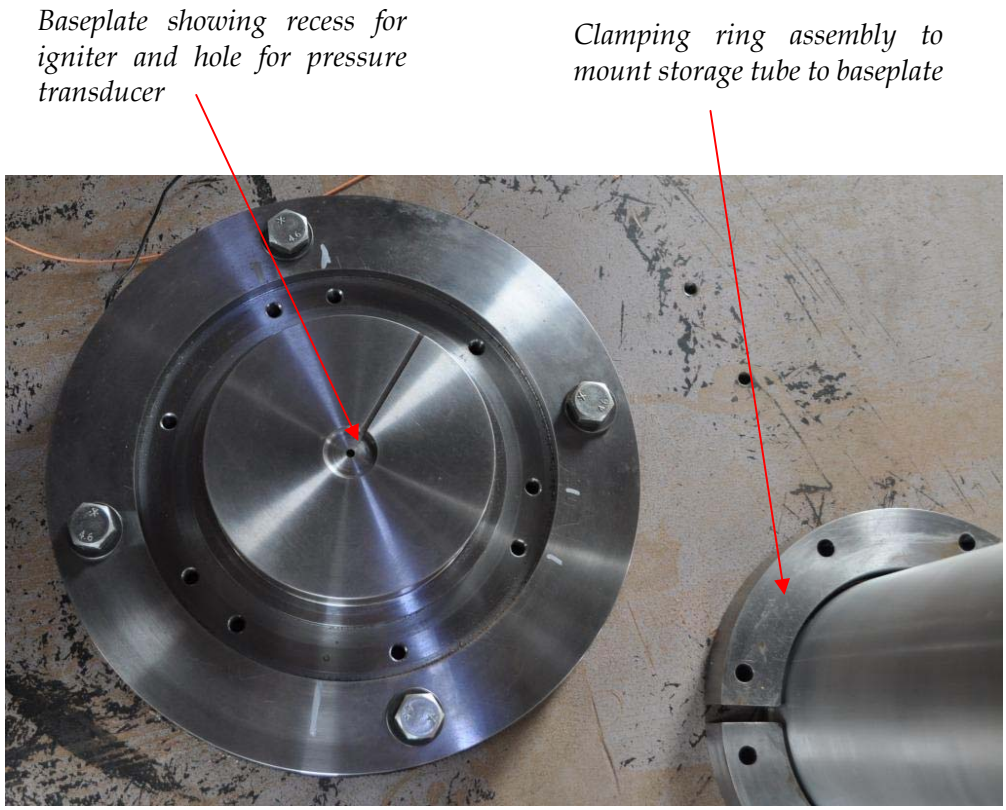

Figure 10: Baseplate and mounting assembly for propelling charge storage tube. See also Figure 20.

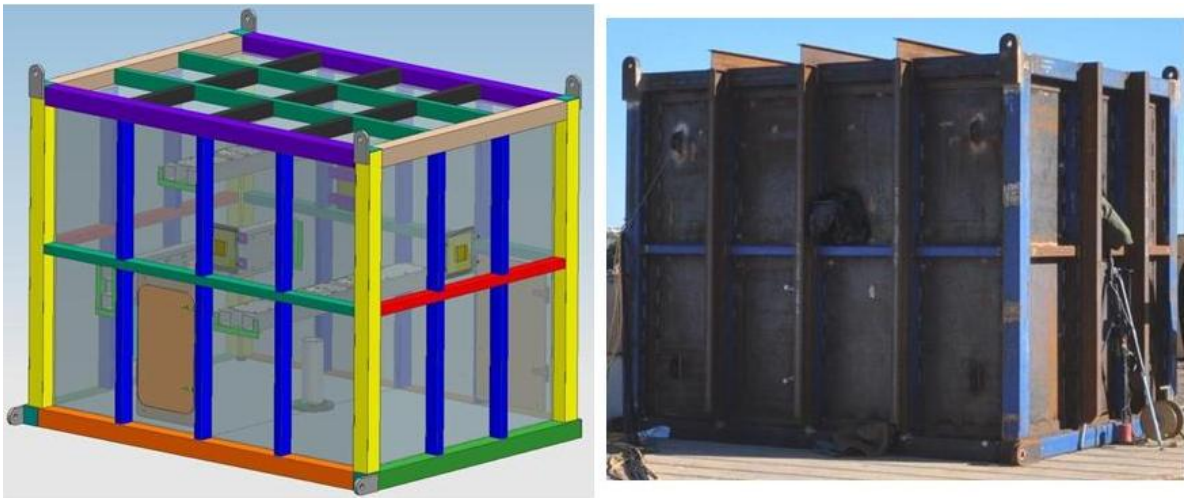

Figure 11: Trials superstructure (a) rendered image (left), (b) photo (right)

4.1.2 Crew Compartment Confinement

The level of confinement afforded by the trials structure will affect the development of pressure and temperature inside the structure, thereby potentially affecting the likelihood of survival in a propelling charge fire event. To gain an appreciation of typical crew compartment confinement levels, finite element analysis of the escape hatches and rear access door of a representative platform was undertaken to determine the pressure at which hatch failure would occur, assuming that the hatches were in the locked position. The developed models were based on information available for a representative platform and consisted of: drawings of the crew compartment; schematics of locking latch details; photographs of the rear access door of the platform; and information provided from a cursory inspection that was able to be conducted on a comparable platform [23].

Modelling was performed using MSC AFEA software [24]. The rear access door of the platform, owing to its relative surface area, was found to require the lowest load before failure. The rear door locking latch was taken as 18 mm thick and constructed of the same material as the door, which was assumed to be steel with a yield stress of 530 MPa. The door hinges were modelled using constraints in their degrees of freedom and the locking latch was modelled assuming sliding contact with the inside frame of the hull.

A static load, peaking at 100 kPag, was applied to the inside surface of the rear door in 5 kPa increments. The yield strength of the latch was exceeded at a pressure of 45 kPag, see Figure 12, and its deformation caused the door to open 118 mm at the far side from the hinge. Further latch deformation would likely result in the locking latch losing contact with the inside frame of the hull and complete opening of the door would result.

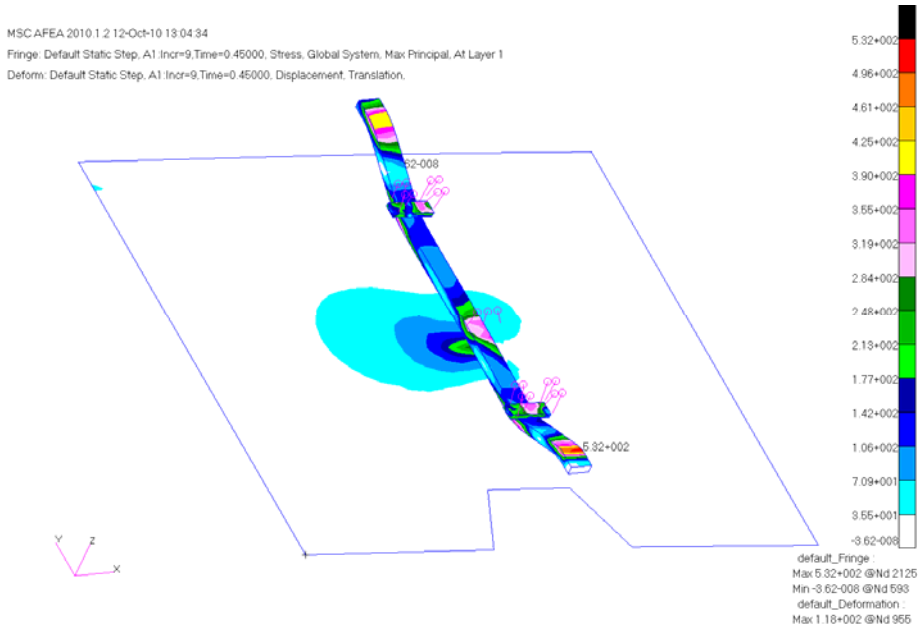

Figure 12: Peak stress on the locking latch of 532 MPa at an applied load on the rear door of 45kPag. Colour chart in MPa.

When open by 118 mm at the far side of the door from the hinge, the effective flow area between the door and the hull, using a door height and width of 1030 mm and 1190 mm respectively, is approximately 0.3 m^2. At a static load of 55 kPag, the door opens by 180 mm at the far end from the hinge, corresponding to a flow area around the door perimeter of 0.4 m^2. It should be noted that the model applies a perpendicular load to the door, so its validity decreases the further the door opens. Other complicating factors include the dynamic nature of the propelling charge event and the rate of gas generation relative to the rate of gas venting through the flow area around the door perimeter. As these factors were not known prior to conducting the trial, and also cannot be accommodated in the model, a vent area in the trials structure of 0.4 m^2 was considered to be representative.

The trials structure was originally designed with the intention of testing three levels of confinement:

- No confinement, representing a case where a platform hatch is sitting shut but not locked. In this case the vent hatch of the trials structure is pushed shut but not locked.

- Intermediate confinement, representing the modelled failure pressure of 45 kPag. In this case the vent hatch is locked shut with a notched bolt, designed to fail at a load corresponding to a uniform 45 kPag static pressure over the 0.4 m^2 area of the vent hatch.

- High confinement. This case was included to account for any assumptions made in the crew compartment failure pressure calculations that may have led to an underestimate of the actual static load required to vent the compartment. This was achieved using a notched bolt designed to fail at a load corresponding to a uniform pressure across the vent hatch of 70 kPag.

The notched bolts were necked down M16 bolts. Necked down diameters of 4.9 mm and 6.2 mm gave the required failure loads for the 45 kPag and 70 kPag confinement cases respectively. To determine the required bolt geometry, uniaxial tensile testing of the bolts was performed using a model 1185 Instron at a cross-head speed of 2 mm/min and a minimum of 5 samples were tested for each notch geometry. The low strain rate was used for uniaxial tensile testing to match the static loading conditions applied in the FEA models.

Pendine blocks were positioned around the vent hatch to arrest its motion, and lengths of docking rubber were bolted to the hatch to dampen its impact with the pendine blocks, see Figure 13.

Figure 13: Trials structure vent hatch

As described in section 5.5, the vent hatch hinges sheared off of the trials structure during the second experiment of the trial. A decision was subsequently made not to reattach the vent hatch to the structure. In lieu of the vent hatch, structure confinement was achieved with the use of 6 mm thick sheets of plywood that were either bolted to the outside of the structure to represent a lower level of confinement, or bolted to the inside of the structure to represent a high level of confinement. For each experiment the plywood was fitted with a break wire so that the time of door failure could be accurately determined.

Comparison of the break wire data with pressure measurements in the simulated crew compartment showed that the plywood mounted on the outside of the trials structure failed at a pressure of 15 kPag for the events most closely approaching a static load condition, thus representing a level of confinement between the 'no confinement' and 'intermediate confinement' cases described above. For the experiment where the plywood was mounted to the inside of the trials structure, plywood failure occurred at approximately 75 kPag. Whilst this closely matches the 'high confinement' condition described above, under a less dynamic condition this failure pressure would more likely fall between the 'intermediate' and 'high' confinement conditions.

4.1.3 Crew Personnel

The position of the three crew personnel depicted in Figure 2 was replicated in the trials structure. As the pressure and temperature environment and likely occurrence of fragmentation and ejecta in the crew compartment was not known prior to conducting the trial, it was decided not to use mannequins as the level of instrumentation deployed on each person was such that irreparable damage to any of the mannequins would be too time consuming and expensive to repair for a trial where 13 experiments were originally planned.

Two lengths of 125x125x9 mm RHS traversing the width of the crew compartment were used to represent each person, and 10 mm thick steel plate was bolted to both sides of the RHS between the head and groin positions. The instrumentation boards were bolted to the steel

plates. This configuration afforded a level of thermal and ejecta protection to the instrumentation cabling which was run down the centre of the cavity created by the steel plates and then out of the structure through rectangular slots in the side walls. The RHS was welded to the sides of the structure, thus also serving a secondary function of bracing the superstructure and increasing its strength.

Figure 14 shows rendered design drawings that illustrate the position of the three crew members and their instrumented body positions relative to the propelling charge storage tube. Dimensions of the design are provided in Figure 8. For the first experiment the steel plates at the top and bottom of the lengths of RHS were not used so as to better represent the cross-section of a human, thus reducing the influence on any dynamic pressure waves generated within the simulated crew compartment, see Figure 15. However, owing to the thermal intensity in the first experiment a decision was made to apply the bottom plates, thus covering the gap between the feet and groin, so as to reduce thermal damage to the instrumentation cabling. The top plates were not used at any stage during the trial.

The width of the simulated personnel was 340 mm and the combined thickness of the lengths of RHS with the 10 mm thick plates was 145 mm. If the trials structure is considered in its correct orientation, that is, rotated on its side so that the propellant storage tube is on the side wall of the structure, the distance from the centre of the instrumentation boards representing the four body regions to the ground is as follows:

Groin	915 mm
Chest/Back	1315 mm
Head	1715 mm

The instrumentation boards were manufactured from synthetic resin bonded paper (SRBP). The SRBP was selected as: it is suitable for high temperature applications; is easy to machine; contains no silica based materials and so, unlike many other thermally insulating materials, will not be adversely affected by the presence of hydrogen fluoride (HF)[1]; and finally, the SRBP has a thermal diffusivity and a thermal effusivity similar to that of human skin, see Table 6. The thermal properties of the SRBP were measured using a Mathis TCi thermal conductivity analyser and the results presented are the average of 10 measurements made on the sample. Sensor calibration was performed using a polycarbonate reference sample of equivalent cross section to the SRBP sample. The SRBP was painted with matt black Septone heat proof paint to give a surface emissivity close to the 0.94 of human skin [25]. A photograph of an instrumentation board with its mounted instrumentation is shown in Figure 16.

[1] Created by the high temperature decomposition of fluorocarbon-based fire suppressants.

Table 6: Comparison of skin and SRBP thermal properties. SRBP properties are the average of ten measurements, the standard deviation of which is shown in brackets. Skin properties are reproduced from Table 1.

Parameter	Epidermis	Dermis	Subcutaneous layer	SRBP
ρ (kg/m^3)	1200	1200	1000	1350
k (W/m.K)	0.255	0.523	0.167	0.35 (0.001)
C_p (J/kg.K)	3600	3230	2760	2113 (7.4)
α x10^7 (m^2/s)	0.59	1.35	0.61	1.23 (0.0007)
e (J/m^2.K.s$^{0.5}$)	1050	1423	679	999 (3.2)

The instrumentation boards representing the groin region were covered with a single layer of Nomex (93% meta-aramid, 5% para-aramid plain weave fire resistant cloth); the chest and back regions were covered by a single layer of cotton beneath a layer of Nomex to simulate the protection afforded to personnel wearing a t-shirt beneath their Nomex coveralls. The Nomex was selected on advice from DMO's Combat Clothing Department [26]. Six metres of 150 cm wide Nomex fabric was sourced through DMO's Combat Clothing Section for the purposes of the trial. The cotton fabric was 100% cotton and was purchased locally as 150 cm wide sheet.

The Nomex and cotton material were washed separately in a domestic washing machine and then air dried inside. Once dry, the fabric was cut into swatches, nominally 24x24 cm in size, as shown in Figure 17. Whilst naturally draped fabric will have air gaps between the fabric and skin, thus affording additional thermal insulation, the existence and size of these air gaps is a function of the size of the garment relative to the wearer and is also dependant on the posture (eg. sitting or standing) of the individual. To remove these factors as variables, the fabric was pulled sufficiently tight to ensure that there were no air gaps between the back face of the clothing and the instrumentation boards. The fabric was then held in place with the four bolts used to attach the instrumentation boards to the steel backing plates. The edges of the clothing were then tucked in behind the instrumentation board to prevent direct gas flow between the clothing and the instrumentation board, see Figure 18.

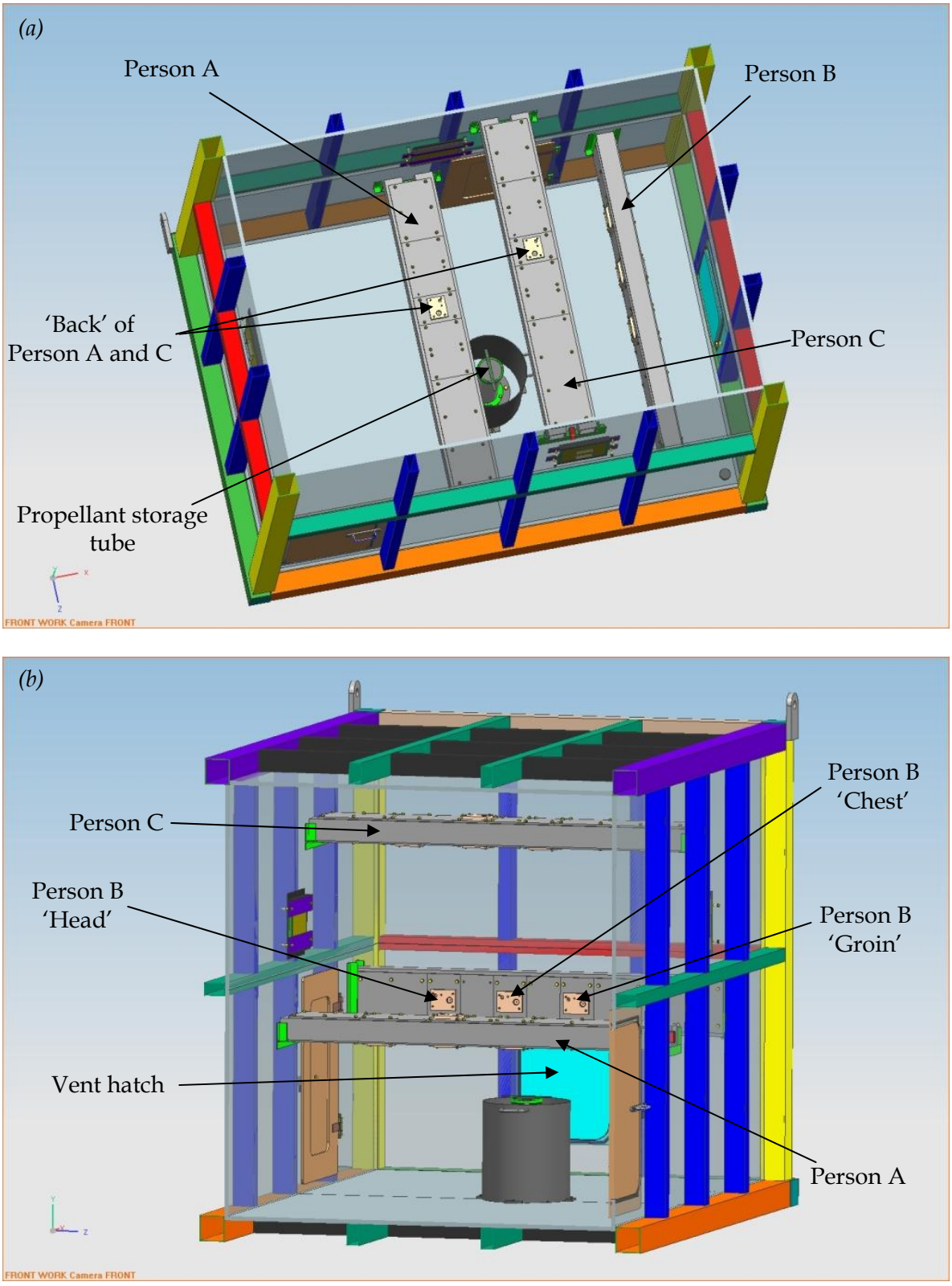

Figure 14: Schematic of the position of the three simulated personnel within the crew compartment and their respective groin, chest, back and head positions from (a) above, (b) end view

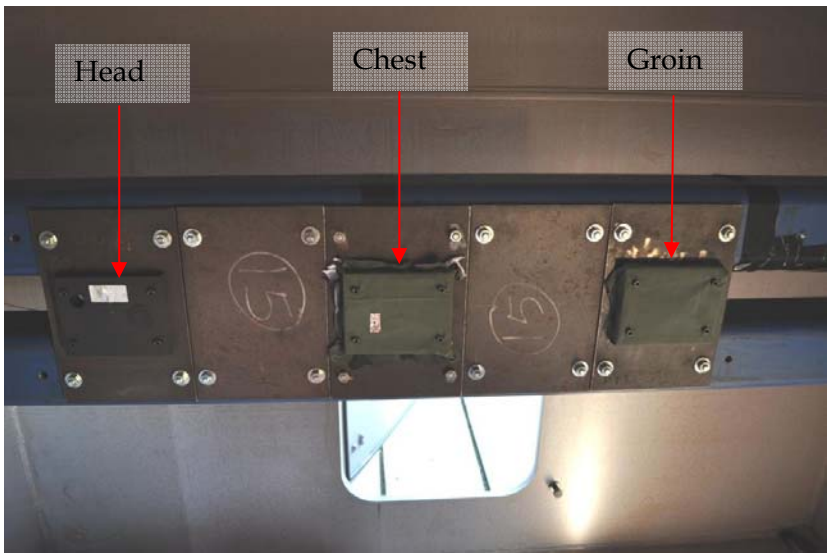

Figure 15: Photograph of the front of Person B with instrumentation boards and associated clothing

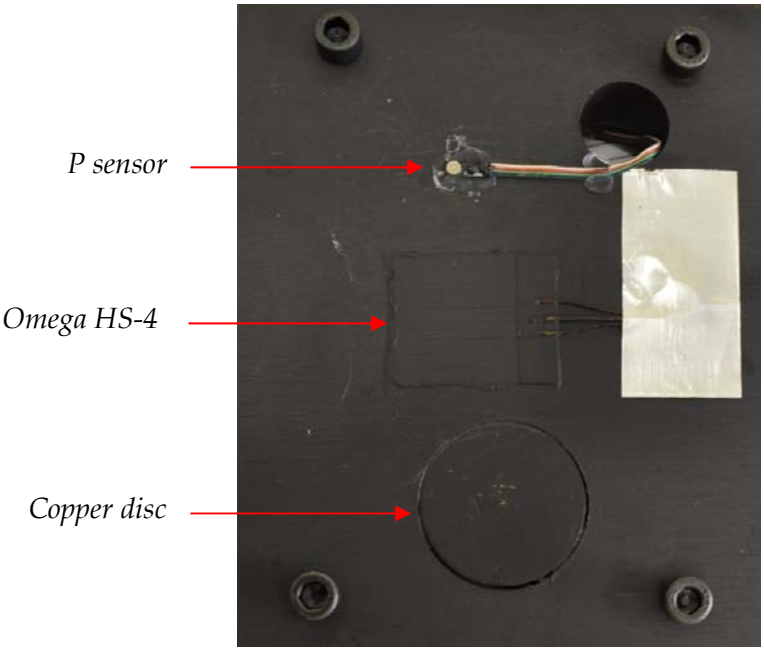

Figure 16: Instrumentation board with mounted sensors

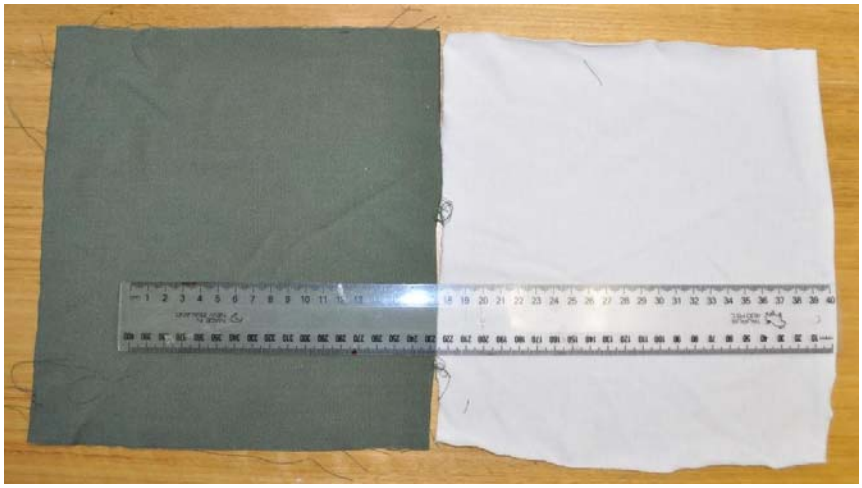

Figure 17: Nomex (left) and cotton (right) fabric swatches prepared for the trial

Figure 18: Instrumentation board covered with a cotton and Nomex fabric swatch

4.1.4 Propelling Charge Storage Tubes

The propelling charge storage tubes were based on storage tubes used in platforms similar to that being represented in the trial and were designed to have an equivalent burst pressure. Using Barlow's formula, a strain-rate independent storage tube burst pressure of 8-19 MPa was calculated. To account for the higher strain rate event more applicable to a fast burning reaction in the propelling charge storage tube, an arbitrarily selected multiplication factor of 1.6 was applied to give an estimate for the high-strain rate burst pressure of 13-30 MPa. Preliminary interior ballistics modelling of ignition of a propellant mass representative of that contained within 3 BCMs in a storage tube of equivalent internal volume indicated a peak tube pressure of 16 MPa [1]. Hence, the possibility of storage tube rupture would exist.

To allow for base ignition, a 3 mm diameter hole was drilled into the side of the storage tubes at the same height as the cut-out channel in the baseplate so that the igniter lead could be fed

out of the tube. After the igniter had been put in position, plasticine was used to seal any remaining flow area around the igniter wire and the drilled hole.

The storage tube being simulated is sealed with a threaded polycarbonate end-cap. Finite element analysis of the polycarbonate end-cap and tube assembly was performed using MSC AFEA software [24]. The analysis indicated that failure would occur at the thread of the end-cap at an internal static pressure of between 750 and 800 kPag, see Figure 19. This, coupled with radial expansion of the aluminium tube under the pressure generated in the early stages of propellant combustion, would likely see the end-cap ejected from the storage tube whole.

A polycarbonate disc, coupled with an end-cap retention ring, was used in the trial, with FEA analysis used to determine the required polycarbonate thickness (6 mm) to replicate the confinement and failure mode of the storage tube end-cap being simulated.

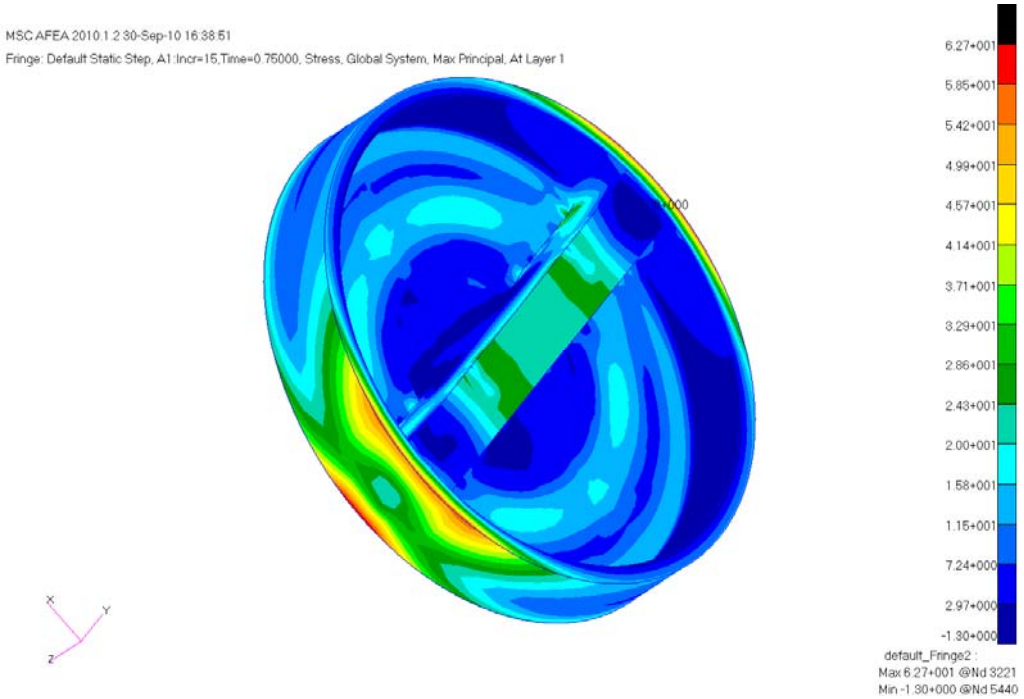

Figure 19: 1st principal stress of polycarbonate end-cap of 62.7 MPa at 750 kPag internal pressure. Colour chart in MPa.

For the first two experiments, an unthreaded storage tube was G-clamped to a fragmentation capture ring that surrounded the propelling charge, see Figure 20. This was done to qualitatively assess the possibility of sympathetic initiation of a neighbouring storage tube via the fragmentation of the primary propelling charge storage tube.

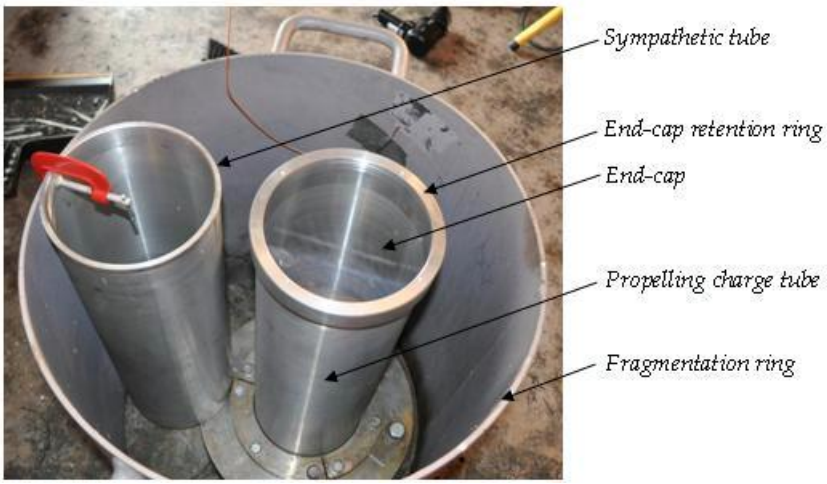

Figure 20: Propelling charge tube configuration for sympathetic fragmentation effect assessment

4.2 Instrumentation

4.2.1 Thermal

Heat flux was measured using two types of sensors: Omega HS-4 thermopile sensors, purchased from Omega Industries, that give a direct measure of heat flux as well as temperature; and a combination of 1.6 mm and 1.2 mm thick, 35 mm diameter copper discs (>99% purity) whose temperature was measured with a K-type thermocouple attached to the centre of the back face of the disc.

Two techniques were used for attaching the K-type thermocouples to the copper discs. Initially, silver epoxy was used as it permitted the use of a smaller bead of material, thus adding less thermal mass to the disc. However, after initial testing it became apparent that the silver epoxy was not able to withstand the sustained, high temperature environment in the trials structure. Subsequently, 60/40 lead/tin solder with a melting point of approximately 190°C was used to attach the thermocouples to the copper discs.

The use of solder required a slightly larger application of bonding material to the copper disc, thus adding to the sensors thermal mass. The effect of this additional mass was ignored during heat flux calculations due to the high magnitude of the heat fluxes observed throughout the course of the trial, coupled with care being taken during the application of the solder to minimise its mass.

The copper discs were bonded to the instrumentation boards using hot melt glue applied around the circumference of the discs. The hot melt glue had a softening temperature of approximately 80°C under the application of a steady heat from a hot air gun.

The Omega HS-4 gauges were bonded to the instrumentation boards using Omegabond 200 two part epoxy that was applied to the back of the gauges at a temperature of 50°C. Small

weights were placed on top of the gauges during the epoxy cure process, undertaken in an oven at 90°C for a minimum of 48 hours, to ensure they remained flat on the instrumentation boards.

The exposed face of the Omega HS-4 gauges and copper discs were painted with matt black Septone Heat Proof paint to give a sensor emissivity close to that of human skin, ε=0.94 [25]. Before painting, the Omega HS-4 gauges were wiped down with methylated spirits. To remove the oxide layer from the copper discs prior to painting and attaching the K-type thermocouples, each disc was immersed in a bath of 15% HCl solution, cleaned using a cotton bud, then immersed in a bath of deionised water followed by immersion in a bath of acetone to remove any residual moisture.

Both the Omega HS-4 gauges and the K-type thermocouples attached to the copper discs were sampled at 100 Hz and the data was then filtered at 10 Hz. To permit the acquisition of accurate temperature data at these sampling rates, high speed temperature compensated thermocouple modules were developed at DSTO. The modules consisted of a Linear Technologies LTKA0x thermocouple amplifier with associated cold junction compensator (LT1025). Galvanic isolation was provided by a high speed AD125 low distortion isolation amplifier. The resultant isolated thermocouple input modules had a frequency response from DC to greater than 50 kHz with excellent common mode rejection and DC isolation to 2000 V. Module performance was verified with a Eurotron MicroCal1 that is calibrated annually by the NATA accredited laboratory, ABSTEC. Calibration over the course of the trial was performed with a Yokogawa CA12E Handy Cal.

A lumped heat capacity analysis was used to convert the transient temperature profile of the copper discs to a heat flux that could then be used for burn damage calculations. So as not to invalidate the lumped heat capacity analysis, it was necessary to insulate the back face of the copper discs. This was achieved by machining an air gap into the instrumentation board with a lip to accommodate the copper disc, as shown in the schematic of Figure 21. The 6 mm diameter hole was used for running the thermocouple wire out the back of the instrumentation board.

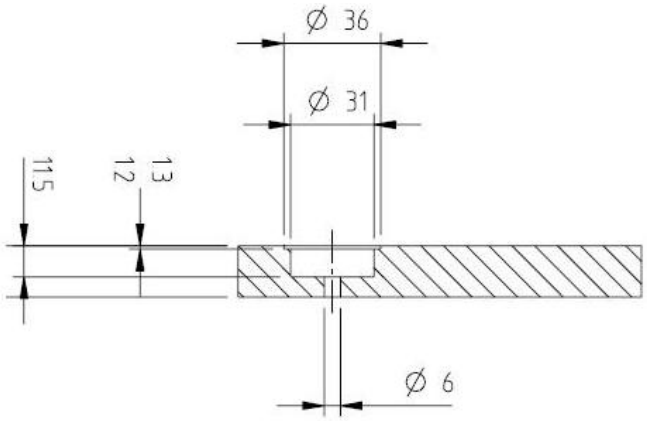

Figure 21: Profile of the copper disc mounting and air gap configuration on the instrumentation boards (dimensions in mm)

After sufficient comparative data had been acquired to demonstrate equivalence between the heat flux output of the two sensor types, the copper discs were positioned at the locations where higher heat fluxes were observed (typically the head and groin positions) and the Omega HS-4 sensors were positioned in areas of less severe heat flux (typically the chest and back). For each experiment, a minimum of one type of heat flux sensor was positioned on each body segment of the simulated personnel.

In addition to the heat flux and temperature measurements on the simulated personnel inside the crew compartment, three K-type thermocouples (*T1*, *T2* and *T3*) were positioned inside the crew compartment to monitor the ambient temperature profile. The location of these thermocouples is shown in Figure 22. The K-type thermocouples were sampled at 100 Hz.

The ambient temperature and relative humidity (*RH*) was measured inside the simulated crew compartment immediately prior to each experiment using a PCWI whirling hygrometer. All ambient crew compartment temperature data presented in the report is normalised to a starting environmental condition of 15°C and 65% *RH* at an atmospheric pressure of 101 kPa.

When normalising the *RH*, to allow for non-homogenous temperature distributions throughout the crew compartment during the course of the propelling charge event, it was assumed that the water content making up the difference between the actual *RH* and the 65% *RH* was vaporised evenly over an arbitrarily selected time-span. This time-span was taken from when the first ambient room thermocouple (either of *T1* or *T2*, uncorrected temperature) reached 95°C to when the last room thermocouple (either of *T1* or *T2*, uncorrected temperature) reached 105°C. Over the course of the trial, variation of actual *RH* relative to the 65% *RH* condition was sufficiently small and the magnitude of the energy released during the propelling charge event sufficiently large, that applying the *RH* normalisation procedure had no influence on the corrected ambient room temperature-time profiles. The ambient environmental conditions inside the trials structure immediately prior to each experiment are provided in Table 24, Appendix A.

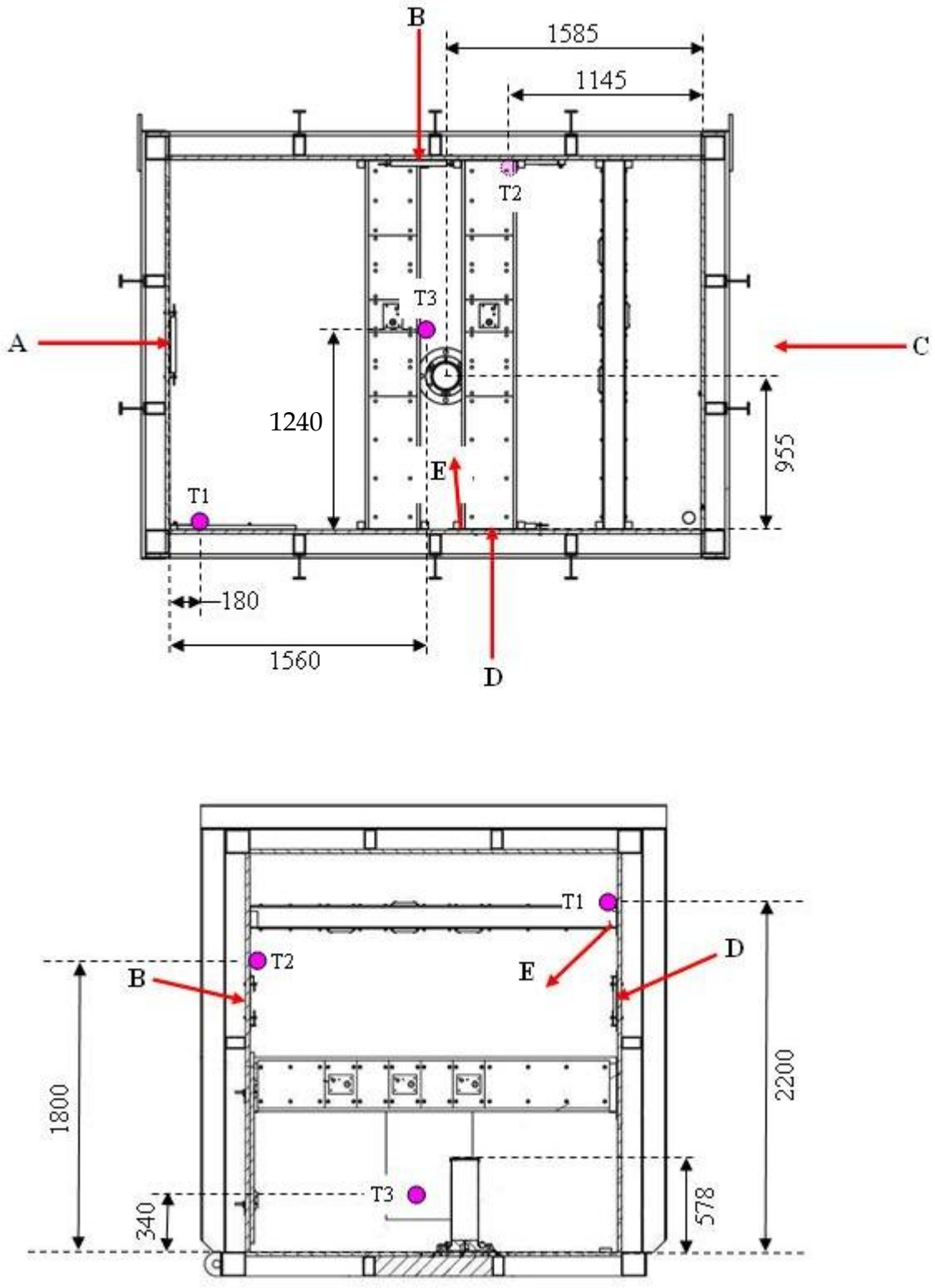

Figure 22: Approximate camera viewing angles (see Table 7) and position of the three ambient room thermocouples (dimensions in mm)

4.2.2 Ejecta

A range of cameras were used from different viewing angles over the course of the trial as familiarity was gained with the nature of the propelling charge events and of key areas of interest inside the crew compartment. Camera viewing angles and operational details are summarised in Figure 22 and Table 7 respectively.

Table 7: Camera details

Experiment	View	Camera	Frame Rate/s	Record time (s)
1-2	A	Customised Cats Eye QC3495^	25	-
		Canon Exilim	420	600
	B	Canon Exilim	420	600
	C	KTK 801C or Cats Eye QC3495	25	-
	D	Photron SA1.1	3000	3.6
	E	KTK 801C or Cats Eye QC3495	25	-
3-15	A	Customised Cats Eye QC3495^	25	-
		Canon Exilim	420	600
	B	Mikrotron Cube 6	400	9
	C	Canon Exilim	420	600
		KTK 801C or Cats Eye QC3495	25	-
	D	Photron SA1.1	3000, 1000*	3.6, 10.9*
	E	KTK 801C or Cats Eye QC3495	25	-

^Cats Eye QC3495 sensor in a c-mount lens body with a Fujinon YV2.7x2.9LR4D2 lens set at 4 mm
*1000 fps was used for Experiment 7 to Experiment 15

To provide illumination for the initial stages of the propelling charge event two PF330 flash bulbs of 1 s burn duration were used in conjunction with consumable plastic flash bulb reflectors mounted at the ceiling above the viewing angle A window. The flash bulbs were triggered off the same firing pulse used to ignite the match-head. To reduce light absorption, the inside walls of the trials structure were painted with 'hidden grey' tinted Dulux exterior acrylic paint.

Ejecta velocities were determined from images captured from viewing angles B and D using a Photron SA1.1 camera and a Mikrotron Cube 6 camera. Both cameras were fitted with Nikon 17-35 mm lenses. The Photron SA1.1 had the zoom set at 17 mm and the Mikrotron Cube 6 zoom was set at 19 mm. Photron Fastcam Viewer 3 software was used for viewing the camera frames.

To calculate grain and module velocities, unburnt grains or sections of propelling charge module of a known dimension were used for scale. The known dimension (either length or diameter) was used to calculate a scale factor at the first and last frame over which the velocity was calculated. An average scale factor was then calculated and used to determine the distance travelled by the piece of ejecta over the number of frames (and therefore time) in question. The use of a scale factor for each ejecta velocity calculation accounted for the fact

that the grains and modules do not necessarily move perpendicular to the camera over the measurement period of interest.

For selected experiments a 1 mm thick aluminium witness plate, with a cross-sectional dimension of approximately 1.2 m by 0.9 m, was mounted on the ceiling of the crew compartment with an 8 mm standoff distance. The witness plate was positioned directly above the propelling charge storage tube with the bottom and top of the witness plate extending past the groin and head of Person C respectively. The distance from the top of the propelling charge storage tube to the front of the witness plate was 1915 mm.

4.2.3 Pressure

Four Kulite LE-080-250PSIA thin line, high temperature pressure transducers were attached to the chest, back and sides of Person A, B and C to measure the dynamic pressure experienced by the thorax of the simulated crew. The pressure transducers were mounted on the instrumentation boards (for chest and back) and sides of the RHS beams (for the two sides of the thorax) using hot melt glue. The thin profile of these sensors meant that protrusion above the level of the clothed instrumentation board was minimal.

To remove any possible influence of the clothing on the measured pressures, as recommended in [16], a small hole was cut in the fabric swatches so that the transducer would not be covered by clothing. To prevent any flame or gas migration into the hole cut in the fabric swatches, the fabric around the transducer was taped to the instrumentation board with a small piece of aluminium tape. This is shown in Figure 23.

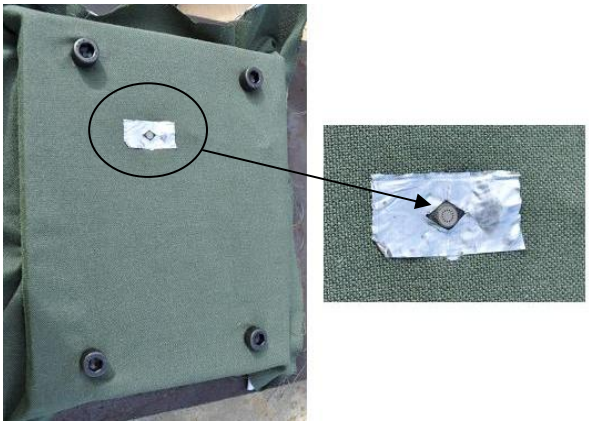

Figure 23: LE-080-250PSIA pressure transducer mounting arrangement for the chest and back

It is noted that the use of flat plates and the RHS beams to represent the four sides of the thorax does not match the contours of the human thorax. However, studies conducted of human surrogates exposed to blast overpressure environments found that the differences in measured pressure-time histories using pressure transducers mounted directly on an anatomically accurate blast test dummy, a cylinder of a representative diameter, and flat plates attached to the dummy had no influence on the outcomes of the injury assessment [27].

The pressure transducers were sampled at 100 kHz.

4.2.4 Compartment Toxicity

Because platforms of the type being simulated in the trial commonly use automatic ventilation systems, the threat posed to crew survival by compartment toxicity was assumed secondary relative to the immediate thermal, pressure and ejecta threats that could be created in a propelling charge event. As such, in-situ real-time monitoring of the atmosphere within the trials structure was not performed during the trial.

To ensure the safety of the trials participants, after the conduct of an experiment a number of measures were put in place prior to personnel being permitted entry into the trials structure.

For baseline experiments, the camera footage fed to the control bunker was used for a preliminary post-test clearance check. Following this, the clearance officer opened the trials structure access doors and turned on a blower positioned at one of the doors to ventilate the structure. An Eagle meter gas detector was also available to measure the atmospheric oxygen content inside the trial structure.

4.3 Open Air Ignition Tests

To better understand the event sequences and observations from the high speed camera footage during propelling charge ignition and the initial stages of bulk propellant combustion, a series of open-air ignition tests were conducted. From these tests, typical timings from match-head initiation through to ignition of the modular charge centre-core ignition train and then initial combustion of the combustible case and bulk propellant for the BCM and TCM configurations were able to be established.

High speed video at frame rates between 1500 and 3000 frames/s with a Photron SA1.1 camera was used to determine the sequence of events for three configurations:

- Configuration 1: Match-head containing 1 g SR371C with a series 2001 Davey Bickford fusehead
- Configuration 2: Match-head positioned below 10 g of centre-core igniter material held in a plastic tube of the same internal diameter of the modular charge centre-core
- Configuration 3: Match-head positioned below 10 g of centre-core igniter material held inside the centre-core of a BCM in the same configuration as that used in the trial

The experimental setup for configuration 2 is shown in Figure 24 and the combustible case used in configuration 3, with perimeter wall removed, is shown in Figure 25. The holes in the centre-core tube are clearly visible. String is fed through these holes to hold the centre-core igniter material centrally within the centre-core and also allows direct flow of hot combustion products from the centre-core igniter into the bulk propellant bed.

To simulate the confinement of the centre-core tube for configuration 2, two holes were drilled through either end of the plastic tube (to allow the centre-core igniter material to be suspended in the middle of the tube using string) with a similar diameter to the holes in the centre-core tube in the BCM and TCM. A piece of cardboard of a comparable cross-sectional

area to the base of the combustible module was mounted onto the base of the plastic-tube to prevent the output from the match-head flashing up the outer wall of the tube. A single piece of adhesive tape was also added to the bottom and top of the plastic tube to simulate the tape used in the BCM and TCM. For configuration 3, the outer wall of the combustible case was cut away to provide visibility of the centre-core, thus allowing the time delay between match-head ignition to flash from the holes in the centre-core tube to be determined.

Figure 24: Experimental setup for configuration 2. The match-head can be seen below the cardboard sheet in-line with the plastic tube.

Figure 25: Image of the cut away combustible case used in configuration 3. The holes in the centre-core tube are also visible. The ruler markings are in cm.

4.4 Trials Schedule

The original trials schedule was based on the evaluation of the effect of the following variables on crew survival: module type and number; AFESS effectiveness; and, room confinement.

However, due to the loss of the vent hatch on the second experiment of the trial, the ability to undertake a thorough evaluation of room confinement was not possible. Despite this, a less rigorous assessment was still conducted by altering the way in which the plywood, used to replace the vent hatch, was mounted to the simulated crew compartment.

The reduced testing scope with respect to room confinement, did however, allow an assessment of the effect of module storage configuration and ignition location to be undertaken.

The baseline tests listed in Table 8 are the subject of this paper. For Experiment 1 and Experiment 2 the vent hatch was pushed shut, but was not held in position with any of the manufactured notched bolts and hence is representative of a hatch being closed, but not locked in position. In the absence of the vent hatch, experiments where the plywood was mounted on the outside of the structure are representative of an intermediate confinement case. For Experiment 14, mounting of the plywood on the inside of the structure was representative of the highest crew compartment confinement case conducted in the trial.

Table 8: Baseline experimental schedule

Experiment	Module	Confinement
1	2xBCM	Hatch
2	3xBCM	Hatch
3	1xTCM	Plywood
4	2xBCM	Plywood
9	2xATC	Plywood
10	3xBCM	Plywood
14	3xBCM	Inner Plywood

The experiments listed in Table 9 were undertaken to investigate the effect of storage tube modification, charge ignition location and an AFESS on the hazards posed to crew. Results from these experiments are the subject of [22].

Table 9: Hazard mitigation and ignition location experimental schedule

Experiment	Module	Other
Storage tube modification and ignition location		
11	3xBCM	No end-cap
12	3xBCM	No end-cap, top ignition
15	3xBCM	Loose modules
AFESS experiments		
5	2xBCM	4xGas
6	1xTCM	4xGas
7	3xBCM	4xGas
8	2xBCM	4xGas
13	1xTCM	4xGas + 2xWater

5. Results and Discussion

5.1 Event Sequence

The sequence of events from match-head ignition through to the completion of propelling charge combustion were investigated for each experiment using the array of cameras deployed in and around the trials structure. Points of interest noted from this footage are summarised in section 5.1.2 to 5.1.5. Times quoted refer to the time elapsed after the firing pulse was sent to the match-head. For view angles A and E, the cameras used were only time stamped to the nearest second. Hence, whilst the described images for these view angles are placed in chronological order, an exact time for the presented frames can not be provided. The reader is referred to Table 7 in section 4.2.2 for a description of the camera detail and orientation for the view angles quoted in this section.

5.1.1 Open Air Igniter Tests

Figure 26 provides camera images at various stages of match-head ignition. Evidence of match-head ignition first occurred at 0.67 ms after the firing pulse, followed by ignition of the pyrotechnic fill in the silk bag at 2.67 ms, peak visual output at 116 ms and then the cessation of match-head output at 493 ms.

Selected images of the open air testing of the centre-core igniter material in the plastic tube, configuration 2, are provided in Figure 27. Silk bag ignition occurred at 1.67 ms, the flash from which penetrated into the plastic tube at 6.3 ms. The image at 31 ms marks the time at which the flame from the match-head completely fills the simulated centre-core tube. Sparks from the match-head output were first observed exiting the top two holes of the tube at 44 ms followed by the commencement of flame and gas flow through these holes at 130 ms. The 170 ms image shows flash exiting the two top holes as well as the commencement of gas and flame exiting through the top of the tube as the adhesive tape fails. Bulk ignition of the centre-core igniter material occurred at 180 ms and continued until 1060 ms.

Figure 28 shows selected images of igniter test configuration 3 where the same ignition configuration used in the BCMs was used. Flash from the match-head was first observed coming from the bottom two holes in the centre-core tube at 13.5 ms. The first sparks were seen exiting the top holes of the centre-core tube at 48 ms, prior to flame exiting the top holes at 113 ms. At 172 ms, flame penetrates through the adhesive tape on the top of the centre-core, at this time the flame emanating radially from the top two centre-core holes ceases. Rapid flame evolution through the top of the centre-core immediately after failure of the adhesive tape indicates the onset of bulk centre-core igniter material burning. The camera footage suggested the onset of combustible case burning at 540 ms.

The observed sequences and timings of the initial ignition events are consistent between each of the three open air tests.

Bulk propellant bed ignition will commence shortly after the time that flash exits the radial holes in the centre-core tube. The flame spread through the propellant bed will then be a function of propellant bed permeability, the progressive burning geometry of the propellant grains, and the position and number of holes in the module centre-core. The larger TCM grains will have greater bed permeability than the smaller BCM grains. Due to the longer length of the TCM relative to a BCM, there will be a greater time delay before flame and hot ignition gases exit the top centre-core holes of each module. The smaller number of centre-core holes per unit length for a single TCM (4 centre-core holes/module) will also inhibit the initial rate of gas generation from the bulk propellant when compared with an equivalent length of BCMs (3xBCM) where there would be 12 centre-core holes along the combined length of the centre-core. This is discussed further in section 5.4.1.

Figure 26: Open air ignition trial, configuration 1, match-head output at various stages after the firing pulse.

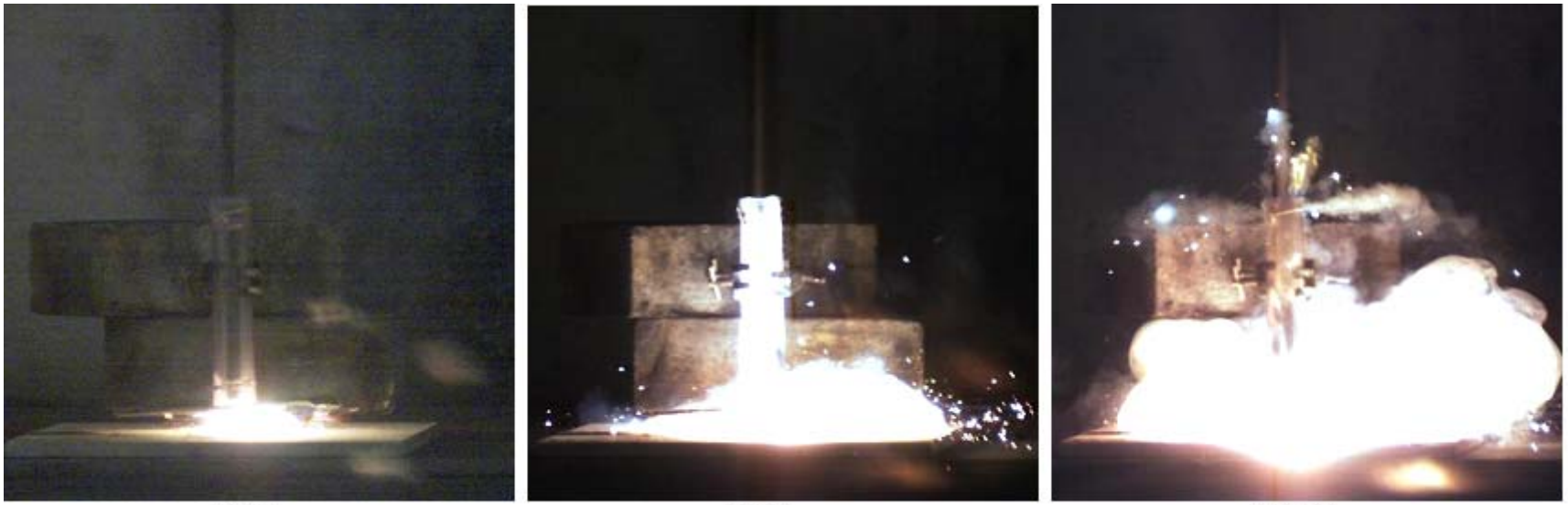

Figure 27: Open air ignition trial, configuration 2, centre-core igniter material ignition in a transparent tube, showing igniter output at various stages after the firing pulse was sent to the match-head.

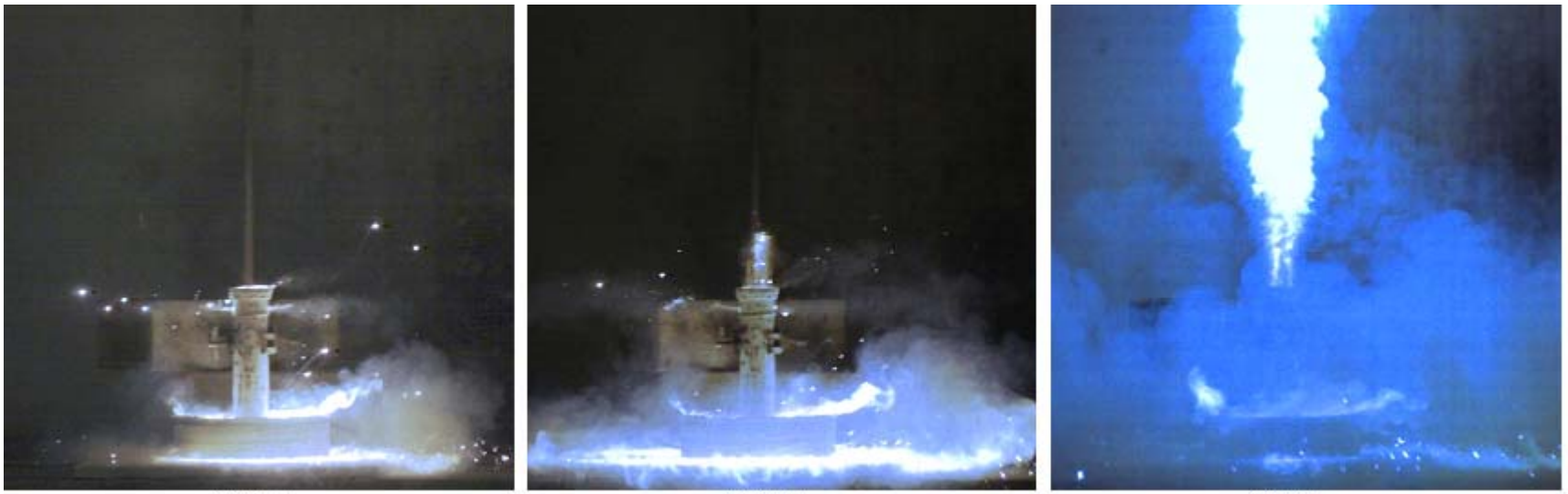

Figure 28: Open air ignition trial, configuration 3, centre-core igniter material ignition in a cut-away combustible case, showing igniter output at various stages after the firing pulse was sent to the match-head.

5.1.2 2xBCM Configuration

Table 10 summarises the key observations made during the 2xBCM configuration of Experiment 4. Screenshots presented in Figure 30 correspond to the numbered images in Table 10.

Camera footage showed that the upper of the two modules in the storage tube exits the storage tube predominately intact, and then strikes the ceiling scattering unburnt propellant grains inside the crew compartment. The loose, unburnt propellant grains are then ignited initially by burning firebrands, followed by the autoignition of remaining propellant when the ambient temperature exceeds the propellant ignition temperature. For the 2xBCM configuration, the bulk of the contents of the lower module remain in the storage tube and, ignited by the initial ignition event, burn to produce a high intensity flame that emanates from the storage tube.

A photo of the burnt out shell of the upper module combustible case next to the propelling charge storage tube (Experiment 4) and of three propellant grains collected from outside the trials structure next to the vent hatch (Experiment 1), showing different degrees of outer grain graphite coating consumption are provided in Figure 29.

Figure 29: Burnt out combustible module case shell from Experiment 4 (top) and three propellant grains showing varying levels of outer graphite layer coating consumption collected from outside the trials structure in Experiment 1 (bottom).

Table 10: Sequence of events for 2xBCM configuration, Experiment 4, as noted from camera footage. See Figure 30 for selected images.

View Angle (Image)	Time (ms)	Observation
D	136	Evidence of match-head output
D (1)	247	End-cap failure
D	252	Propelling charge module decoppering sleeve exiting tube
D	263-271	Mass of ejecta, including unburnt propellant grains, exiting tube.
D	281	Upper module exits tube
D (2)	294	Upon exit of upper module (*arrow*), flame is evident inside the storage tube.
D	309	Flame exits from tube
D	320	Tube engulfed in flame
B (3)	336-367	Strands of centre-core igniter material and propellant grains visible exiting tube
D	409-442	Fireball 'lifts-off' tube, grains continue to be ejected from below fireball.
D (4)	539	Burning grains and shell of combustible case (*arrow*) falling from roof, no fire visible in the top of the storage tube.
D (5)	1379	Widespread, low intensity fire on floor
D	1626	Vent hatch opens
D (6)	1671-2050	Fire redevelops in tube from combustion of propellant from the lower module and creates 'Roman candle' effect.
D (7)	2338	Fire transitions to mass internal fire
B (8)	3172	Clothing of Person C groin on fire (*arrow*), burning propellant grains being ejected from the storage tube at low velocity.
A	~17 000	Propellant combustion ceases

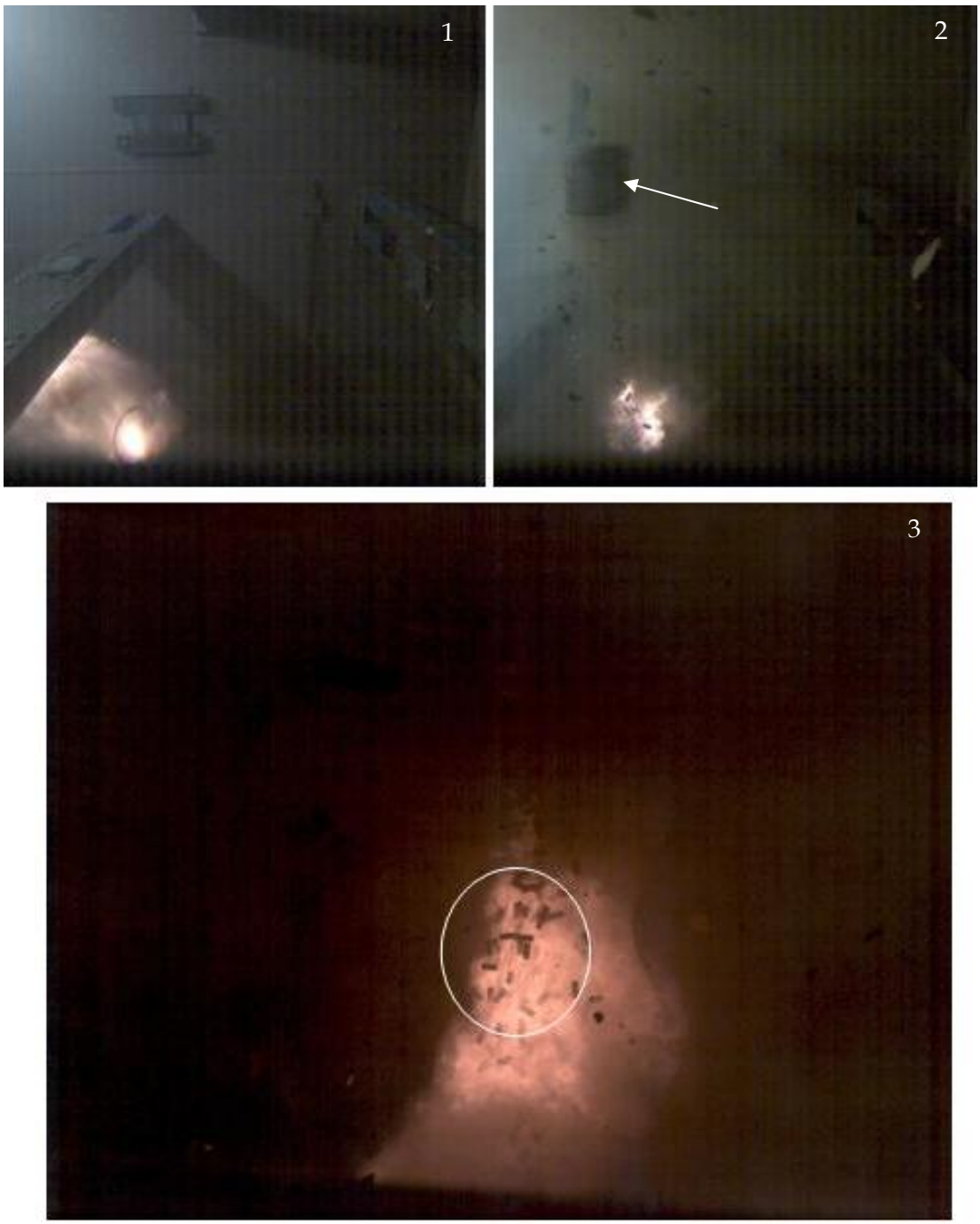

Figure 30: Selected images for Experiment 4, refer to Table 10.

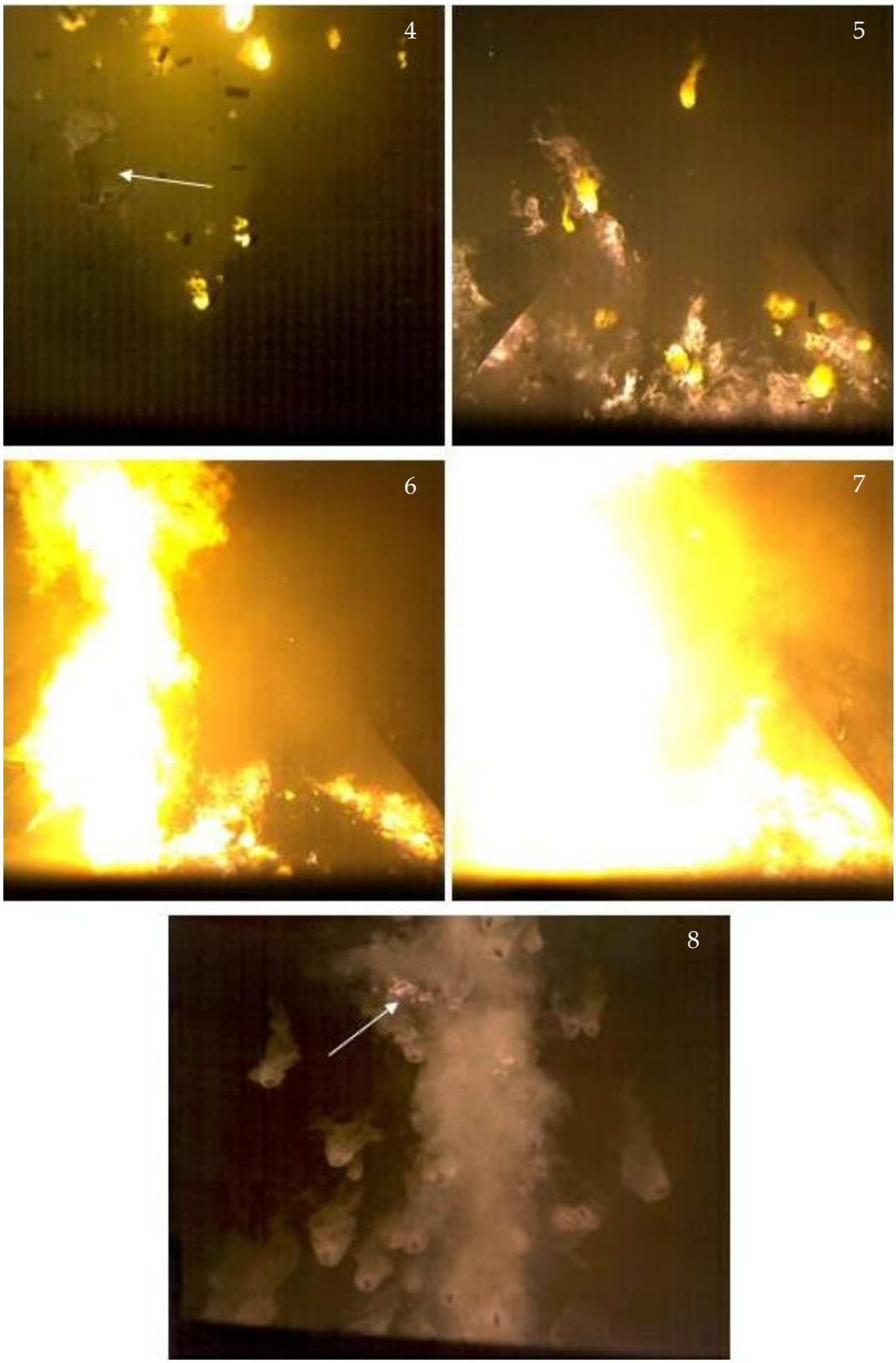

Figure 30: Selected images for Experiment 4, refer to Table 10. (cont.)

5.1.3 1xTCM Configuration

Table 11 summarises the key events of the 1xTCM configuration baseline test as observed from the camera footage of Experiment 3. Screenshots presented in Figure 31 correspond to the numbered images in Table 11.

The sequence of events for the 1xTCM configuration is similar to that described in section 5.1.2 for the 2xBCM configuration, with the exception that the 1xTCM configuration has only one module. The TCM exits the storage tube, predominately intact, save for the base of the combustible case which separates from the cylindrical shell, allowing a portion of unburnt propellant grains to remain in the storage tube. As for the other module configurations, this propellant burns to create a flamethrower effect from the storage tube.

Selected photographs taken post-experiment are provided in Figure 32.

Table 11: Sequence of events for 1xTCM configuration, Experiment 3, as noted from camera footage. See Figure 31 for selected images.

View Angle (Image)	Time (ms)	Observation
D	91	Evidence of match-head output
D	212	Partial ignition of module centre-core
D (1)	277	Storage tube end-cap failure
D	283-290	Initial fireball and debris from tube
D	301	Module exits tube
D (2)	318	Module (*arrow*), without its base, travels away from storage tube with unburnt centre-core igniter material and grains falling out from base of module.
D	643	Burning debris and propellant falling from ceiling
B (3)	946	Burning module case falling from ceiling
D	1326-1552	Burning module bounces off storage tube and lands on ground between the storage tube and Person B. Bulk combustion of the propelling charge module develops.
D	2101	Fire develops in storage tube
D	3100	Vent hatch opens
D	3403	Mass fire in trials structure
B (4), A (5)	3900	'Roman candle' effect from propellant fire in storage tube. Clothing on chest and groin of Person C ignites (*arrow*). Fire continues to burn between the storage tube and Person B.
A	~19 000	Combustion ceases

Figure 31: Selected images for Experiment 3, refer to Table 11.

Figure 32: (top) Burn marks on floor of trial structure highlight the widespread burning of propellant throughout the structure; (middle) Person C groin showing the loss of the copper disc sensor and the destruction of the Nomex clothing initially protecting the groin; (bottom) Fractured propellant grain collected from outside the trials structure near the vent hatch.

5.1.4 3xBCM Baseline Configuration

Complete event sequences for the 3xBCM configurations were not able to be determined due to image obscuration associated with ejecta dispersion shortly after end-cap failure and image saturation due to the intensity of the fire inside the trials structure. A summary of the events noted for Experiment 10 are provided in Table 12, with selected images provided in Figure 33.

Table 12: Sequence of events for 3xBCM baseline configuration, Experiment 10, as noted from camera footage. See Figure 33 for selected images.

View Angle (Image)	Time (ms)	Observation
D	236	Evidence of match-head output
D (1)	323	Storage tube end-cap failure
D (2)	328-333	Debris and ejecta exits tube
-	333-402	Complete image obscuration
D	402	Orange glow on image indicates fire development
D	435	Propellant grains and centre-core igniter material can be seen moving away from the storage tube towards the ceiling
D	464-1474	Image appears black
D	1474	Orange glow on image indicates fire development
D	2000	Mass fire developed
B (3)	3294	Person A (*right*) and C (*left) (arrows*) subjected to high intensity flame impingement.
B	3300	Clothing of chest and groin of Person C on fire
D	3976	Fire begins to reduce in size
D	4534	Bulk fire in room ceases, localised portions of propellant continue to burn on ground.
D	4600-5880	Low intensity combustion continues in tube
A	~9 000	Combustion ceases

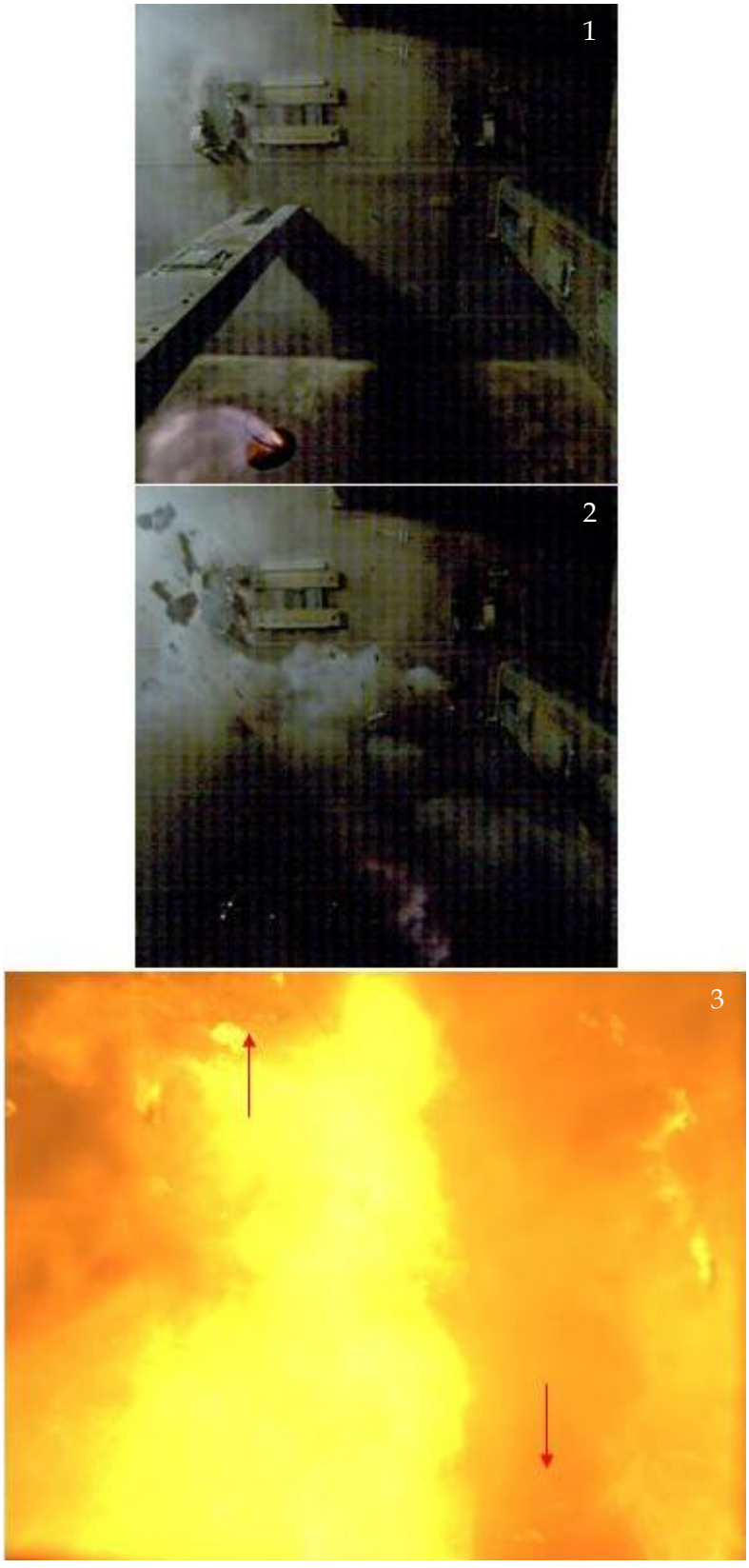

Figure 33: Selected images for Experiment 10, refer to Table 12.

5.1.5 2xATC Configuration

Table 13 summarises the key observations made during the 2xATC configuration of Experiment 9. Camera footage indicated a different ignition sequence to that observed with the other charges and this was also evident from the storage tube pressure measurements for Experiment 9, see section 5.4.1. This is attributed to the different centre-core ignition train of the ATC when compared with the BCM and TCM configurations.

Post storage tube end-cap failure, the event sequence for the 2xATC configuration was the same as that described for the 2xBCM configuration in section 5.1.2.

Carbonaceous remains of the shell of the lower module combustible case were found in the base of the storage tube post-test, confirming that the lower module did not exit the storage tube. Photographs of carbonaceous propellant residue and remains of the burnt out upper module situated on top of Person C are shown in Figure 34.

Figure 34: Carbonaceous propellant residue (top) and portion of burnt out combustible case (bottom) from Experiment 9

Table 13: Sequence of events for 2xATC configuration, Experiment 9, as noted from camera footage. See Figure 35 for selected images.

View Angle (Image)	Time (ms)	Observation
D	146	Light emitted from match-head ignition first evident in tube
D	177	First match-head spark evident at tope of tube
D	365	Tube goes dark as light from ignition disappears, match-head sparks still evident.
D (1)	457	Tube illuminated by 'instantaneous' flash associated with ignition of modular charge igniter train.
D (2)	485	End-cap fails
B (3)	500	Upper module and propellant grains exiting tube
D	618	Grains from lower module exiting tube
D	773	Commencement of localised burning of material falling to ground, including the upper module which has come to rest on top of Person C.
B	786	Burning propellant grains falling from ceiling
D	977	Flash of flame from the storage tube, large quantity of grains still in the air.
D	1143	Part of combustible case, on fire, falling to the ground.
D	1725	Burning combustible case hits the ground, small localised fires on the ground evident.
D	3372	Fire, originating near the base of the storage tube, starts to spread across the floor.
D	3502	Combustion intensity increases around the tube.
D (4)	3560	Fire develops in the storage tube
D	4372	Vent hatch opens
D, A (5)	4608	High intensity flame impingement originating from the storage tube on Person C.
D (6)	5587	Flames 'washing over' Person B, mass fire developed.
D	10116	Mass fire loses intensity
A	~19000	Propellant combustion ceases

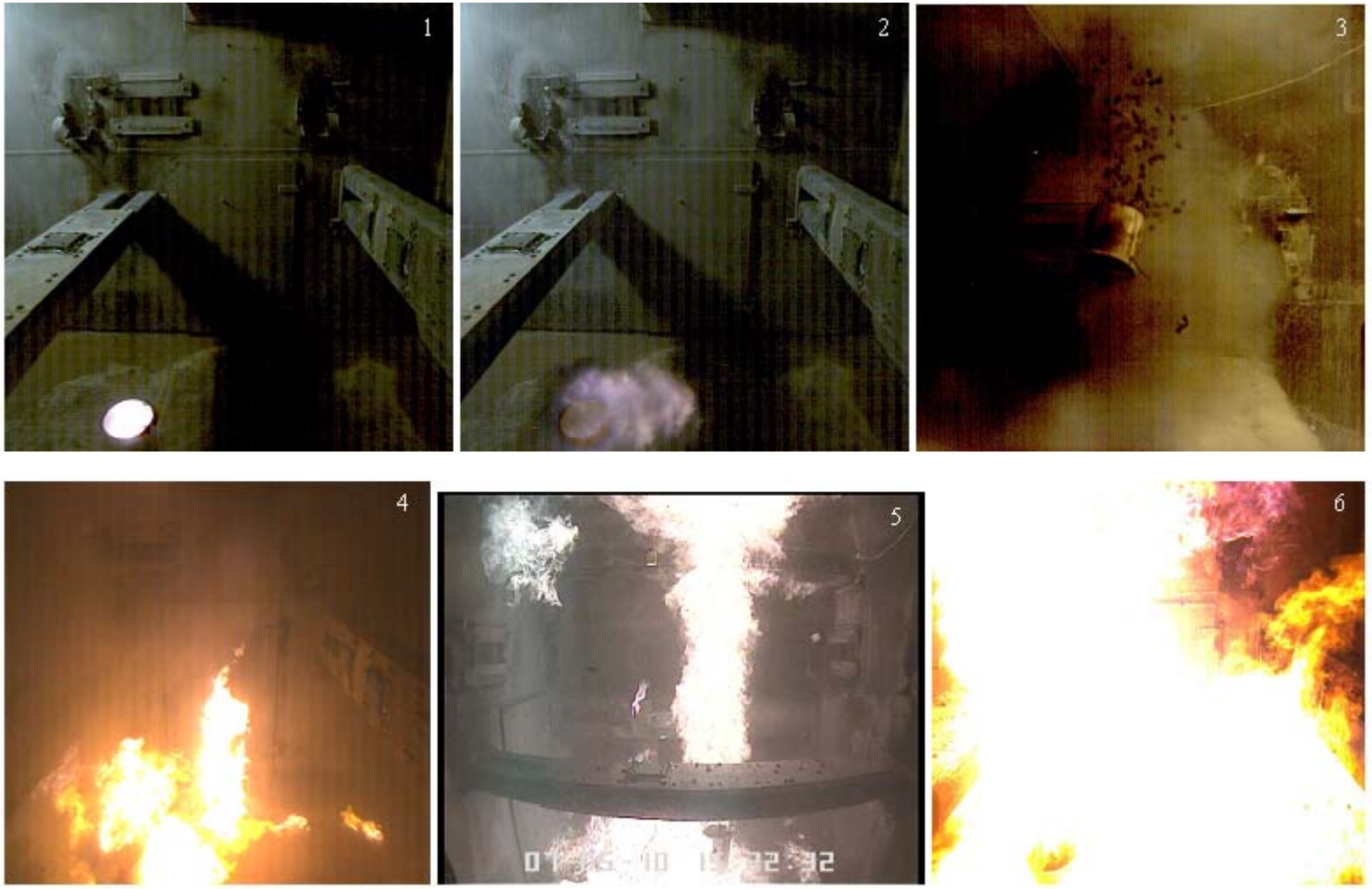

Figure 35: Selected images from Experiment 9, refer to Table 13.

5.2 Thermal

Burn charts are provided in this section as a means of summarising the burns sustained by the three personnel inside the simulated crew compartment and are provided for two scenarios:

- Crew personnel exposed to the thermal environment inside the crew compartment for 10 s. This was arbitrarily considered to be a realistic time for all of the personnel inside the crew compartment to escape if they have not sustained any injuries that affect their mobility or their ability to operate latches to escape hatches or the rear access door.

- Crew personnel exposed to the thermal environment for 30 s. This was assumed to be representative of a scenario where the crew were unable to immediately escape the vehicle due to injuries that may have been sustained, or if the propelling charge event affected the structure of the crew compartment in such a way that egress from the crew compartment was not initially possible.

Burn injuries for these two scenarios were modelled by applying the measured transient heat fluxes for either 10 s or 30 s. After this time the heat flux was set to zero and so any additional burning sustained after this time is as a result of burns occurring as the skin cools. Integrating the heat flux versus time curves gives the energy absorbed and these values are presented for a 10 s exposure time as an additional comparative tool.

Ambient crew compartment temperature conditions are plotted versus time to permit an assessment of escape time from a respiratory viewpoint, and to consider the likelihood of sympathetic cook-off of munitions stored in the crew compartment. The plotted temperature is the average of thermocouples *T1* and *T2*, see Figure 22 in section 4.2.1, as these thermocouples are positioned at approximately head height and therefore are of more relevance from a respiratory hazard perspective. *T3* was not included in the average temperature, as its proximity to the ground made it more susceptible to the location of burning propellant and other modular charge components.

It should be noted that the measured crew compartment temperatures and heat fluxes are not only influenced by the experimental variable of interest, but also by the gas dynamics inside the room, both prior to and upon room venting, and where propelling charge modules and propellant gets distributed over the course of the event. Post experiment inspection and video footage was used where possible to track the distribution of propellant and propelling charge modules for each experiment, and where relevant, these are commented upon in light of the observed results.

5.2.1 Module Configuration

This section summarises the thermal results for the four module configurations tested under baseline conditions (i.e. storage tube with end-cap, base ignition and outer plywood for room confinement).

From results presented in Table 14 and Figure 36, the following general conclusions can be made:

- The groin and chest of Person C suffered a given level of burn damage more rapidly than was the case for these body regions on Person A and B. This is due to the position of Person C relative to the propelling charge storage tube. Because Person C is positioned almost directly in line with the storage tube, the front of Person C, and in particular the groin, is subjected to direct flame impingement from the jet of flame that emanates from the storage tube. This can be seen in a number of screenshots provided in section 5.1, see for example Image 5 in Figure 35.

- Conversely, the backs of Person B and C consistently showed a lower level of burn damage as the respective positions are protected from direct flame impingement and are also better protected from radiative heat transfer.

- The use of both cotton and Nomex (as used on the chest and back) offered significantly increased thermal protection when compared with just Nomex (as used on the groins) or for unprotected skin (head).

For the 2xBCM and 2xATC configurations, as described in sections 5.1.2 and 5.1.5, the upper module exited the storage tube predominately intact and then struck the ceiling scattering unburnt propellant grains inside the crew compartment. The loose, unburnt propellant grains were then ignited initially by burning firebrands, followed by the autoignition of remaining propellant when the ambient temperature exceeded the propellant ignition temperature. For the 2xBCM and 2xATC configurations the bulk of the contents of the lower of the two modules remained in the storage tube and, ignited by the initial ignition event, burned to produce a high intensity flame that emanated from the storage tube. In the 1xTCM configuration, see section 5.1.3, the base of the module separated from the combustible case as the module was propelled out of the storage tube, thus allowing a portion of propellant to remain in the tube. As for the other module configurations this propellant subsequently burned to create a 'flamethrower' effect from the tube.

As described in section 5.1.4, full event sequences for the 3xBCM configuration were not able to be determined from the camera footage. However, unlike the other module configurations, none of the modules in this configuration were observed exiting the storage tube whole. It is postulated that the higher storage tube pressures (see section 5.4.1) and greater level of ignition development for this configuration led to the structural breakdown of the combustible cases before they were able to be ejected from the storage tube.

Figure 36 shows the energy absorption and the burn damage to the skin after 10 s exposure and Figure 37 allows respiratory threshold escape times to be estimated. Using these three criteria the module configurations can be ranked in order of increasing severity from a thermal hazard perspective as follows:

$$2xATC \equiv 2xBCM < 1xTCM << 3xBCM$$

Table 14: Burn charts for different module configurations at (a) 10 s personnel exposure, (b) 30 s personnel exposure

(a) 10 s exposure		**Person A**				**Person B**				**Person C**			
Module	Experiment	Groin	Chest	Back	Head	Groin	Chest	Back	Head	Groin	Chest	Back	Head
1xTCM	3	7	-	-	6,16	7	10	-	6[p]	4,<15[c]	8	10	5,19
2xBCM	4	8	-	-	4,19	6	-	-	6,42	4,19	8	-	5
3xBCM	10	3,16	9	8	2,10	4	9	-	2,10	1,<7[n]	3,10	-	3,12
2xATC	9	8	-	-	6,24	7	-	-	6,19	6,20	10	-	6

(b) 30 s exposure		**Person A**				**Person B**				**Person C**			
Module	Experiment	Groin	Chest	Back	Head	Groin	Chest	Back	Head	Groin	Chest	Back	Head
1xTCM	3	7,25	12	12	6,15	7,22	10	13	6[p]	4,<15[c]	8,29	10	5,16
2xBCM	4	8,32	14	14	4,17	6,23	12	-	6,20	4,16	8	18	5,21
3xBCM	10	3,16	9	8	2,10	4,28	11	18	2,10	1,<7[n]	3,10	14	3,12
2xATC	9	8,20	17	14	6,16	7,21	13	17	6,16	6,16	10	12	6,18

a,b	3rd degree burn, a=time to 2nd degree burn (s), b=time to 3rd degree burn (s)
a	2nd degree burn, a=time to 2nd degree burn (s)
a	1st degree burn, a=time to first degree burn (s)
-	No burn sustained

[c]Cu disc failed at 5.7s at 185[o]C

[n]Cu disc failed at 3.5s at 150[o]C

[p]HFS delaminated at 8.0 s

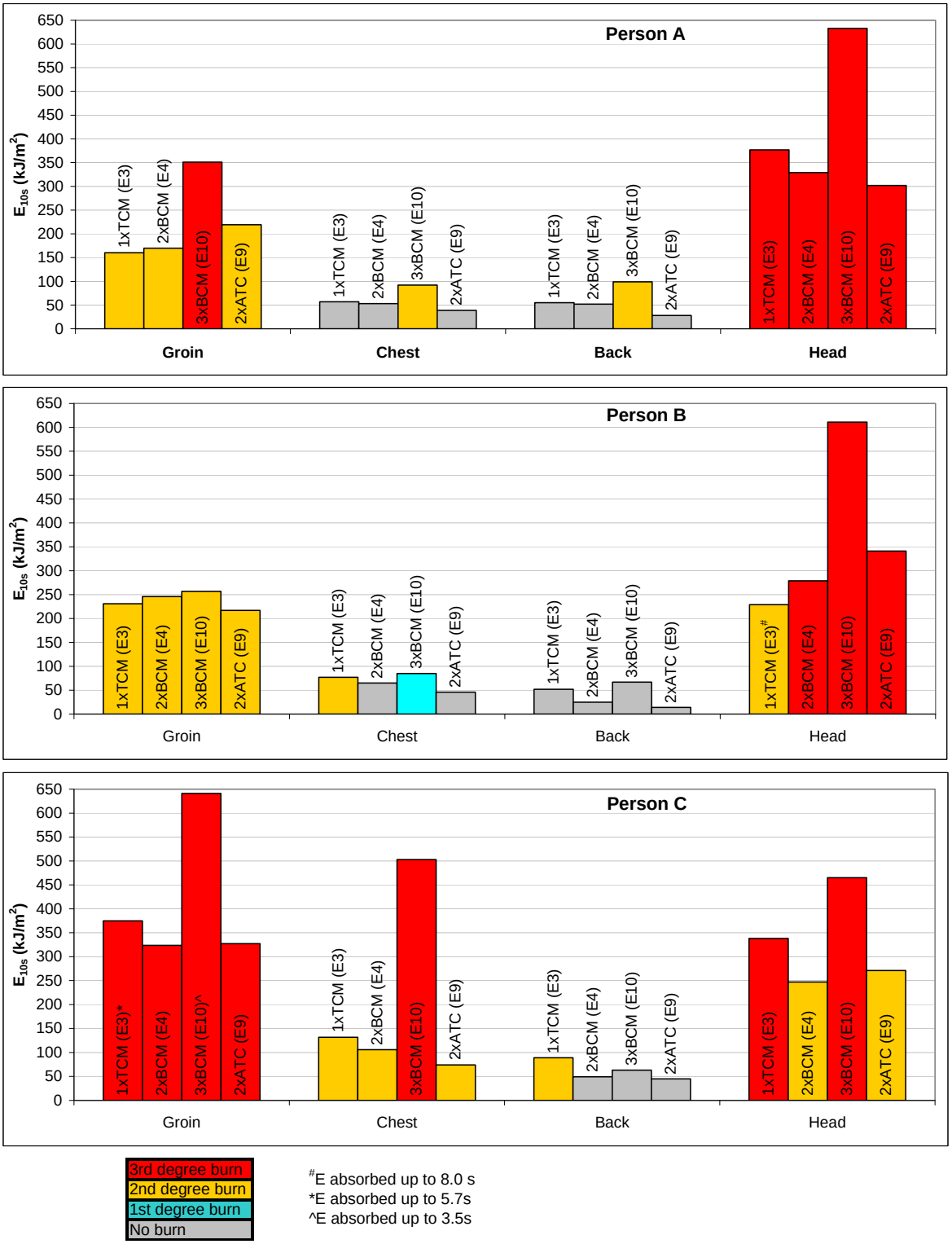

Figure 36: Effect of module configuration on energy absorbed by body part after 10 s exposure.

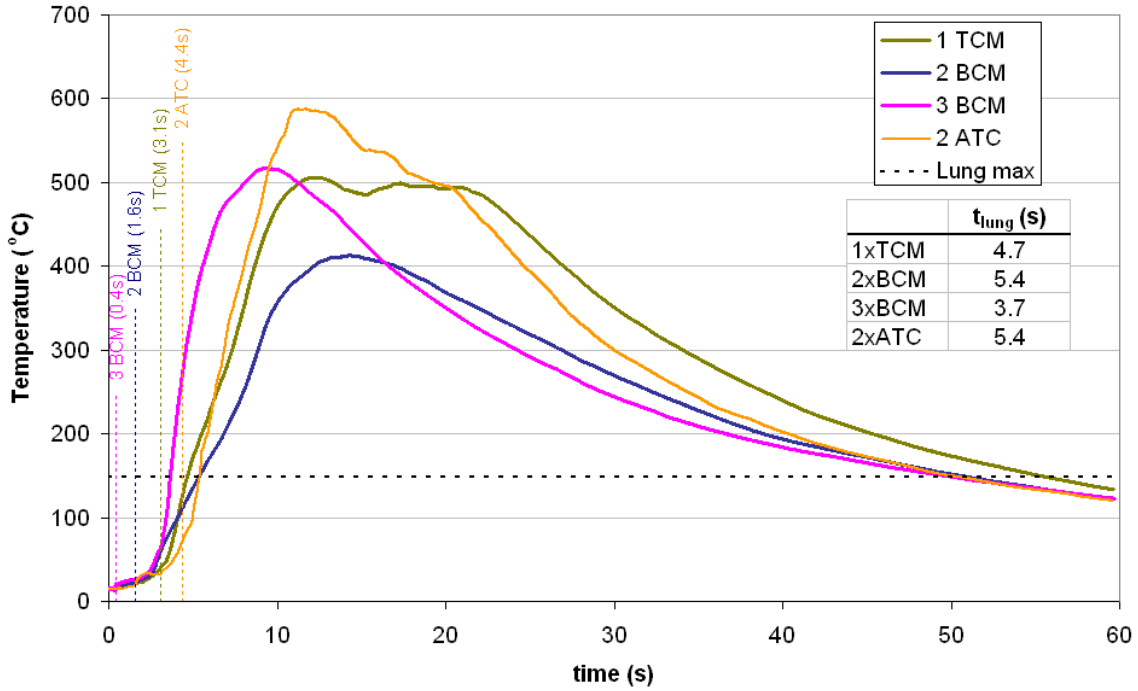

Figure 37: Average crew compartment temperature for the four module configuration types in baseline tests. The vertical dashed lines denote the time at which the vent hatch opened.

For each of the baseline experiments all of the propelling charge material was consumed. This enabled the average rate of energy release to be quantified for each experiment using the chemical energy of the propelling charge and dividing it by the event time[3]. The former is a function of the energetic material constituents of the propelling charge and their mass, the latter is approximated from the camera footage for the experiments in question. Inspection of the data in Table 15 shows a direct correlation between the average rate of energy release and the thermal hazard severity ranking stated above. This highlights the importance of the rate of energy release as a hazard determining factor. Propelling charge module characteristics governing rate of energy release and gasification rates are discussed in section 5.4.1.

Table 15: Importance of propelling charge rate of energy release as a thermal hazard determining factor

Configuration	Chemical Energy (kJ)	Event time (s)	Avg rate E release (kJ/s)	Thermal severity ranking[4]
3xBCM (E10)	31149	9	3461	1
1xTCM (E3)	34744	19	1829	2
2xBCM (E4)	20766	17	1222	3
2xATC (E9)	22748	19	1197	3

[3] Defined as the time from charge ignition through to the cessation of propelling charge combustion.
[4] As determined from: skin burn damage after 10 s; energy absorption after 10 s; and respiratory threshold escape times. On the ranking scale 1=most severe, 3=least severe.

A summary of the major energetic components stored inside the crew compartment and their ignition temperatures, as determined by heating 200 mg specimens in a heating block at 5°C/min, is provided in Table 16 [28]. Figure 37 shows that the ambient crew compartment temperature well exceeds the highest of these ignition temperatures for a period in excess of 30 s. As such, there is a possibility of sympathetic cook-off of munitions stored in the crew compartment, particularly if there are any munitions not stored in protective storage housings.

Table 16: Typical ignition temperatures of the major propelling charge components and likely composition of the HE filled projectiles in the crew compartment [28]

Component	**Temperature of Ignition (°C)**
BCM/TCM propellant	165
ATC propellant	167
Combustible Module Case	170-175
Melt Cast Explosive (60/40 RDX/TNT)	201

A means of determining the probability of burn injury mortality from the surface area of the body affected by a given level of burn damage was described in section 3.1. However, as burns were only evaluated at four locations of the body, to determine a precise probability of death would require many assumptions regarding the burns calculated at the measured positions and how those burn levels translate to burn damage at other areas of the body not fitted with sensors. Whilst, in a number of cases, the magnitude and uniformity of the incident heat fluxes was such that these assumptions could be made with a degree of confidence, a quantitative evaluation of a probability of death is not provided as a part of this work. Rather, a general assessment of the likelihood of survival as a result of the thermal environment is made based upon the aforementioned burn damage parameters and the ambient temperature-time profiles.

From Table 14 and Figure 36, given the percentage of the body surface area of Person C that suffered 2nd degree burns or worse, the likelihood of survival would be minimal irrespective of the module configuration tested. The 3xBCM configuration would cause fatal skin burns for Person A and the same is true for Person B with the 1xTCM configuration. Whilst the sustained skin burns would be extensive, they may not be fatal for Person A against the 1xTCM, 2xBCM and 2xATC configurations or for Person B against the 2xBCM, 3xBCM and 2xATC configurations.

With respect to respiratory burn damage; the potential for ejecta related injury (see section 5.3); and, the possible requirement to operate hot latches on damaged doors and escape hatches, whilst incurring significant skin burn damage, would make the likelihood of escaping the crew compartment before the maximum respiratory escape temperature is reached low for all baseline tests conducted. Hence, from a thermal perspective, the likelihood of crew survival would be low.

5.2.2 Room Confinement

The loss of the vent hatch on the second experiment limited the scope for a thorough investigation of the effect of room confinement on the pressure and thermal environment within the simulated crew compartment. Despite this, a comparative assessment between the minimal confinement case of Experiment 1, where the original vent hatch was pushed shut, with an intermediate confinement case created by bolting a sheet of plywood to the outside of the trials structure (Experiment 4), was made for the 2xBCM configuration. The thermal results for these experiments are provided in Table 17, Figure 38 and Figure 40. Thermal results for a second comparative assessment, made for the 3xBCM configuration, between an intermediate level of confinement (Experiment 10) and a high level of confinement (Experiment 14), achieved by bolting a sheet of plywood to the inside of the trials structure, are provided in Table 18, Figure 39 and Figure 41.

Considering the low and intermediate confinement comparison for the 2xBCM configuration, the data does not show a definitive trend with respect to either skin burn damage or energy absorption. The *average quickness*[5] (Experiment 1=197 MPa/s, Experiment 4=187 MPa/s) and peak tube pressure (Experiment 1=2617 kPa, Experiment 4=2455 kPa), as determined from storage tube pressure data, suggests that initial ignition development was greater for Experiment 1; however the difference is not significant. The presence of the plywood in Experiment 4 affords increased room confinement until the plywood separates from the structure 1.6 s after charge initiation at a pressure of 13 kPag (see Figure 58 in section 5.4.2). The average crew compartment temperature data, presented in Figure 40, shows a near-identical profile for the two experiments for the first 5 s of the events. After this time the rate of temperature rise is greater for Experiment 1.

For the 3xBCM configurations, the higher room confinement afforded by the inner ply (75kPag) allowed greater combustion development and therefore a higher ambient room temperature up until failure of the plywood. The sharp drop in room temperature at 0.8 s for Experiment 14 (see Figure 41) corresponds to failure of the plywood and the subsequent rapid gas outflow from the room. The 10 s energy absorption and 10 s skin burn damage, see Table 18 and Figure 39, suggested that the level of skin burn damage sustained by the three personnel in the crew compartment after 10 s would most likely be fatal irrespective of the level of confinement. The more rapid ambient room temperature rise associated with the increased confinement condition of Experiment 14 reduced the respiratory threshold escape time from 3.7 s for the reduced confinement condition of Experiment 10 to 2.1 s.

[5] Average storage tube *dP/dt* at pressures of 40, 60 and 80% of P_{max}

Table 17: Burn chart for different levels of room confinement for 2xBCM experiments at (a) 10 s personnel exposure, (b) 30 s personnel exposure

(a) 10 s exposure		**Person A**				**Person B**				**Person C**			
Confinement	Experiment	Groin	Chest	Back	Head	Groin	Chest	Back	Head	Groin	Chest	Back	Head
Hatch	1	5	10	9	4,16	6	10	-	5	4	8	-	4,30
Ply	4	8	-	-	4,19	6	-	-	6,42	4,19	8	-	5

(b) 30 s exposure		**Person A**				**Person B**				**Person C**			
Confinement	Experiment	Groin	Chest	Back	Head	Groin	Chest	Back	Head	Groin	Chest	Back	Head
Hatch	1	5	10	9	4,15	6,37	10	-	5,28	4,21	8	12	4,18
Ply	4	8,32	14	14	4,17	6,23	12	-	6,20	4,16	8	18	5,21

Table 18: Burn chart for different levels of room confinement for 3xBCM experiments at (a) 10 s personnel exposure, (b) 30 s personnel exposure

(a) 10 s exposure		**Person A**				**Person B**				**Person C**			
Confinement	Experiment	Groin	Chest	Back	Head	Groin	Chest	Back	Head	Groin	Chest	Back	Head
Ply	10	3,16	9	8	2,10	4	9	-	2,10	1,<7[n]	3,10	-	3,12
Inner Ply	14	2,20	-	10	1,<12[g]	2	18	10	1,10	**No data**[b]	2,11[h]	-	2,10

(b) 30 s exposure		**Person A**				**Person B**				**Person C**			
Confinement	Experiment	Groin	Chest	Back	Head	Groin	Chest	Back	Head	Groin	Chest	Back	Head
Ply	10	3,16	9	8	2,10	4,28	11	18	2,10	1,<7[n]	3,10	14	3,12
Inner Ply	14	2,25	11	10	1,<12[g]	2	10	10	1,10	**No data**[b]	2,11[h]	15	2,10

a,b	3rd degree burn, a=time to 2nd degree burn (s), b=time to 3rd degree burn (s)
a	2nd degree burn, a=time to 2nd degree burn (s)
a	1st degree burn, a=time to first degree burn (s)
-	No burn sustained

[b]Fragment strike

[g]Sensor delaminated at 1.2s

[h]Cu disc hit by ejecta and exposed through clothing

[n]Cu disc failed at 3.5s at 150^{o}C

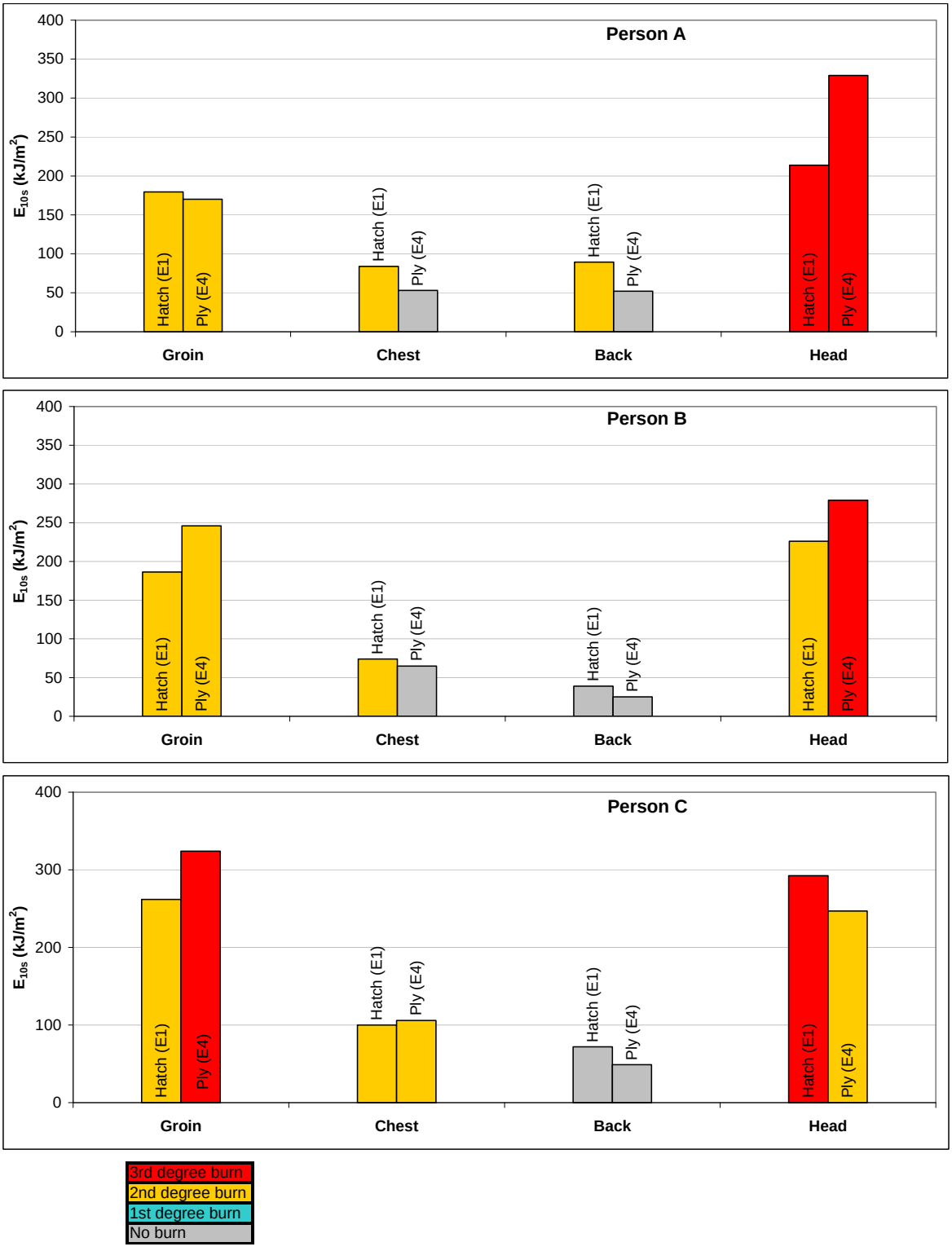

Figure 38: Effect of room confinement on energy absorbed by body part after 10 s exposure for 2xBCM configuration.

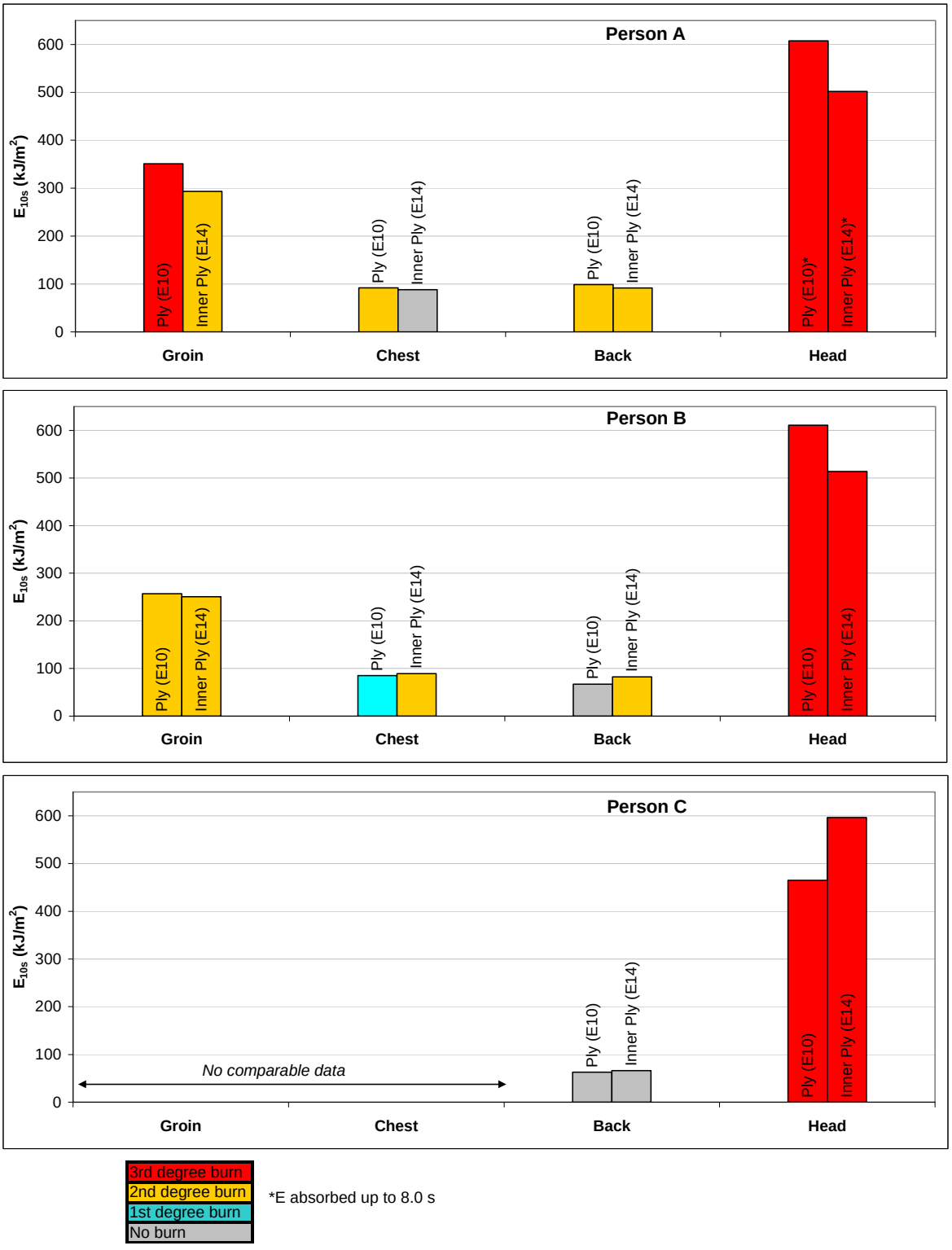

Figure 39: Effect of room confinement on energy absorbed by body part after 10 s exposure for 3xBCM configuration.

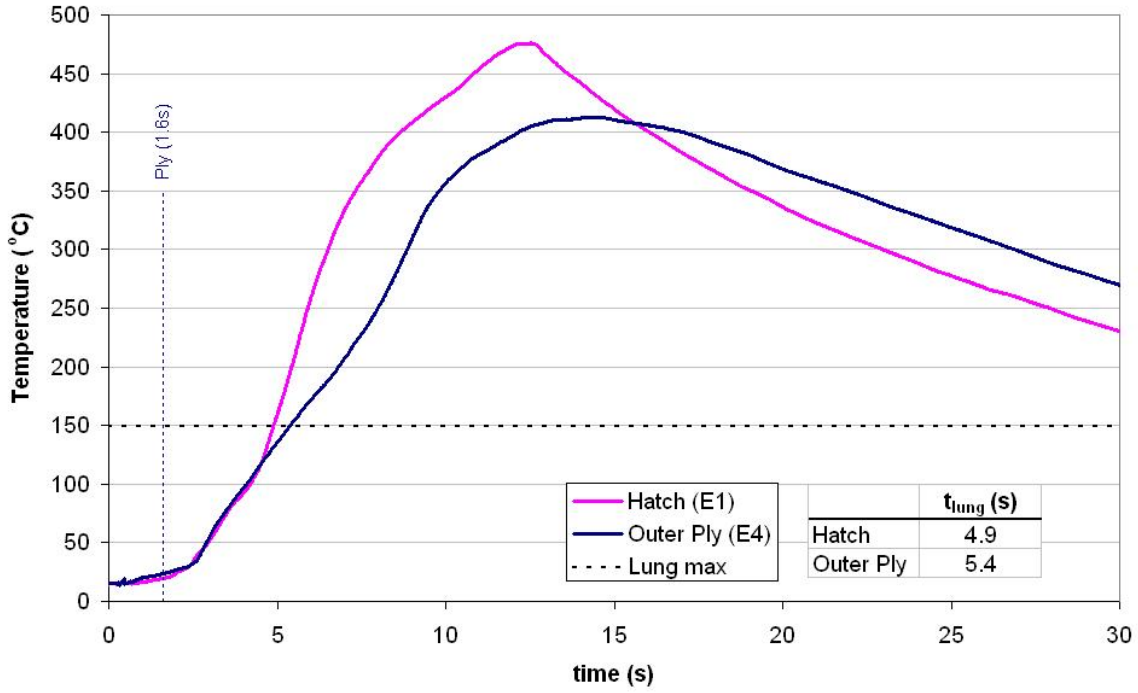

Figure 40: Effect of room confinement on average crew compartment temperature for the 2xBCM configurations. The vertical dashed line denotes the time at which the vent hatch opened.

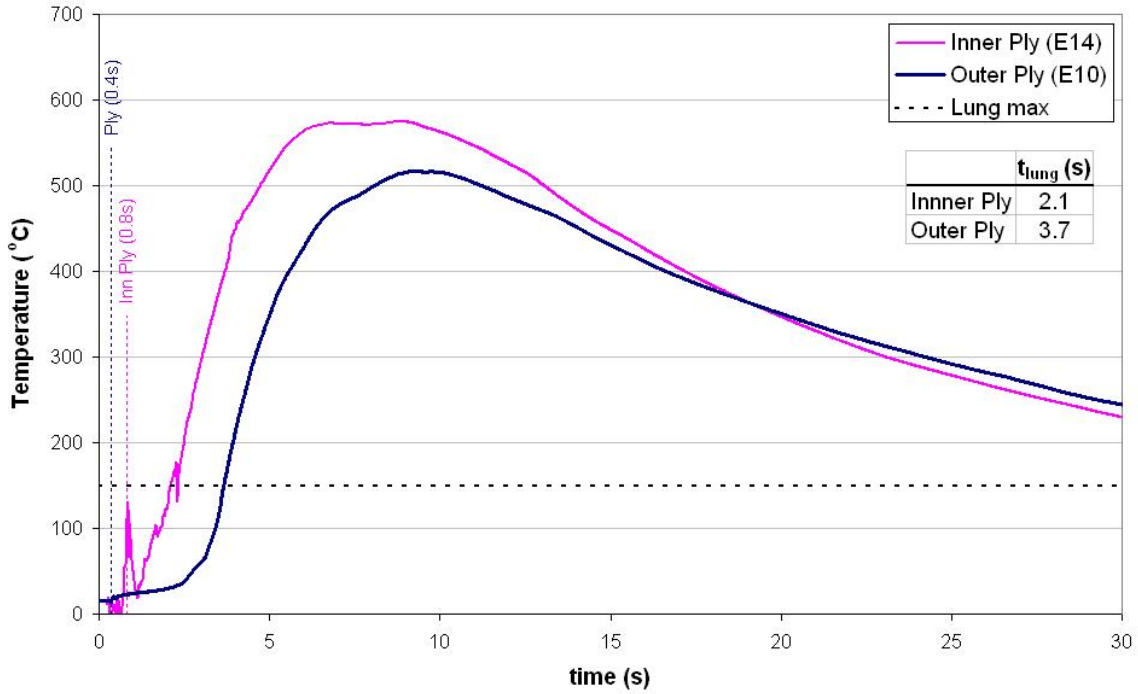

Figure 41: Effect of room confinement on average crew compartment temperature for the 3xBCM configurations. The vertical dashed line denotes the time at which the vent hatch opened.

5.3 Ejecta

5.3.1 Module Configuration

A propelling charge event inside the crew compartment can give rise to a number of sources of ejecta, most common are: unburnt or partially burnt propellant grains; propellant fragments ricocheting off surfaces; whole propelling charge modules; propelling charge module components; storage tube end-caps; and, storage tube fragments in the event of tube fragmentation.

As the ejecta hazard assessment applied in this work is based on kinetic energy thresholds, the ejecta hazard can only be quantified for objects of a known mass and geometry. As such, only unburnt propellant grains and propelling charge modules were considered when quantifying the hazard posed from ejecta. The end-cap was not considered as it was designed to create a realistic level of tube confinement rather than to represent the mass and geometry of an end-cap used in a specific platform.

Observations over the course of the trial suggest that the greatest ejecta threat would be posed by unburnt propellant grains ejected from the storage tube shortly after end-cap failure, when the tube pressure is still high and provides a higher driving force for ejecta acceleration. The propellant grains were generally ejected in a widely distributed fashion (Figure 42(*a*)), further increasing the risk posed, and the impact of the grains with solid surfaces inside the structure at high velocities resulted in the generation of significant quantities of secondary fragments in the form of propellant shards (see for example Figure 42(*b*) and (*c*)). These propellant shards would pose a serious threat to sensitive organs such as the eyes and skin. In addition, for many experimental configurations propelling charge modules were ejected, largely whole, from the storage tubes. Whilst the probability of being struck by a propelling charge module is lower than that of being struck by propellant grains, the consequences would be severe.

In the presented grain velocity versus time curves, the abscissa refers to time since the end-cap first starts to separate from the storage tube. Upon end-cap separation significant obscuration associated with the module flash suppressant, dust, propellant and igniter flash and other materials occurs. Consequently, locating grains that could be positively identified and tracked with an easily identified dimension over a sufficient number of frames to calculate a velocity had to be done opportunistically. As such, the reported grain velocities are not based upon a velocity determined over a certain distance from the tube or at a specific location inside the trials structure. Each data point for the presented grain velocity versus time curves corresponds to the velocity measurement of a unique grain. Conversely, the plots of propelling charge module velocity versus distance from the propelling charge storage tube are based on measurements made for a single, common module.

Figure 42: (a) Ejecta dispersion during Experiment 4, image from view A; (b) Post experiment propellant grain and grain fragments from Experiment 13; (c) Propellant shards lodged in flash bulb reflector, Experiment 13.

Figure 43 summarises the collected grain velocity data for the 2xBCM configuration experiments. An exponential decay model, shown in Figure 43, gave the best fit with the measured grain velocity data. Using this model, propellant grains travelling at potentially lethal velocities were calculated to exit the tube for 7 ms after end-cap separation from the storage tube. Also included in Figure 43 are two grain velocity measurements for a 3xBCM configuration. A combination of the camera frame rates, coupled with the high grain velocities and level of obscuration present upon end-cap separation with the 3xBCM configuration meant that there was less opportunity to accurately identify grains in the camera frames. The level of ejecta damage sustained by the instrumentation boards and also by a witness plate (see Figure 45) used in Experiment 10 (3xBCM) indicated that the hazard posed by unburnt propellant grain ejecta from a 3xBCM configuration. This can be attributed to the higher storage tube pressures (see section 5.4.1) and the likelihood of greater structural breakdown of the modular charges in the storage tube for the 3xBCM configuration.

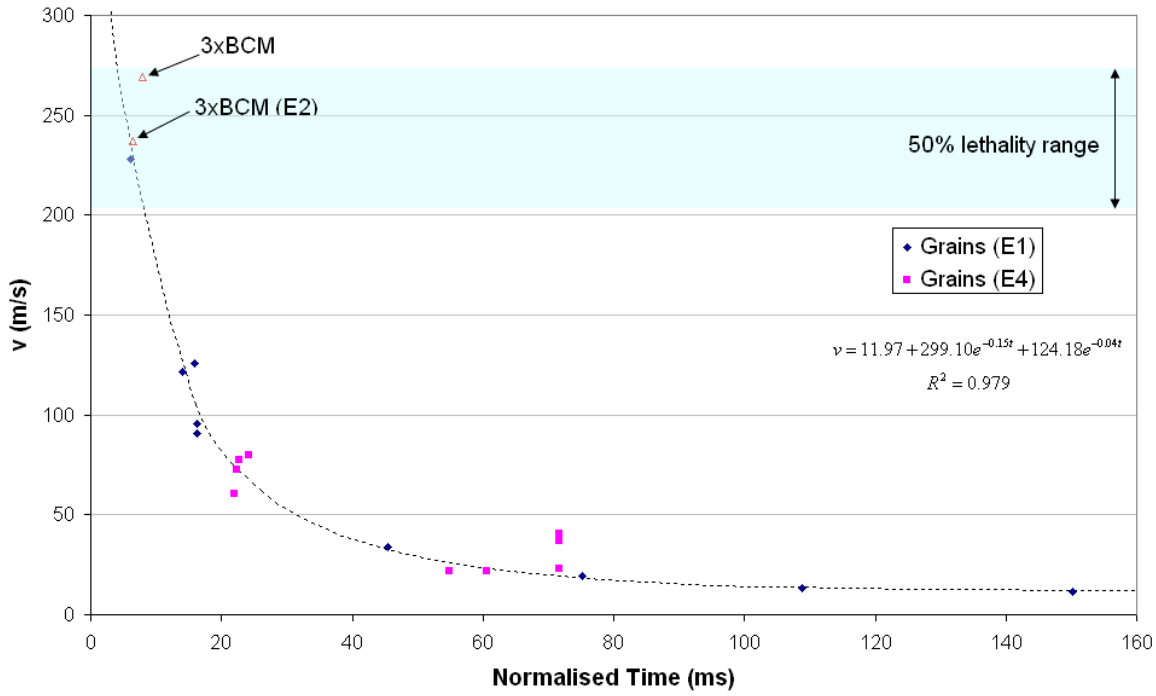

Figure 43: Unburnt grain velocities versus time from end-cap failure for 2xBCM configurations. Two data points for 3xBCM configuration grain velocities are also included. 50% lethality range calculated using blunt force trauma correlation of [20].

Figure 44 summarises the propelling charge module velocity data collected for the 2xBCM configuration of Experiments 1 and 4. In each case, the velocity data corresponds to the upper of the two modules in the storage tube. Impact from the ejected module in Experiment 1 would pose a high mortality risk, whereas a high chance of survival would be anticipated for the module velocity of Experiment 4.

Separation of the propelling charge module base from the module body was observed in a number of experiments. This allows the loss of propellant grains and other module

components as the module moves away from the storage tube. Whilst it is not possible to quantify the associated reduction in module mass, in the case of Experiment 1 the module would need to lose 50% of its mass to fall below the 50% lethality range. Images of the module as it traversed the trials structure suggested that such a loss in mass was unlikely.

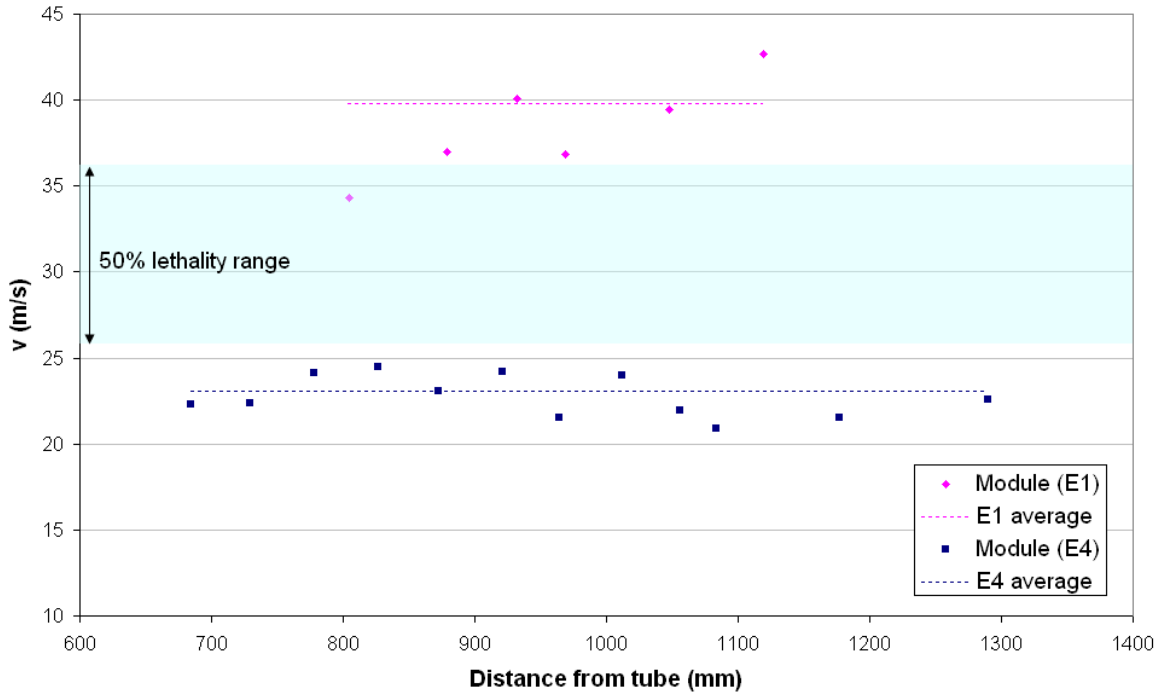

Figure 44: Module velocity as a function of distance from the propelling charge storage tube for the 2xBCM configurations of Experiment 1 and 4. 50% lethality range calculated using blunt force trauma correlation of [20].

The level of propellant grain dispersion from the storage tube for the 3xBCM event is illustrated in Figure 45. Shown in the figure is a photo of the aluminium witness plate that was positioned alongside Person C. The 1.2 m long witness plate was positioned such that its base was below the groin and the top of the plate extended past the position of the head. Ejecta penetration of the witness plate was limited by the plates 8 mm standoff distance from the ceiling of the structure. Had the standoff distance been greater, it is anticipated that significantly more plate penetration would have occurred. The comparatively low level of damage on the sides of the witness plate was due to protection afforded by the position of the plate relative to Person A and Person C. The onset and/or continuation of propellant burning after penetrating through the plate, as evidenced by charring on the back face of the witness plate, adds an additional thermal risk to personnel. Evidence of propellant grains penetrating through the clothing on the instrumentation boards and then either being ignited by the ambient temperature, or continuing to burn after penetration, was also noted for a number of experiments. An example is provided in Figure 46.

Figure 45: 1 mm thick 1.2 x 0.9 m Al witness plate used to assess ejecta dispersion for a 3xBCM configuration, Experiment 10. LHS image: witness plate viewed from behind. RHS image: view from front. Distance from top of propelling charge storage tube to witness plate was 1914 mm.

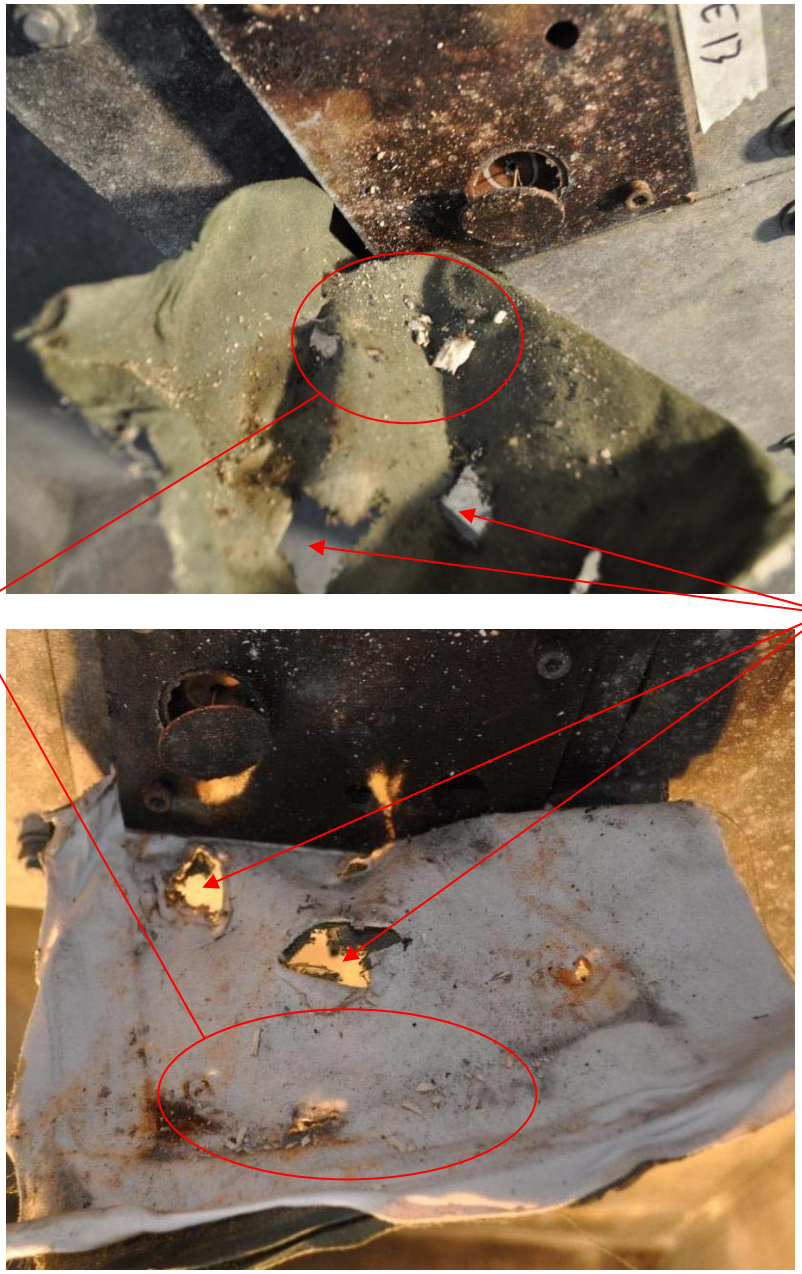

Figure 46: Propellant penetration through the clothing of Person C groin (top) and chest (bottom). Photo from Experiment 13.

Whilst no witness plates were used for the 2xBCM configurations, photographs of the ceiling after Experiment 1 (Figure 47) clearly showed marks left by the high velocity impact of propellant grains and gave an indication of the dispersion of high velocity propellant. The clear demarcation of propellant marks (see bottom of the photograph) on the ceiling was due to protection afforded by Person C.

Figure 47: Propellant impact marks on the ceiling of the trials structure parallel to the chest and groin position of Person C, Experiment 1.

Grain velocities and module velocity for the 1xTCM configuration are presented in Figure 48 and Figure 49 respectively. Owing to the larger mass of the TCM grains and the TCM itself relative to the BCM components, lower velocities are required to achieve a given lethality level. From the curve of best fit, shown in Figure 48, propellant grains travelling at potentially lethal velocities exited the storage tube up to 17 ms after end-cap separation. The average module velocity, as shown in Figure 49, exceeded the upper 50% lethality velocity by approximately 14 m/s. At the measured velocity, the TCM would still fall within the 50% lethality limit even if 80% of its mass was lost prior to impact.

Photographs of the witness plate used in Experiment 13 for the 1xTCM configuration are shown in Figure 50. The view of the back of the witness plate shows burn marks from propellant grains that have continued to burn after penetrating through the witness plate. Whilst discharge of the AFESS obscured the view of the cameras, the large tear at the bottom of the witness plate (as viewed from the front) was most likely a result of impact from either the propelling charge module or the storage tube end-cap. A section of the witness plate in-situ is shown in Figure 51. Ejecta damage to the chest and groin of Person C is also clearly evident in the figure.

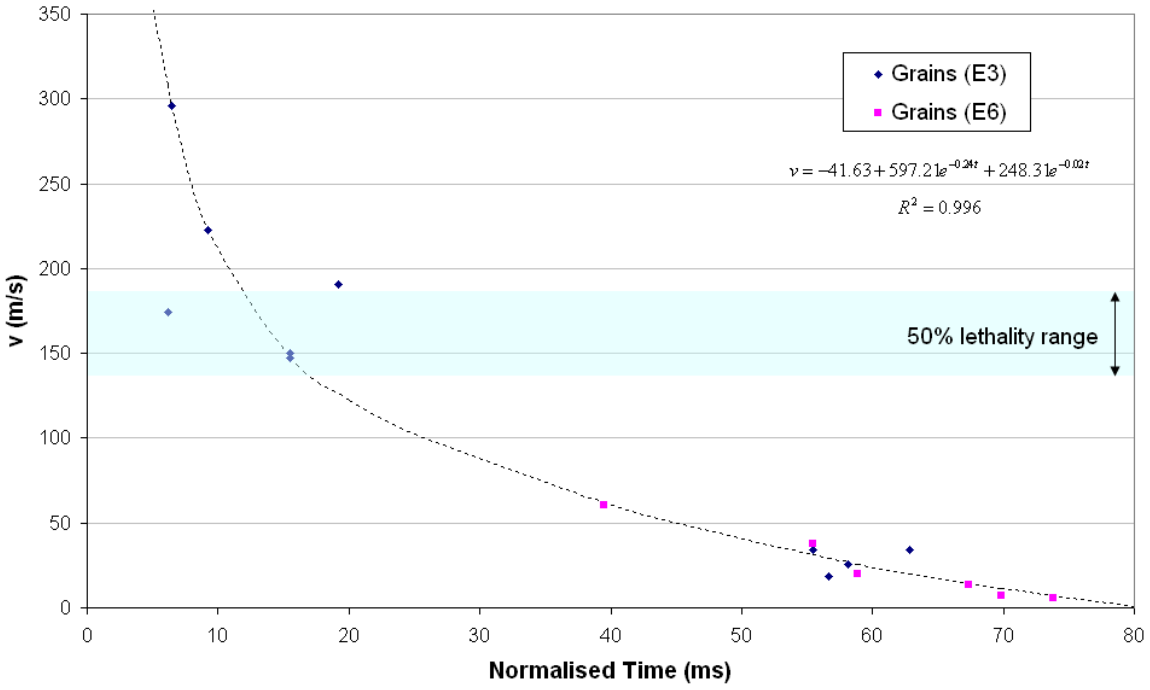

Figure 48: Unburnt grain velocities versus time from end-cap failure for 1xTCM configurations[5].

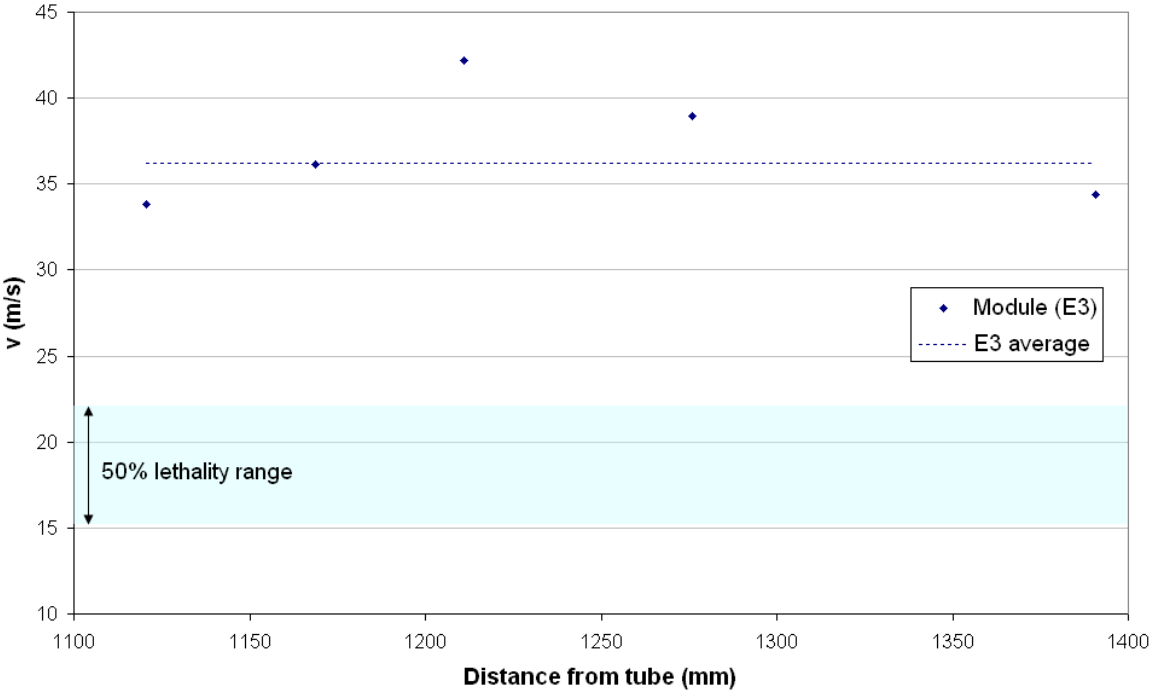

Figure 49: Module velocity as a function of distance from the propelling charge storage tube for the 1xTCM configuration of Experiment 3[5].

[5] 50% lethality range calculated using blunt force trauma correlation of [20].

Figure 50: 1 mm thick Al witness plate used to assess ejecta dispersion for a 1xTCM configuration, experiment 13 at a distance of 1014 mm from the top of the propelling charge storage tube. LHS image: witness plate viewed from behind. RHS image: view from front.

Figure 51: Ejecta damage to Person C in Experiment 13

Unburnt grain velocity measurements for the 2xATC configuration in the early stages after end-cap separation were not possible due to obscuration of the camera images. The curve of best fit for the grain velocities is provided in Figure 52. Extrapolation of the selected decay model to time zero indicates that unburnt grains are unlikely to pose a life threatening risk for this configuration. This is supported by the reduced damage sustained by the witness plate in Experiment 9 when compared with the 3xBCM and 1xTCM configurations (see Figure 53). Camera footage of Experiment 9 confirmed that the deeper of the two circular impressions in

the witness plate was caused by impact from the ejected ATC module; the second, lighter circular impression on the witness plate was due to impact of the end-cap.

A number of decay models give an adequate description of the measured ATC grain velocity data with comparable R^2 values. However, the predicted grain velocity as the time approaches zero varies with the selected decay model. For example, an alternative decay model, with an R^2 value of 0.97, predicts a grain velocity of 400 m/s at t=0 s. More data, either generated from further experiments or from validated modelling, would aid in the selection of the most appropriate model.

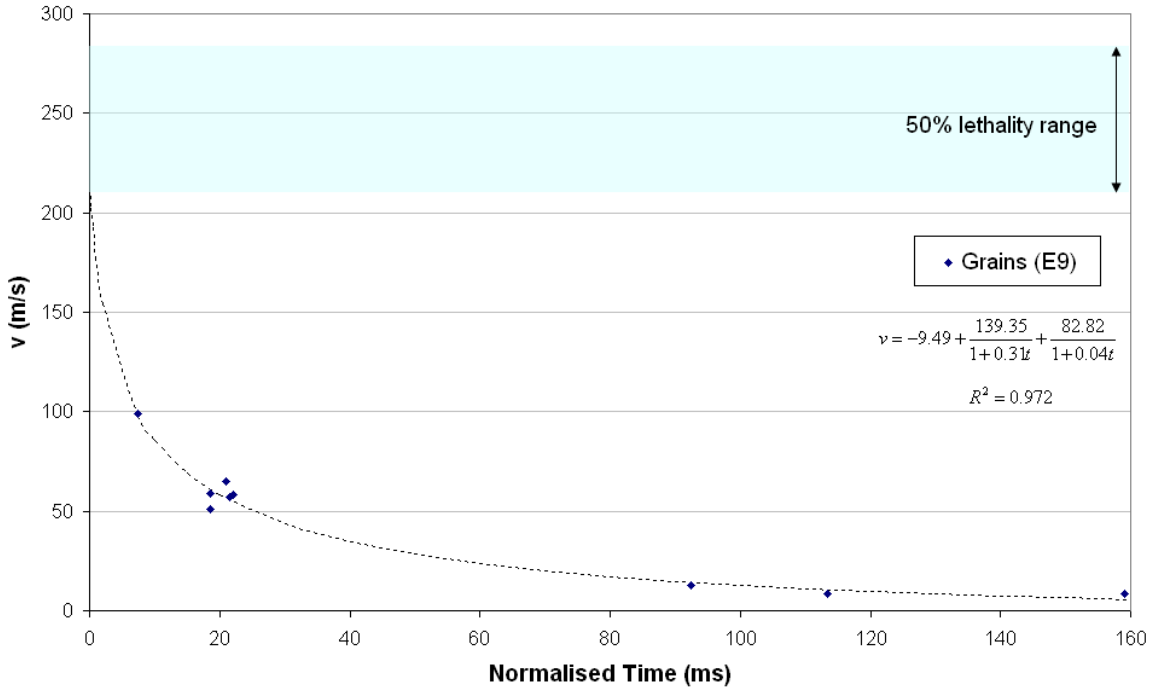

Figure 52: Unburnt grain velocities versus time from end-cap failure for 2xATC module configurations. 50% lethality range calculated using blunt force trauma correlation of [20].

Figure 53: 1 mm thick Al witness plate used to assess ejecta dispersion for a 2xATC configuration, Experiment 9. RHS image shows close up view of the two circular impressions left by the module and end-cap. Distance from top of propelling charge storage tube to witness plate was 1914 mm.

As shown in Figure 54, the average ATC module velocity exceeded the upper 50% lethality bound. At the measured velocity, the module could lose 60% of its initial mass before falling below the 50% lethality range.

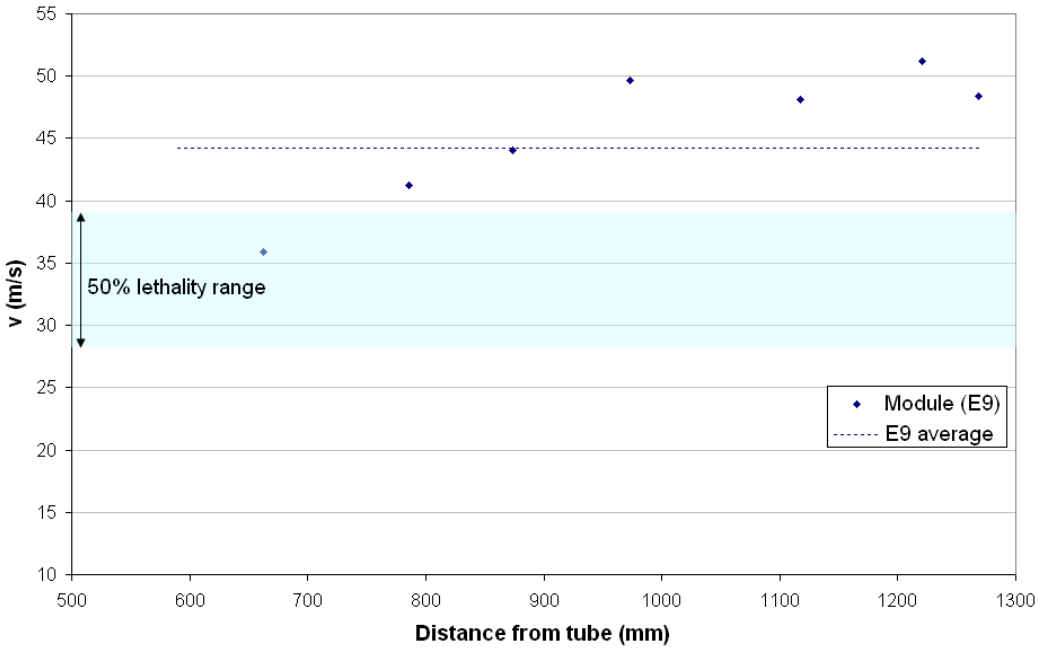

Figure 54: Module velocity as a function of distance from the propelling charge storage tube for the 2xATC module configuration of Experiment 9. 50% lethality range calculated using blunt force trauma correlation of [20].

5.4 Pressure

5.4.1 Module Configuration

Figure 55 compares representative storage tube pressure data of the BCM and TCM configurations tested under baseline conditions and Table 19 provides a direct comparison of the nature of the ignition event for the baseline experiments where tube pressure measurements were made. In the table, *average quickness* is defined as the average storage tube *dP/dt* at 40, 60 and 80% of the peak tube pressure (P_{max}) and provides a measure of the rate of gas generation relative to the free volume of the tube. dP/dt_{fall} gives the rate of tube depressurisation, corresponding to the time from the maximum tube pressure to when the pressure drops to 50 kPag. The storage tube pressure-time trace for the ATC configuration, filtered at 50 Hz, is provided in Figure 56. End-cap separation occurred at 485 ms for the 2xATC configuration. For all of the experiments summarised in Table 19, the end-cap was ejected from the tube whole and the pressure peaks for each of the experiments in Figure 55 correspond to the time at which separation of the end-cap from the storage tube occurred. The periodic oscillation at 50 Hz observed in all storage tube pressure-time traces is due to mains noise induced in the signal due to the need to ground the piezoelectric PCB pressure gauge. Note that Experiment 2, involving a 3xBCM configuration, is not included in this section as the pressure results for this experiment were markedly different to all other experiments conducted over the course of the trial. Results from Experiment 2 are discussed separately in section 5.5.

Open-air igniter tests (see section 5.1.1) showed that bulk propellant is exposed to hot combustion products from the match-head through holes in the centre-core of the combustible case as early as 13 ms after match-head initiation (open air ignition test configuration 3). A delay time from match-head ignition to centre-core igniter material ignition of approximately 170 ms was also observed (open air ignition test configuration 2). Storage tube end-cap failure occurred after both of these events for all module configurations tested, see Table 19. Consequently, the *average quickness* and P_{max} for the BCM and TCM configurations are a function of the following variables:

- *Storage tube free volume*: The 3xBCM and 1xTCM configurations have a comparable storage tube free volume that is approximately 30% smaller than the 2xBCM configuration. The reduced free volume promotes an increased rate of tube pressurisation. Higher storage tube pressures also increase the burn rate of the energetic material in the tube, thus further enhancing the effect of reduced free volume on tube pressure.

- *Propellant grain form*: The BCM and TCMs contain propellant of the same formulation, but the TCM grains are larger and have a more progressive burning geometry. As a consequence, in an unfractured state and if uniformly ignited, the BCM propellant will have a higher rate of gas generation and also liberate more energy in the early phases of the combustion cycle. Propellant grain form also affects propellant bed packing characteristics and therefore the permeability of the bed to gas flow from the igniter

and initial, localised bulk propellant combustion. The larger grains of the TCM will give greater bed permeability when compared with the BCMs.

- *Centre-core igniter material mass and configuration*: The 3xBCM and 1xTCM configurations have a comparable total mass of centre-core igniter material. However, for the 3xBCMs, the centre-core igniter material in each module is separated by adhesive tape placed on either end of the modules. This compartmentalised confinement in the 3xBCM case will affect the flame spread through the centre-core and into the bulk propellant. The 3xBCM configuration also has 12 holes in the centre-core (four per module) compared with four in the 1xTCM configuration and this provides an increased number of bulk propellant ignition sites in the former. The 2xBCM configuration has a smaller quantity of both centre-core igniter material and bulk propellant than the 1xTCM configuration, but this will be offset by the greater number of centre-core holes in the 2xBCM configuration (eight compared with four).

The net effect of these interrelated variables accounts for the differences in the storage tube pressure data for the BCM and TCM configurations, as shown in Figure 55 and Table 19.

The design of the ignition train used in the ATCs is different to that of the BCM and TCMs. It consists of black powder coated propellant attached to the outer diameter of the centre-core with a black powder filled bag located around this coated propellant halfway along the length of the centre-core. The different ignition train of the ATC could account for the different shape of the storage tube pressure versus time plot for this configuration (see Figure 56). The storage tube pressure-time profile for the 2xATC configuration correlates with observations made from the camera footage, see section 5.1.5.

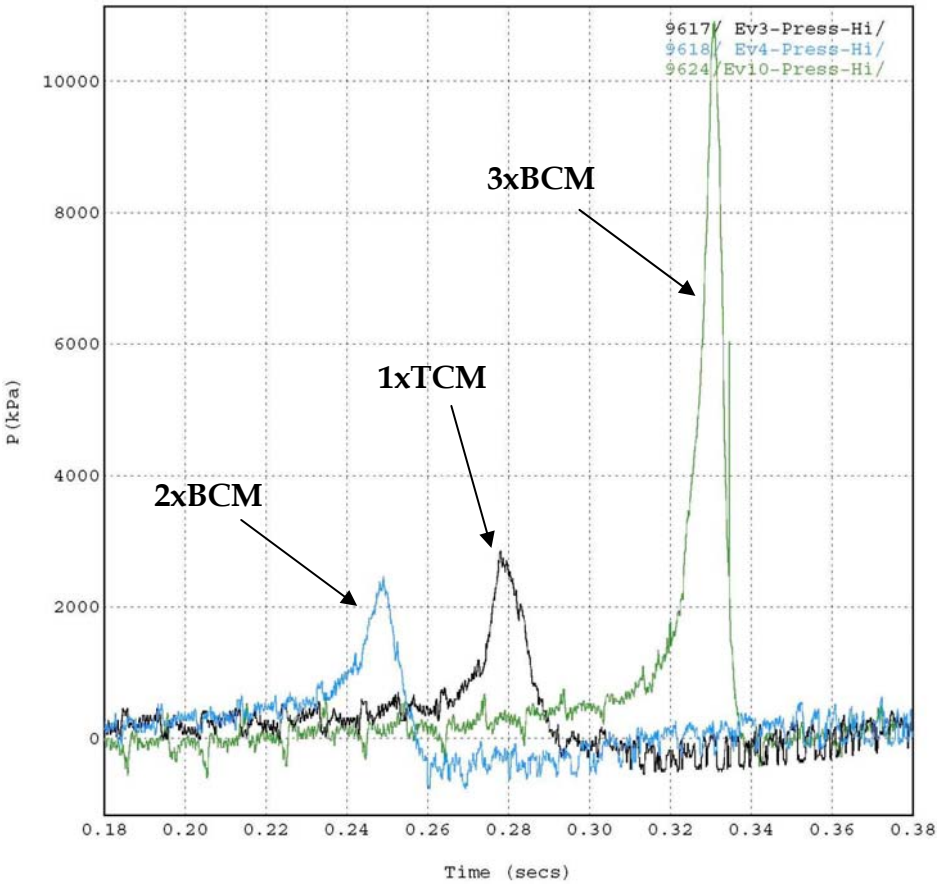

Figure 55: Representative storage tube pressure measurements for the three module configurations tested under baseline conditions

Table 19: Effect of module configuration on storage tube pressure

Module	**Experiment**	**P_{max} (kPa), (std deviation)**	***Avg Quickness* (MPa/s), (std deviation)**	***dP/dt*$_{fall}$ (MPa/s), (std deviation)**	***End-cap fail (ms), (std deviation)***
1xTCM	3,6	2641 (298)	343 (53)	-202 (2.4)	232 (64)
2xBCM	1,4,5,8	2695 (201)	225 (43)	-311 (53)	239 (24)
3xBCM	7	15759 (-)	3344 (-)	-2844 (-)	242 (-)
3xBCM	10	10906 (-)	1423 (-)	-1693 (-)	323 (-)
2xATC	9	3383 (-)	90 (-)	-4.2 (-)	485 (-)

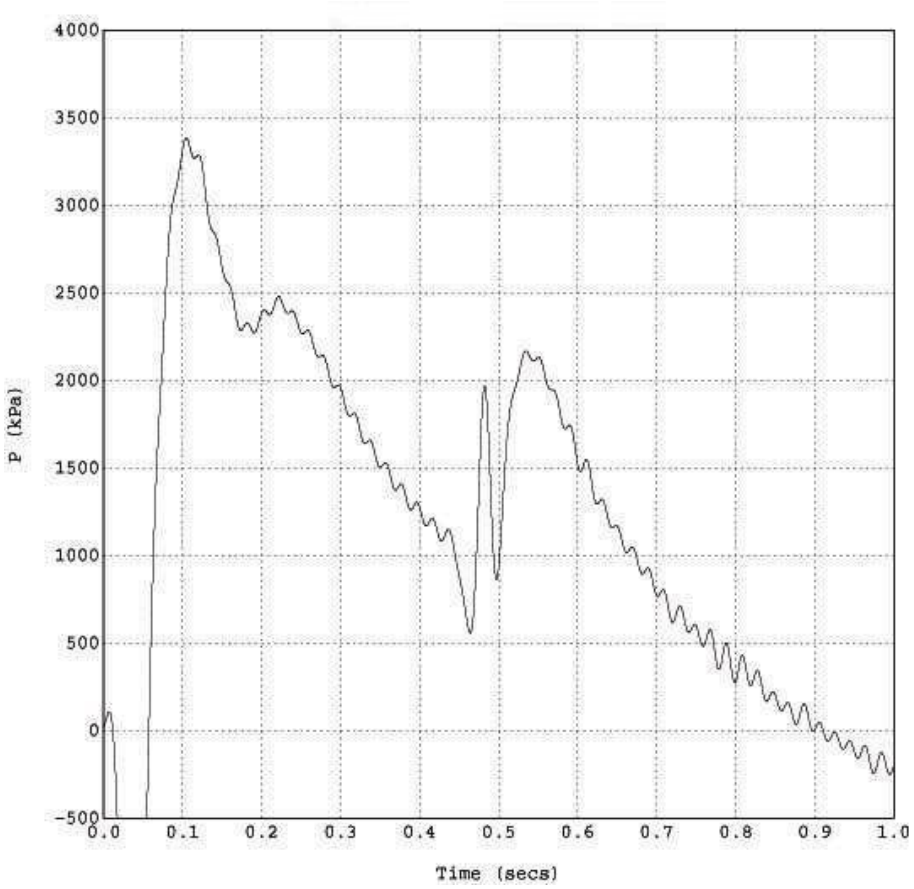

Figure 56: Storage tube pressure data, filtered at 50Hz, for the 2xATC configuration, Experiment 9.

The crew compartment pressure-time profile is a function of the propellant gasification rate and the heat generated from the combustion reaction. The gasification rate is determined by the surface area of the propellant (and how it varies with time) and the linear burning rate of the propellant which is determined by the propellant formulation, pressure and temperature.

At the low pressures at which propellant combustion occurs in the crew compartment, the propellant in the BCM and TCM has a higher linear burn rate than the propellant used in the ATC modules [28]. With respect to initial grain geometry, the propellant in the TCM is significantly larger and has a more progressive burning geometry than the propellant used in the BCM. Similarly, the propellant in the ATC modules has a more progressive burning geometry than does the propellant used in the BCM. The net effect of these burn rate and surface area differences is that, at low pressures and in the early stages of propellant combustion, the gas generation rate for an equivalent propellant mass would increase in the order:

ATC<TCM<BCM

This is supported by Figure 57 where the 2xATC configuration takes the longest time to generate the 13 kPag required to blow off the plywood hatch on the simulated crew compartment, followed by the 1xTCM and then 2xBCM configuration. The rate of gas

generation (and energy release) is highest for the 3xBCM configuration, with door failure occurring at 0.4s for Experiment 10. Whilst the initial portion of the pressure-time traces varies with position owing to the complex pressure environment created in the crew compartment at the time of, and shortly after, storage tube end-cap failure, these spatial differences become small by the time sufficient pressure is generated to blow off the vent hatch. The pressure time traces presented in Figure 57 for the back of Person A were found to be representative of the pressure measurements made at other locations in the crew compartment at the time of end-cap failure. The exception to this is the more dynamic 3xBCM case where vent hatch failure occurred 0.4 s after end-cap failure, in this instance the crew compartment pressure profile is less uniform at the time of vent hatch failure. However, the significantly higher peak pressures and shorter times to vent hatch failure for this configuration support the aforementioned conclusions regarding charge gasification rates.

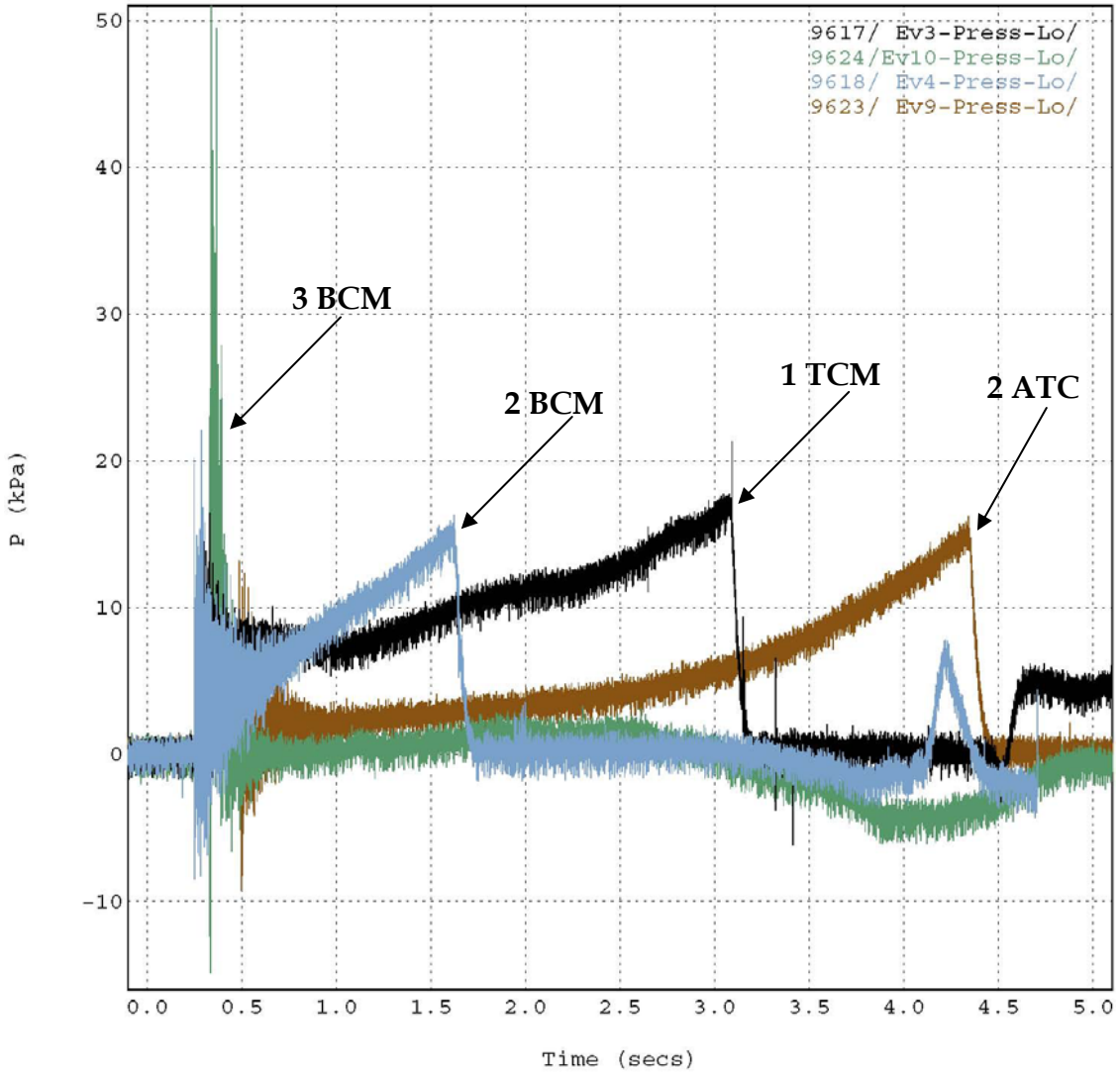

Figure 57: Crew compartment overpressure, as measured on the back of Person A, for the four module configurations tested.

The intrathoracic overpressure assessment methodology, described in section 3.2, was applied to the pressure-time curves collected at each of the body positions where the pressure sensors were functional for the 3xBCM configurations, as it was these experiments that created the most dynamic pressure environments. Results from this analysis for Experiment 10 gave a maximum chest wall velocity of 1.9 m/s for Person C, see Table 20. This gives an *ASII* value of 0.06 which corresponds to no intrathoracic overpressure effects. Whilst a large number of pressure sensors were not functional for this experiment due to a progressive loss of sensors over the course of the trial, a higher order 3xBCM event (Experiment 2, see section 5.5) than that observed in Experiment 10 showed the most severe intrathoracic overpressure injuries to fall in a 'trace to slight' category. Hence, for the baseline tests presented in Figure 57, it can be concluded that the pressure environment inside the crew compartment will not be life-threatening, and indeed, only the 3xBCM configuration would pose a risk of non-life threatening injuries such as auditory damage. However, the effect of the pressure wave, coupled with the bright flash and noise generated upon end-cap failure may result in disorientation, or other physiological responses, that could impede the egress of the crew.

Table 20: Intrathoracic overpressure effects for Experiment 10. Damage to the pressure sensors over the course of the trial limited the available pressure data for this experiment.

Person	***A***		***B***		***C***	
Location	***CWV*(m/s)**	***ASII***	***CWV*(m/s)**	***ASII***	***CWV*(m/s)**	***ASII***
Front	No data		No data		No data	
Back	1.3	0.03	No data		No data	
Right side	No data		0.8	0.02	1.0	0.02
Left side	1.2	0.03	No data		1.9	0.06

5.4.2 Room Confinement

A comparison between room pressures for the minimal confinement case, achieved by having the trial structures original vent hatch pushed shut (Experiment 1), and the intermediate confinement case achieved by bolting a sheet of plywood on the outside of the trial structure (Experiment 4), is made for a 2xBCM configuration in Figure 58.

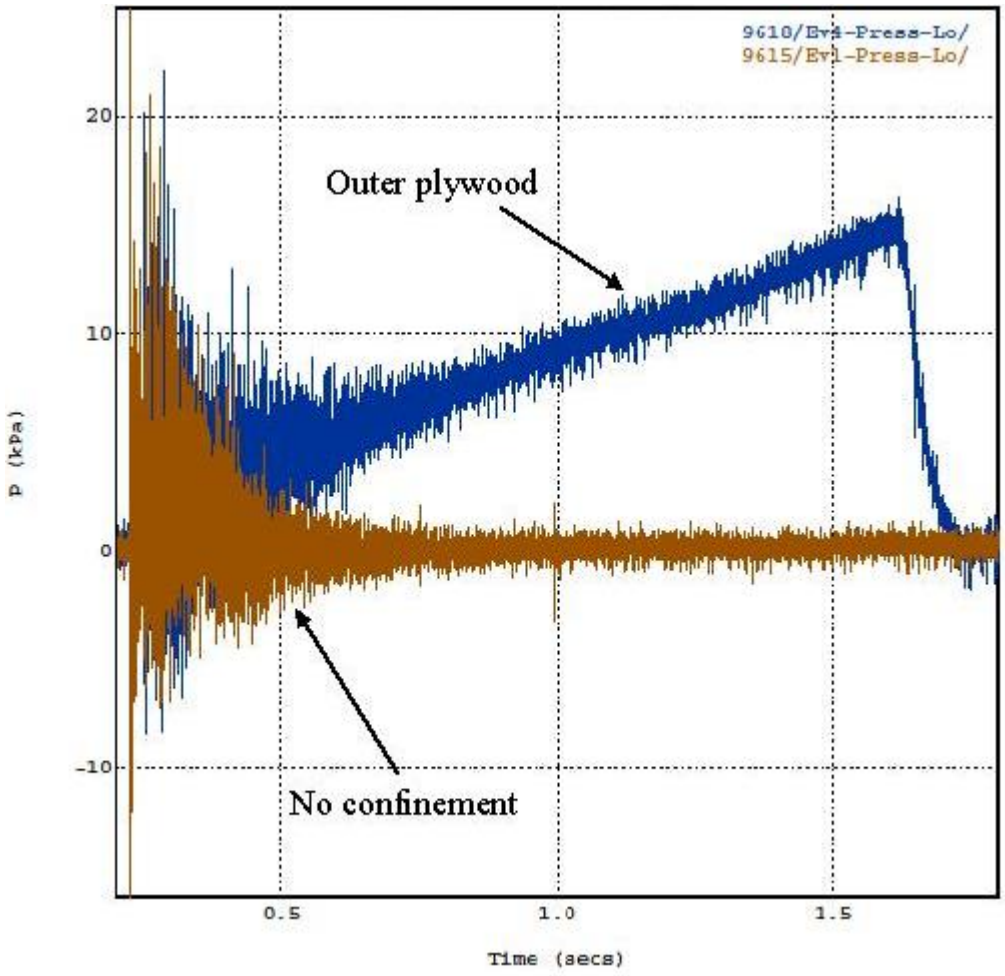

Figure 58: Crew compartment overpressure for the low and intermediate confinement cases of Experiment 1 (brown) and Experiment 4 (blue), 2xBCM configuration.

Storage tube pressure data for Experiment 1 and 4 gave a peak pressure of 2.6 and 2.5MPag, respectively. Given the similarity between the storage tube pressures at the time of end-cap failure for the two events there was a minimal difference between the magnitude of the initial pressure waves experienced by the personnel. The use of the plywood allowed a steady pressure rise in the room until a pressure of 13 kPag was reached after approximately 1.6 s, at which time the plywood was blown off the structure.

The aforementioned 13 kPag confinement level represents a confinement level that would fall at the lower end of the range between platform escape hatches or rear access door pulled closed, but not locked, and the 45 kPag static confinement level predicted from modelling to fail a locked rear-access door. As the 13 kPag pressure is below the threshold level for any pressure related injury, it is only the pressure waves generated at, and shortly after, storage tube end-cap failure that need to be considered. For the 2xBCM configuration the peak storage tube pressures were too low to cause any serious pressure-related injuries upon storage tube venting.

The effect of intermediate (Experiment 10) and high (Experiment 14) crew compartment confinement on pressure development is shown in Figure 60, section 5.5. For the high confinement case, vent hatch failure occurred at 75 kPag approximately 0.5 s after end-cap separation from the storage tube. Taking into consideration the effect that the applied dynamic loading rate would have on the observed failure pressure of the vent hatch, the confinement afforded by the inner plywood in Experiment 14 would likely be similar to that predicted by modelling for the rear access door of the platform in the locked position.

For both 3xBCM confinement cases, application of the overpressure hazard prediction models gives *ASII* values falling in the 0.0-0.2 range, corresponding to no intrathoracic overpressure injuries. The peak pressures for Experiments 10 and 14 do exceed the minimum threshold for eardrum rupture, so non-life-threatening injuries, such as auditory damage, could be sustained.

5.5 Experiment 2

Experiment 2 involved the testing of a 3xBCM configuration with the original trial structure vent hatch pushed shut. This experiment was one of four conducted where the 3xBCM configuration was confined in the storage tube with an end-cap.

The propelling charge response in Experiment 2 was markedly different to the other experiments conducted over the course of the trial. The propelling charge response for Experiment 2 was a higher order event: the storage tube was split into two pieces; the fragment ring sitting around the storage tube was buckled; the four M10 bolts holding the fragment ring to the floor were sheared off; and the hinges used to mount the vent hatch to the trials structure were sheared off. The pressure generated inside the crew compartment created sufficient force upon expanding through the vent area to displace the 13.5 tonne steel trials structure, sitting on a concrete apron, by approximately 90 mm. The force of the exiting gas also knocked over and displaced a series of 1.6 tonne pendine blocks positioned around the vent hatch.

Photographs of the trials structure post-test are provided in Figure 59.

Unfortunately, due to cabling damage incurred in the previous experiment, storage tube pressure measurements were not made for Experiment 2 thus preventing a comparison with the initial stages of the ignition cycle of the other 3xBCM configurations. Measured peak tube pressures for the other 3xBCM configurations with end-cap, Experiment 7 and 10, were 15.8 and 10.9 MPag respectively. This compares with the predicted tube burst pressure range of 13-30 MPag. If, as suggested by the more dynamic nature of Experiment 2, propelling charge ignition developed more rapidly than for Experiments 7 and 10, the predicted tube burst pressure could have been exceeded.

Camera footage of Experiment 2 showed that the storage tube was still intact 7 ms after end-cap failure. Whilst the camera image is partially obscured by initial ejecta and cloud of modular charge flash suppressant, a bright flash at this time likely corresponds to the failure

of the propelling charge storage tube. The brightness of the propelling charge fire completely washes out the camera images between 384 and 1128 ms, thus preventing a definitive statement about the time of storage tube failure. Photographs of the storage tube and sympathetic tube post-test are provided in Figure 59(*b*). The significant denting at the bottom of the sympathetic tube would lead to propelling charge module fracture. Depending on the time-scales over which damage to the sympathetic tube occurred, sufficient localised shear rates could be generated within the energetic material components to cause charge initiation. Alternatively, the damage to the adjacent storage tube may compromise the initial thermal protection that would otherwise be afforded to the propelling charge modules, thus reducing the time before sympathetic cook-off is likely to occur.

Experiment 2 represented the most dynamic event observed in the trial, generating the most severe pressure environment in the crew compartment with a quasi-static pressure of approximately 150 kPag measured on the simulated personnel approximately 450 ms after match-head initiation, see Figure 60. The pressure transducer on the right hand side of Person A, closest to the storage tube, was destroyed shortly after end-cap failure, thus preventing the intrathoracic overpressure effects at this location from being calculated. A summary of the CWV's and corresponding *ASII* values at the other positions is provided in Table 21. In the table, values in red correspond to an intrathoracic injury level of 'trace to slight'; all other values correspond to no intrathoracic injury. Based on this data, the pressure environment will not cause life threatening injuries at the positions where data was collected.

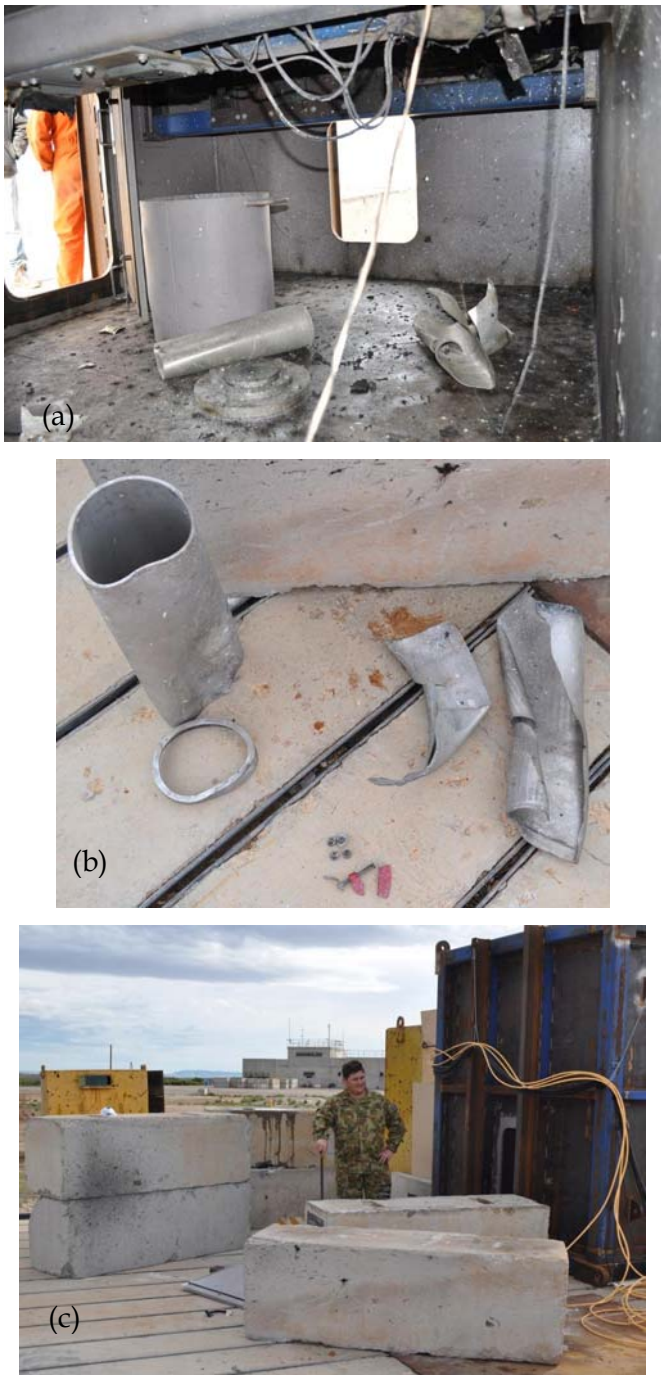

Figure 59: Experiment 2 (a) location of storage tube, split into two pieces, sympathetic tube and fragment ring post-test. (b)Damage to sympathetic tube and storage tube, deformed end-cap sealing ring, 4x sheared M10 bolts and fragmented G-clamp used to hold sympathetic tube to fragment ring also shown. (c) Location of pendine blocks, originally stacked two high in a U-shaped configuration around the vent hatch, post-test. The detached vent-hatch, partly obscured by the pendine blocks, is also visible on the ground.

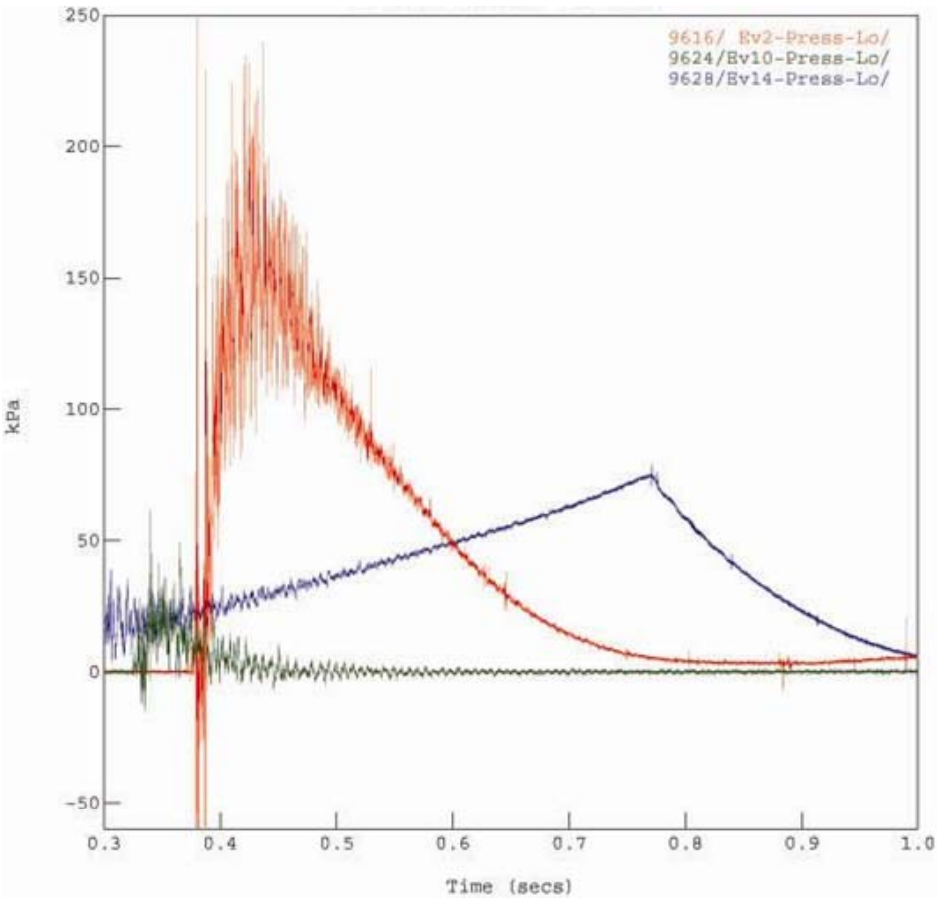

Figure 60: Crew compartment pressure-time profiles for the 3xBCM experiments as measured on the back of Person A. Experiment 2 had minimal room confinement but the propelling charge response was of a higher order than Experiment 10 (intermediate confinement) and Experiment 14 (high confinement).

Table 21: Intrathoracic overpressure effects from Experiment 2

Person	***A***		***B***		***C***	
Location	***CWV*(m/s)**	***ASII***	***CWV*(m/s)**	***ASII***	***CWV*(m/s)**	***ASII***
Front	3.7	0.29	2.5	0.10	1.9	0.06
Back	3.8	0.23	4.3	0.29	2.7	0.12
Right side	No Data		3.2	0.16	2.4	0.09
Left side	2.8	0.12	1.9	0.06	2.5	0.1

Burn damage to the skin is summarised in Table 22 and the level of burns sustained after 10 s exposure are likely to be fatal for all personnel in the crew compartment. With respect to the ambient temperature in the simulated crew compartment (see Figure 61), only the *T1* thermocouple survived the initial stages of the event. Based on the *T1* temperature-time curve the crew would have 0.6 s to escape before the 149°C respiratory threshold escape temperature is reached.

Table 22: Skin burn levels for Experiment 2

	Person A				Person B				Person C			
Exposure (s)	Groin	Chest	Back	Head	Groin	Chest	Back	Head	Groin	Chest	Back	Head
10	2	10	6	1,14	2	7	7	**No data**[a]	**No data**[b]	1	1	1,10
30	2	10	6	1,14	2	7	7			1,42	1,60	1,10

a,b	3rd degree burn, a=time to 2nd degree burn (s), b=time to 3rd degree burn (s)
a	2nd degree burn, a=time to 2nd degree burn (s)
a	1st degree burn, a=time to first degree burn (s)
-	No burn sustained

[a]Sensor delaminated at 1.2s

[b]Fragment strike

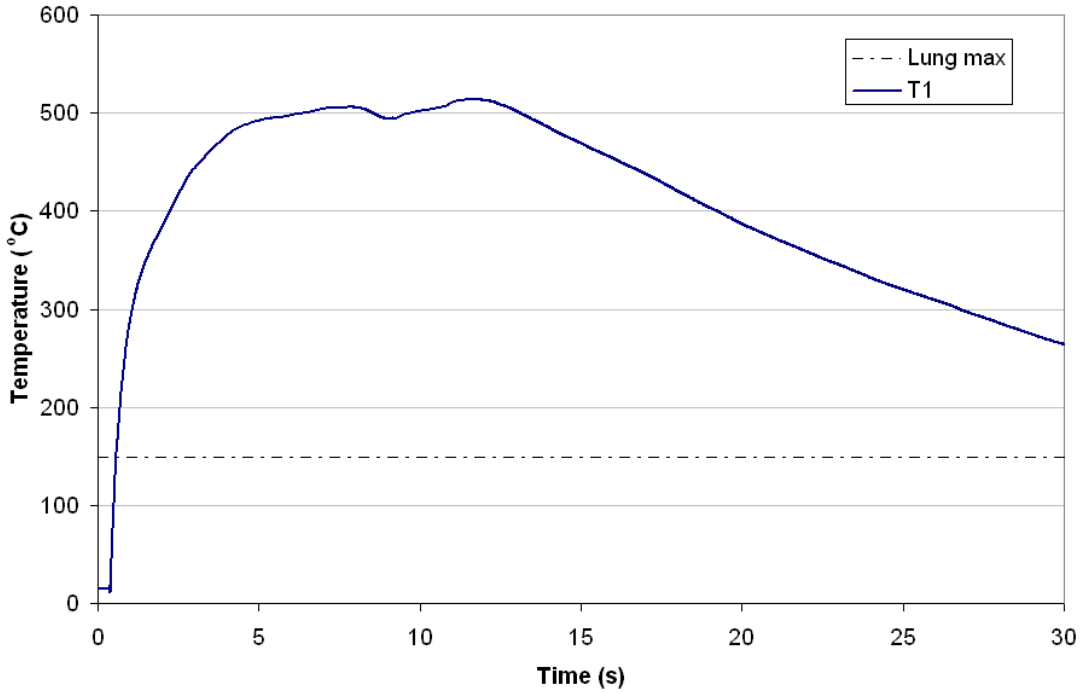

Figure 61: Temperature condition inside the simulated crew compartment for Experiment 2

Ejecta velocity data, presented in Figure 43, section 5.3.1, indicates that unburnt propellant grains travelling at potentially lethal velocities will be present inside the crew compartment.

6. Trial Limitations

During the design of the trial a number of assumptions needed to be made, due primarily to limitations in the availability of platform-specific information at the time the trial was developed. In certain instances the short time-frame available for preparation and conduct of this work program also necessitated modifications to known platform attributes for the sake of engineering design simplicity.

The major assumptions and modifications made are summarised below, along with a brief discussion of their implications to the conclusions made in this baseline study.

6.1 Simulated Crew Compartment

6.1.1 Orientation

Section 4.1.1 detailed the requirement to design the trials structure such that it represented the actual military vehicle lying on its side. For the baseline studies, propellant was ejected from

the storage tube at high velocity and in a widely dispersed fashion. As such, the influence of the trials structure orientation on the spatial heat release from propellant combustion would not be expected to be significant.

Similarly, as all items included in the simulated crew compartment were in the same relative positions as in the platform being represented and because clutter was not incorporated into the trials structure, the trials structure orientation should not have a significant influence on the ejecta and pressure environment resulting from the propelling charge event.

6.1.2 Absence of Clutter

The rationale for excluding clutter from the trials structure is provided in Section 4.1.1. The absence of clutter, and the increase in effective crew volume that occurs due to its absence, would likely have the following effect on sustained injuries:

- Reduced severity of injuries associated with the average thermal and pressure environment in the crew compartment.
- Increased likelihood of ejecta related injuries and direct flame impingement on the crew.
- The absence of clutter will alter the gas flow dynamics in the crew compartment, thus affecting the occurrence and magnitude of pressure reflections. This will influence potential overpressure-related injuries to personnel.
- The absence of clutter will create more favourable conditions for effective fire suppression, thus offering a potential reduction in thermal related injuries when an AFESS is used, see [22].

6.2 Simulated Personnel

A comparative assessment of the thermal protection afforded by the clothing configurations used in this trial, see [22], demonstrated the potential thermal protection benefits that could be gained through the judicious selection of clothing. As such, should different clothing configurations to that described in this trial be used, the energy absorption levels of the skin will be affected, thus potentially changing the reported skin burn damage predictions.

Clothing can also amplify pressure loading, with the level of amplification a function of the textile properties such as gas permeability and apparent bulk density [29,30]. Reference 29 shows an inverse relationship between peak pressure amplification and textile apparent bulk density for a range of different fabrics. In the cited reference, based on a shock loading test condition of 85 kPa overpressure with a positive phase duration of 5 ms, Nomex (apparent bulk density of 426 kg/m^3) gave a peak pressure amplification of approximately 2 and a cotton/nylon battle dress uniform fabric (apparent bulk density of 398 kg/m^3) gave a peak pressure amplification of approximately 2.8 [29]. Further, the strength of the shock front has a significant effect on the pressure wave amplification between different clothing configurations [30]. For example, data presented in [30] shows an average pressure amplification factor for a range of textile configurations of up to 2.5 when shock strength was increased from Mach 1.34 to Mach 1.42.

As the pressure sensors used in this trial were not covered by clothing, these amplification effects, if any, were not captured. However, the average pressure wave velocities for the most dynamic 3xBCM events in the trial, as estimated using the time from end-cap failure to the arrival of the first pressure wave at the pressure sensors nearest the storage tube, were approximately 230 m/s (corresponding to a Mach number at standard atmospheric conditions of 0.67). This is consistent with measured propellant grain ejecta velocities (see Figure 43) as well as with gas velocities predicted by modelling [31]. The sub-sonic flow regime of the pressure waves observed in this trial would be expected to limit the magnitude of any pressure amplification effects. This could be confirmed in subsequent trials by mounting the pressure sensors beneath the clothing.

Notwithstanding the above, to inform on the significance of excluding clothing effects on the pressure-induced damage to personnel, a pressure amplification factor of 3.0 was applied to the two pressure-time traces over the course of the trial that yielded the greatest intrathoracic overpressure damage. The results from this assessment are summarised in Table 23. Whilst application of the aforementioned amplification factor, which based on the cited literature would seem to be at the higher end of the probable spectrum, increases the level of sustained injury, in no cases does the enhanced injury level alter the conclusions made regarding likely crew survival.

Table 23: Effect of possible pressure amplification due to clothing on intrathoracic overpressure effects

	E2 Person B Back		**E10 Person C Chest**	
Amplification Factor	1.0	3.0	1.0	3.0
P_{max} (kPa)	381	1143	71	213
CWV_{max} (m/s)	4.3	7.4	1.9	5.0
ASII	0.29	0.99	0.06	0.40
Injury Level	Trace to slight	Slight to moderate	None	Slight to moderate

6.3 Propelling Charges

This trial investigated the prospects for crew survival in an unplanned initiation event involving the contents of only a single propelling charge storage tube in a platform where dozens of storage tubes and also HE-filled projectiles would typically be stored.

The results from the trial indicated that the sympathetic cook-off of other munitions inside the crew compartment would be a realistic possibility if a single propelling charge storage tube was initiated. If such a scenario were to occur, the reported prospects for crew and platform survivability would be greatly diminished.

There are a vast number of ways in which a propelling charge (or other energetic material) in the crew compartment could be initiated and the nature of the external stimuli that initiates the propelling charge can play a large role in governing the violence of the propelling charge

response. Consequently, the severity of the hazards that the crew are exposed to can be expected to vary in accordance with the manner in which the propelling charges are initiated. As the object of this study was to investigate the effect of a propelling charge event on crew survival, as opposed to investigating the effect of a range of external stimuli on propelling charge response, and also to aid in current modelling efforts [31], a reproducible, single point source method of initiation (pyrotechnic-filled silk bag) was selected.

The level of propelling charge confinement and the point of charge initiation will also affect the nature of the propelling charge response. An assessment of the effect of propelling charge confinement, as well as the effect of a different propelling charge initiation location on the thermal, ejecta and pressure environment created in an unplanned initiation event has been made in [22].

7. Conclusions

This work allowed the key threats posed to crew personnel, and the effectiveness of a range of hazard mitigation strategies (see [22]), in a propelling charge fire to be identified.

In a propelling charge initiation event involving a single storage tube inside the crew compartment the thermal and ejecta threats pose the greatest risk to crew survival.

In the absence of a fire suppression system, a propelling charge event in the crew compartment will create a thermal environment that will cause life-threatening respiratory and skin burn damage with a minimal probability of survival, irrespective of module configuration or ignition location. The sustained, high temperature environment will also pose a possible sympathetic cook-off risk to other munitions stored within the crew compartment.

Ejecta in the form of unburnt propellant grains and/or propelling charge modules pose a life threatening risk to crew for all baseline tests conducted. Ejecta damage to personnel may be reduced by weakening the storage tube end-cap seal. This is addressed in [22].

Whilst not life-threatening, the pressure environment associated with a single storage tube propelling charge event can cause non-life threatening injuries such as auditory damage and may also engender physiological responses that may impede egress of the crew, thus increasing the injury levels sustained.

Burn damage predictions from the transient heat flux measurements made over the course of this trial support heuristics proposed by the US Army Surgeon General for second degree burn damage using either 10 s energy absorption levels (160 kJ/m^2) or 10 s temperature-time integrals (1316°C.s). Results from this trial also indicate that a 10 s energy absorption level of 275 kJ/m^2 can be used as a heuristic for the onset of 3rd degree burns (see Appendix C).

8. Recommendations

If conducted, a second trial should focus on the more dynamic 3xBCM and also the 3xATC configurations in a trials structure that has an accurate representation of the clutter in the crew compartment. The inclusion of clutter, and its likely effect on the thermal, ejecta and pressure environment in the simulated crew compartment, would necessitate that follow-on trials be conducted with the crew compartment in its correct orientation.

The robustness of the copper disc sensors could be enhanced by using higher melting point solder to attach the thermocouple to the back of the disc and a higher temperature adhesive for attaching the copper discs to the instrumentation boards should be explored.

The deployment of a greater number of heat flux sensors would allow a more accurate prediction of burn damage as a function of skin surface area to be made. In turn, this would enable the probability of death resulting from skin burns to be determined.

Future trials should be conducted with the pressure sensors used for intrathoracic overpressure effect assessment mounted beneath the clothing so that any textile-related pressure amplification effects can be captured.

To enhance the turnaround time between experiments, the use of a frame to mount around the existing instrumentation boards should be considered as an alternative means of holding the clothing against the instrumentation boards, rather then tucking the clothing behind the board.

9. Acknowledgements

The authors are indebted to the following people and organisations, all of whom contributed greatly to the successful completion of this work program:

CAPT Mathew Brooks, JPEU Pt Wakefield, for facilitating the many non-routine activities conducted over the course of the trial and for his willingness to go above and beyond the call of duty to help ensure that maximum benefit was gained from the trial.

Mr Ian Argent, JPEU Pt Wakefield, for his excellent audio visual support, and preparedness to accommodate varying requirements as the trial progressed.

Mr Ken Pickett of Scientific and Engineering Services (SES) for his fantastic support in overseeing the trials stucture fabrication and other trials component design and manufacture in spite of the very short time frames available. Thanks are also extended to Mr Des Cass and Mr Federico Lorenzin, also of SES, for their support in many aspects of the trials preparation.

Mr Chris French and Ms Alicia Malter for undertaking the preliminary structural design and drafting of the trials superstructure.

Mr Gordon Proctor and Mr Michael Footner for instrumentation and data acquisition support and Mr Shaun McCormack for hi-speed camera support.

Dr Bin Lee of Land Division, DSTO and Mr Tino Pavic of Boeing Australia for discussions regarding thermal damage criterion and their experiences with heat flux measurement techniques during the early planning phases of the trial.

Dr Roger Li for performing the FEA analysis of the proposed crew compartment and storage tube end-caps.

Mr Raoul Pietrobon and Mr Michael Morgan of Explosives and Pyrotechnics Group, DSTO, for the provision of test materials and conduct of flare and igniter trials that were undertaken for the purposes of instrumentation development in the lead up to the trial.

Mr Alan Starks and Mr Roger Cockerill for undertaking the transportation of energetic materials and hardware throughout the course of the trial.

Mr Steve Kollias and Mr Tim Watts for their many useful discussions during the planning phases of the trial.

10. References

1. Johnston, I., (19 Nov 2009), Personal communication and unpublished modelling data, Weapons and Countermeasures Division, DSTO.

2 **SFPE Guide**, as cited in: Sipe, J.E., (2004), *Development of an Instrumented Dynamic Mannequin Test to Rate the Thermal Protection Provided by Protective Clothing*, M.Sc Thesis, Worcester Polytechnic Institute, pg.2.

3 **ISO 13506**, (2008), *Protective clothing against heat and flame – Test Methods for complete garments – Prediction of burn injury using an instrumented manikin*.

4 Gasperin, M., Juricic, D., Musizza, B., Mekjavuc, I., (2008), *A Model-Based approach to the Evaluation of Flame-Protective Garments*, **ISA Transactions**, 47, pp. 198-210.

5 Henriques, F.C., Jr., Moritz, A.R., (1947), *Studies of Thermal Injuries V. The Predictability and the Significance of Thermally Induced Rate Processes Leading to Irreversible Epidermal Injury*, **Archives of Pathology**, 43, pp. 489-502.

6 Stoll, A.M., Chianta, M.A., (1969), *Method and Rating System for Evaluation of Thermal Protection*, **Aerospace Medicine**, 40, pp. 1232-1238.

7 Takata, A.N., (1975), *Development of Criterion for Skin Burns*, **Aerospace Medicine**, 45, pp.634-637.

8 Pennes, H.H., (1948), *Analysis of Tissue and Arterial Blood Temperatures in Resting Human Forearm*, **Journal of Applied Physiology**, 1, pp. 93-122.

9 Torvi, D.A., Dale, J.D., (1994), *A Finite Element Model of Skin Subjected to a Flash Fire*, **Journal of Biomechanical Engineering**, 116, pp. 250-255.

10 Torvi, D.A., Hadjisophocleous, G.V., Hum, J., (2000), *A New Method of Estimating the Effects of Thermal Radiation from Fires on Building Occupants*, **Proceedings of the ASME Heat Transfer Division**, pp. 65-72.

11 McCormick, S., Clauson, M., (2006), *Halon Replacment Program (HRP) for US Army Ground Combat Vehicles*, **TACOM TARDEC Report Number 15837 RC**.

12 Hymes, I., Brearly, S., Prescott, B.L., Zahid, M., (1993), *The Prognosis of Burn Injury Victims*, **SRD/HSE Report R600**, Safety and Reliability Directorate, Chesire, U.K. As cited in reference **10**.

13 Pryor, A.J., (1968), *Full-Scale Evaluation of the Fire Hazard of Interior Wall Finishes*, Southwest Research Institute, San Antonio. As cited in Bryan, J.L., (1986), **Fire Safety Journal**, 11, pp. 15-31.

14 Spieth, H.H., Gaume, J.G., Luoto, R.E., Klinck, D.M., (1982), *A Combined Hazard Index Fire Test Methodology for Aircraft Cabin Materials*, Vols. I and II, **DOT/FAA/CT-82/36-1** and **DOT/FAA/CT-82/36-11**, Department of Transportation, Atlantic City. As cited in Bryan, J.L., (1986), **Fire Safety Journal**, 11, pp. 15-31.

15 Axelsson, H., Yelverton, J.T., (1996), *Chest Wall Velocity as a Predictor of Nonauditory Blast Injury in a Complex Wave Environment*, **The Journal of Trauma: Injury, Infection and Critical Care**, 40(3), pp. S31-S37.

16 NATO Report: RTO-TR-HFM-090, *Test Methodology for Protection of Vehicle Occupants against Anti-Vehicular Landmine Effects*, April 2007, Chapter 3-4.

17 Yelverton, J.T, (1993), *Blast Overpressure Studies with Animals and Man: Final report – Biological Response to Complex Blast Waves*. US Army Medical Research and Development Command, Fort Detrick. As cited in reference 15.

18 Yelverton, J.T, (1994), *Pathology Scoring System for Blast Injuries*, **Proceedings of the 7th International Symposium of Weapons Traumatology and Wound Ballistics**, St Petersburg, Russia.

19 Richmond, D.R. *et al*, (1989), *Physical Correlates of Eardrum Rupture*, **Annals of Otology, Rhinology and Laryngology**, 98, pp.35-41

20 Clare, V.R. et al, (1975), *Blunt Trauma Data Correlation*, **Edgewood Arsenal report AD-A012 761**, Figure 7, pg 21.

21 Duma, S.M. *et al*, (2005), *Determination of Significant Parameters for Eye Injury Risk from Projectiles*, **Journal of Trauma: Injury, Infection and Critical Care**, 59(4), pp. 960-964.

22 Hart, A.H., Lade, B., Hale, G., (2013), *Survivability of a Propellant Fire Inside a Simulated Military Vehicle Crew Compartment. Part 2: Hazard Mitigation Measures*, **DSTO-RR-0393**, Weapons and Countermeasures Division – DSTO Edinburgh.

23 Henschke, P., (March 2010), Personal communication, Weapons and Countermeasures Division, DSTO.

24 Li, R., (15 April 2010), Personal communication and unpublished modelling data, Weapons and Countermeasures Division, DSTO.

25 Stoll, A.M., Greene, L.C., (1959), **Journal of Applied Physiology**, 14, pp.373-382. As cited in Torvi, D.A., Dale, J.D., (1994), *A Finite Element Model of Skin Subjected to a Flash Fire*, **Journal of Biomechanical Engineering**, 116, pp.250-255.

26 Cassidy, K., (25 March 2010), Personal communication, Combat Clothing Sustainment Technical Manager, Defence Materiel Organisation.

27 van Deursen, J.R., van der Horst, M.J., van de Kasteele, R.M. and Weerheijm, J., (2006), *Injury Assessment for Blast Overpressure Effects: Experimental Approach*, **19th Symposium of Military Aspects of Blast and Shock**, Calgary, Canada.

28 Li, R., Hart, A., (2010), unpublished data, Weapons and Countermeasures Division, DSTO.

29 Gibson, P.W., (1995), *Amplification of Air Shock Waves by Textile Materials*, **J. Textile Inst**, 86(1), pp. 119-128.

30 Skews, B.W., Bugarin, S., *Blast Pressure Amplification due to Textile Coverings*, **Textile Research Journal**, 76(4), pp. 328-335.

31 Harrland, A., Johnston, I., Hart, A., (2013), Simulation of a Propelling Charge Fire in an Armoured Combat Vehicle, DSTO Technical Report, Weapons Systems Division, DSTO, in preparation.

32 Holman, J.P., **Heat Transfer**, 8th Edn, 1999, McGraw-Hill, Chapters 7-8.

33 Protective Clothing Against Heat and Flame – Determination of Heat Transmission on Exposure to Flame, **ISO 9151:1995(E)**.

34 Lee, B., Pavic, T.*, (16 Feb 2010), Personal communication, Land Division, DSTO and *Boeing Australia.

Appendix A: Test Condition Summary

Table 24: Crew compartment environmental conditions

Experiment	Date	$T_{ambient}$ (°C)	*RH* (%)
1	23/6/10	17	61
2	24/6/10	10.5	81
3	25/6/10	14.5	72
4	29/6/10	9	93
5	29/6/10	14	78
6	30/6/10	14	78
7	1/7/10	17	52
8	2/7/10	19.5	67
9	5/7/10	16	46
10	6/7/10	12	76
11	6/7/10	18.5	50
12	6/7/10	17	52
13	7/7/10	18	53
14	8/7/10	18	45
15	8/7/10	19.5	44

Appendix B: Heat Flux Measurement Techniques

Consider first the measurement of heat flux using the copper discs mounted to the instrumentation boards. A simple energy balance taken over the control volume depicted in Figure 62 is required to relate the measured temperature-time profile of the copper disc to the rate of energy absorption by the skin.

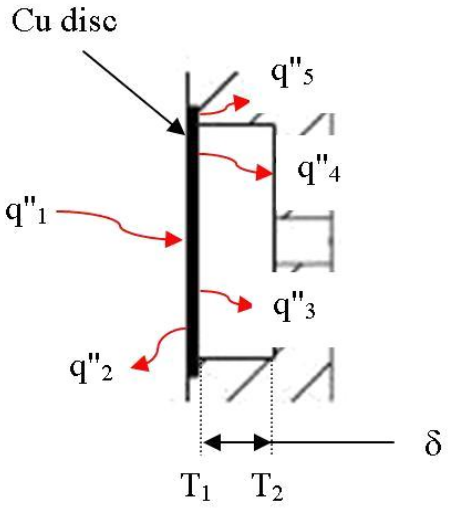

q″$_1$=incident heat flux
q″$_2$=heat flux losses to atmosphere
q″$_3$=heat flux conduction and convection losses to air gap between disc and board
q″$_4$= heat flux radiation losses from back of disc
q″$_5$=heat flux losses via conduction from edges of disc in contact with board

Figure 62: Energy balance over the copper disc and instrumentation board

If it is assumed that q''_2 will be common to both the copper disc and to the skin, as both will be exposed to the same environment and because the copper discs are prepared so as to have comparable surface emissivity to that of skin, then the heat flux absorbed by the skin can be represented by equation (12).

$$q''_{absorbed} = q''_{stored} + q''_{losses} = \left(q''_1 - q''_2\right) + \left(q''_3 + q''_4 + q''_5\right) \tag{12}$$

The energy stored by the copper disc can be determined by applying a lumped heat capacity analysis to the measured temperature-time profile of the disc:

$$q''_1 - q''_2 = \left(\frac{mC_p}{A}\frac{dT}{dt}\right)_{disc} \tag{13}$$

To assess the magnitude of the energy losses on the calculated heat flux profiles, a condition that would maximise the energy losses from the copper disc was considered. Energy loss calculations were performed using a copper disc temperature of 190°C (corresponding to sensor assembly failure) and an ambient temperature in the air gap behind the copper disc and the instrumentation board of 15°C.

Conduction and Convection Losses, q''_3+q''_5

Conduction losses from the copper disc will occur to the air in the air gap between the back of the disc and the instrumentation board, as well as from the surface of the copper disc that is in contact with the instrumentation board. Thermal conduction contact losses, q''_5, have not been considered in this simple analysis as their calculation requires knowledge of the transient temperature profiles of the instrumentation board in the vicinity of the copper disc, which is not known. Further, the low thermal diffusivity of the instrumentation board relative to the copper disc, coupled with the very small contact area between the two ought to minimise these losses over the time intervals of interest.

Convection losses from the copper disc to the air gap behind the copper disc are representative of a natural convection phenomenon in an enclosed space. As convection is an orientation dependant phenomenon, three cases need to be considered for the instrumentation boards used in the trial, as detailed below. Irrespective of orientation, the heat flux losses owing to natural convection and conduction from the back of the copper disc is given by equation (14) [32]:

$$q''_3 = Nu_\delta \frac{k}{\delta}\left(T_1 - T_2\right) \tag{14}$$

Where the geometry-dependent Nusselt number, *Nu*, is a function of the dimensionless Grashof , *Gr*, and Prandtl, *Pr*, numbers as shown in equation (16).

$$\begin{aligned} Gr_\delta &= \frac{\rho^2 g\left(T_1 - T_2\right)\delta^3}{T_f \mu^2} \\ \Pr &= \frac{C_p \mu}{k} \end{aligned} \tag{15}$$

In equation (15), all air properties are evaluated at the film temperature, T_f.

$$Nu_\delta = C\left(Gr_\delta \Pr\right)^n \left(\frac{L}{\delta}\right)^m \tag{16}$$

In equation (16), *C*, *n* and *m* are empirically determined constants.

Using the assumed condition of T_1=190°C and T_2=15°C the following air properties are obtained at the T_f of 102.5°C:

ρ =0.94 kg/m^3
C_p=1010 J/kg.K
μ=2.2x10^{-5} kg/m.s
k=0.032 W/m°C

From the instrumentation board design, the air gap thickness, δ, is 10.2 mm and the length of the surface over which convection was occurring, L, was taken as the 35 mm diameter of the copper disc.

Case 1: Horizontal surface, $T_{disc\ upper\ face} > T_{disc\ lower\ face}$

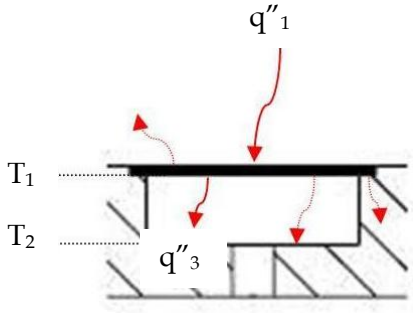

Case 1 is applicable to the copper discs mounted on the back of Person A and C. In this configuration, as the air in the air gap immediately below the copper disc will be hotter, and therefore less dense, than the air at the bottom of the air gap, there will be minimal convection currents and therefore negligible natural convection. Hence, in this case, Nu=1 and heat transfer is by pure conduction.

$$q''_3 = \frac{k}{\delta}(T_1 - T_2) = 550 W/m^2$$

Case 2: Horizontal Surface, $T_{disc\ upper\ face} < T_{disc\ lower\ face}$

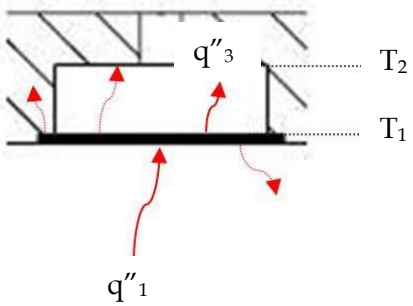

Case 2 is applicable to the copper discs mounted on the groin, chest and head of Person A and Person C.

The *GrPr* for this configuration is 6000, well above the 1700 threshold at which natural convection begins to occur on horizontal surfaces.

Given the horizontal orientation, *L* has no influence on the natural convection heat transfer coefficient and *m* in equation (16) is zero. Values for the empirical constants *C* and *n* for this case and under these assumed temperature conditions are 0.059 and 0.4 respectively [32].

Substituting these values into equations (14) and (16) gives heat flux losses of 1050 W/m^2.

Case 3: Vertical Surface

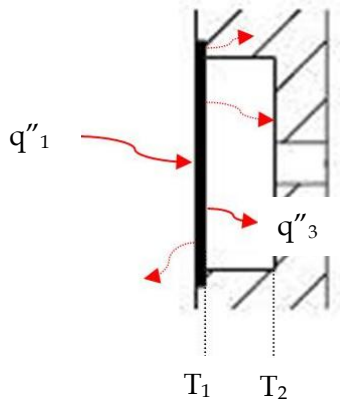

Case 3 is applicable to the copper discs mounted on Person B.

For *GrPr*=6000, for an isothermal vertical plate, *C*, *n* and *m* are 0.197, 0.25 and -0.11 respectively [32].

Substituting these values into equations (14) and (16) gives heat flux losses of 830 W/m^2.

Radiation losses, q″$_4$

Radiation losses from the back of the copper disc to the instrumentation board can be estimated assuming radiation heat transfer between parallel discs separated by a 10.2 mm air gap.

$$q"_4 = F_{1-2}\varepsilon\sigma\left(T_1^4 - T_2^4\right) \qquad (17)$$

For 35 mm diameter plates with a 10.2 mm air gap, the radiation shape factor, $F_{1\text{-}2}$, is approximately 0.58 [32]. However, the physical interpretation of this is that 58% of the energy in the form of radiation that is leaving surface 1 (the back of the copper disc) is absorbed by

surface 2 (the instrumentation board). Whilst this is important if wishing to calculate the temperature increase of surface 2, we are only interested in the losses from the copper disc. Hence, F_{1-2} was taken to be equal to 1 for the calculation of radiation heat flux losses.

Using the assumed condition of T_1=190°C and T_2=15°C, the radiation heat flux losses are calculated to be 2100 W/m².

The above calculations were repeated at a number of other typically observed copper disc temperatures to see how the magnitude of the losses varied. This is summarised in Table 25.

Table 25: Estimation of copper disc heat flux losses

Copper disc T (°C)	Heat Flux losses (W/m²)		
	q''_3	q''_4	Total
50	90-140	230	320-370
100	235-440	710	945-1150
190	830-1050	2100	2930-3150

As the instantaneous heat flux is a function of the rate of change of temperature, rather than the absolute temperature at any point in time, it is difficult to relate a given copper disc temperature to a heat flux. Despite this, a cursory inspection of the data where the maximum temperature of the copper disc at the end of the initial disc temperature rise approached the temperatures stated above was used to approximate typically observed heat flux levels for these cases, see Table 26.

Table 26: Comparison of heat flux losses to measured heat fluxes

Copper disc T (°C)	Measured Heat flux (kW/m²)	Heat flux losses (kW/m²)	% losses
50	18	0.37	2.1
100	75	1.15	1.5
190	180	3.15	1.8

The data in Table 26 suggests that the heat flux losses represent approximately 2% of the measured heat flux, thus supporting the assumption that neglecting copper disc heat flux losses will not have a large effect on the calculated transient heat flux profiles, and will have a minimal effect on the predicted burn levels.

Using this assumption, for the purposes of calculating instantaneous heat flux from copper disc temperature-time profiles, equation (12) can be simplified to:

$$q''_{absorbed} \approx q''_{stored} = \left(\frac{mC_p}{A} \frac{dT}{dt} \right)_{disc} \tag{18}$$

The mass of the 1.2 mm and 1.6 mm thick copper discs was 10.2 and 13.7 g respectively. The C_p of the copper was assumed to be 0.385 kJ/kg°C, as provided in ISO Standard 9151 for copper with a purity >99% [33].

The raw temperature data was sampled at 100 Hz and then filtered at 10 Hz. Because of the need to use the temperature-time derivative to calculate the heat flux, and the fluctuations that the derivative introduces into the calculated values, a 40 point running average (representing 0.4 s) of filtered *T-t* data was taken prior to calculating the derivative. A five-point least linear squares method (see equation (19)) was then used to evaluate the temperature-time derivative as it gave the best compromise between smoothing of the resultant heat flux profiles without losing any features of the temperature-time profiles.

$$\left.\frac{dT}{dt}\right|_{t_m} = \frac{-2T_{m-2} - T_{m-1} + T_{m+1} + 2T_{m+2}}{2.5\left(t_{m+2} - t_{m-2}\right)} \tag{19}$$

Figure 63 shows the conversion of the raw copper disc temperature-time data to a heat flux profile as measured at the head of Person A in Experiment 1.

The use of the Omega HS-4 gauges eliminates the need to go through the above data reduction procedure, as the output of the sensors can be converted directly to a heat flux using the manufacturer supplied calibration data that is applicable for the gauges with a surface emissivity approaching unity [34]. As the low profile HS-4 gauges, with a nominal thickness of 0.18 mm, are mounted flat on the instrumentation boards that have a thermal diffusivity and a thermal effusivity similar to that of human skin, the gauge setup is already representative of heat absorption by the skin without the need to correct for energy losses.

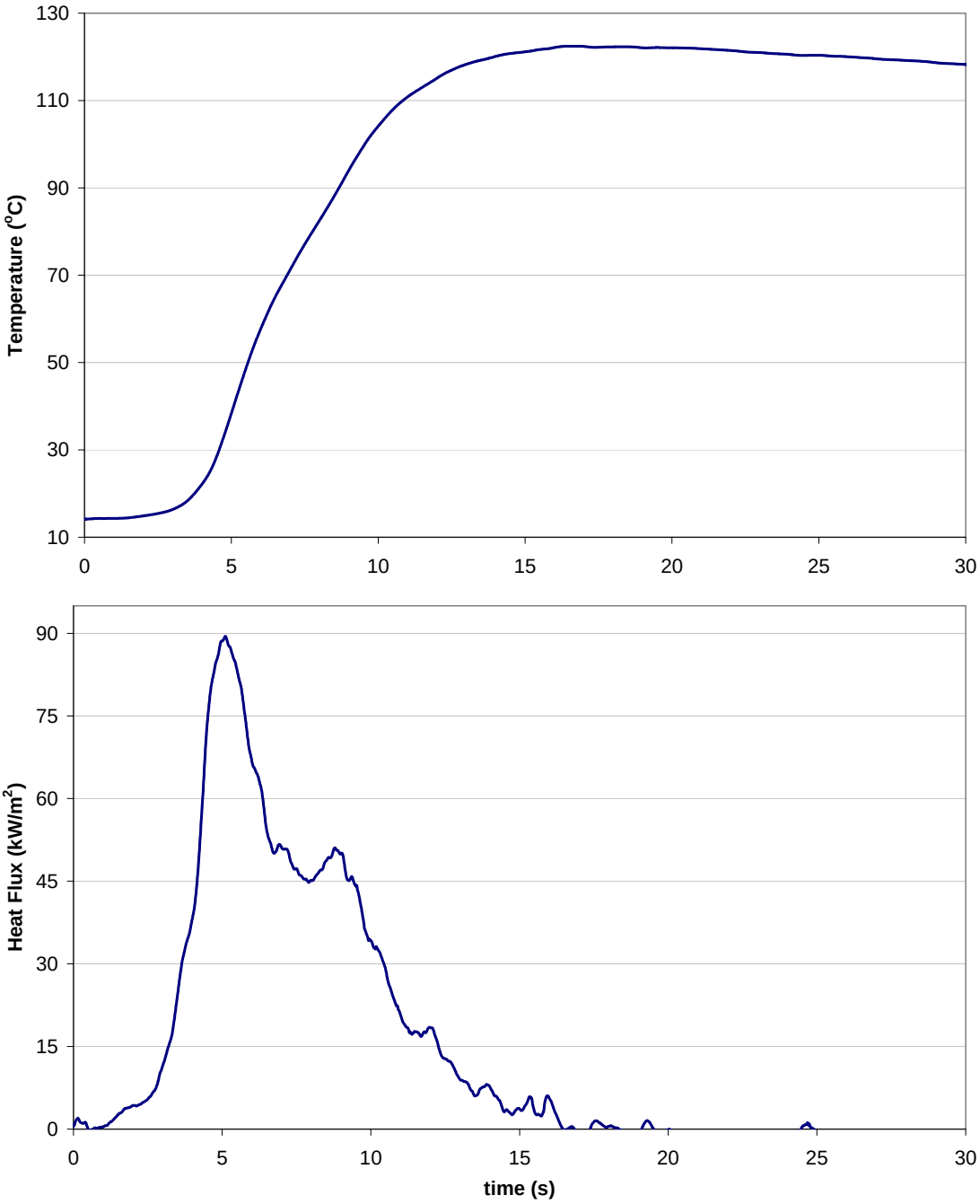

Figure 63: Example of the translation of a copper disc temperature-time profile to a heat flux profile. Measured data for Person A Head, Experiment 1.

A comparison between heat flux data measured using copper discs and the Omega HS-4 gauges in the trial are provided in Figure 64 to Figure 66. Due to limitations with the number of data acquisition channels, comparative data was only obtained until it was apparent that the two sensor types gave acceptable agreement. After this point, copper discs were positioned in locations where the heat flux levels were highest and the most sustained (typically the head and groin positions). The less robust Omega HS-4 gauges were mounted in positions where a less severe thermal environment was encountered (typically the chest and back).

Compared with the Omega HS-4 sensors, the heat flux profiles determined from the copper discs are more sensitive to electrical noise. Reasons include:

- The calculation of the heat flux for the copper disc measurement methodology requires the differentiation of the disc temperature-time profile.
- The electrical output from the single thermocouple attached to the copper disc requires the application of a higher gain factor when compared with the output from the 50 thermocouple junctions in the Omega HS-4 thermopile.

Possible sources of induced electrical noise in the conducted experiments include: the triboelectric effect in the coaxial cable used with the Omega sensors and copper disc thermocouples; and static electricity associated with high velocity gases as they exit the storage tube. These effects are most significant at the time of end-cap failure, and will be more significant for the more dynamic events where gas velocities and pressure waves are higher, see for example Figure 66.

Figure 64 to Figure 66 shows that the copper discs and Omega HS-4 gauges give acceptable agreement in terms of both heat flux profile and magnitude. The heat flux curves from both sensor types gave near-identical results with respect to skin burn damage assessment.

The copper discs, owing to their thermal mass, have a slower response time than the Omega HS-4 sensors and are also less sensitive to minor variations in heat flux. However, the copper discs are a cheaper, more robust sensor. For sustained, high heat flux events such as those observed over the course of this trial, copper discs are the preferred sensor option. For future work of this kind, the robustness of the copper discs could be further enhanced by using higher melting point solder to attach the thermocouple to the back of the disc, and by using a higher temperature alternative to hot melt glue to attach the copper discs to the instrumentation boards.

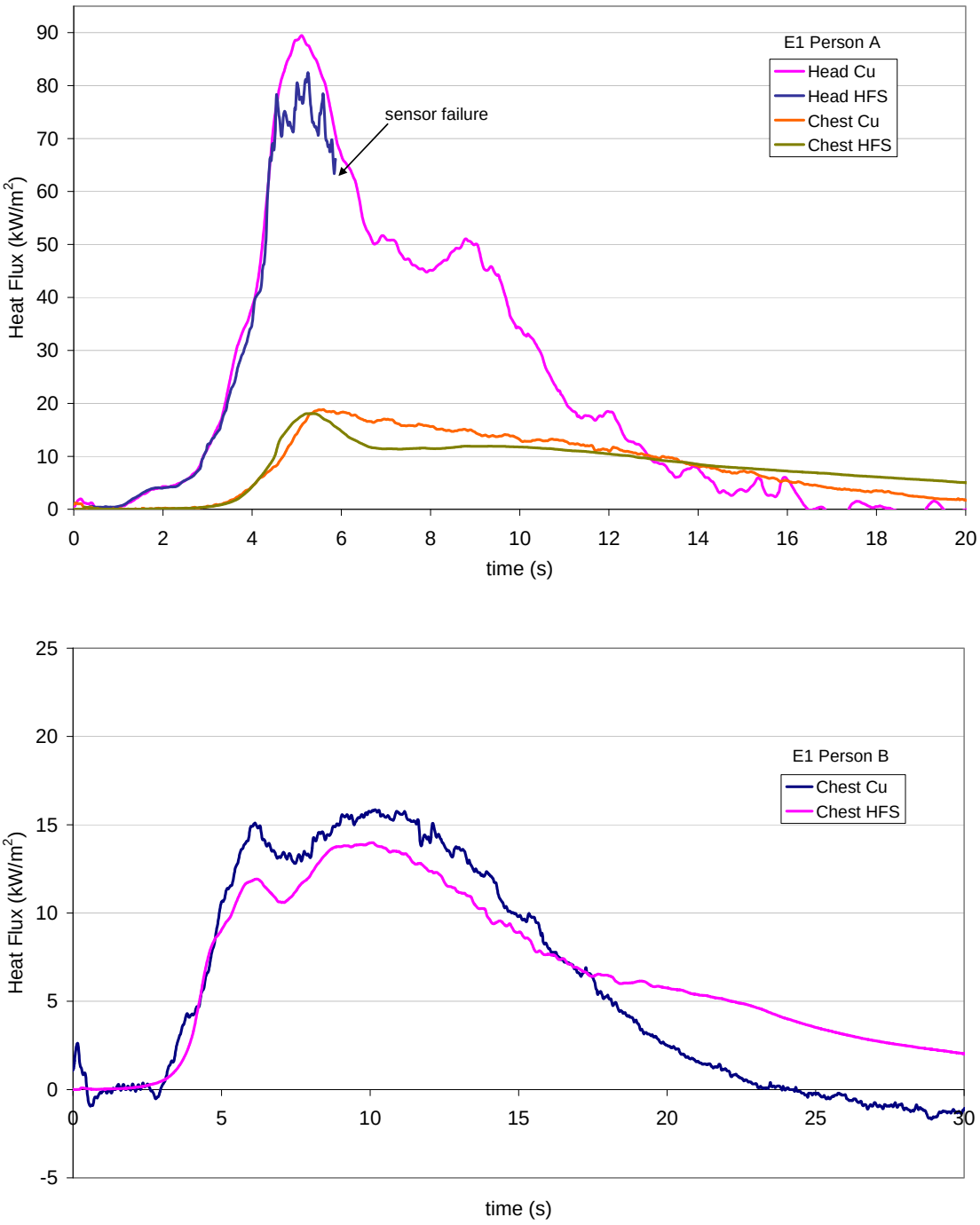

Figure 64: Omega HS-4 (HFS) and copper disc (Cu) heat flux measurement comparison for Experiment 1

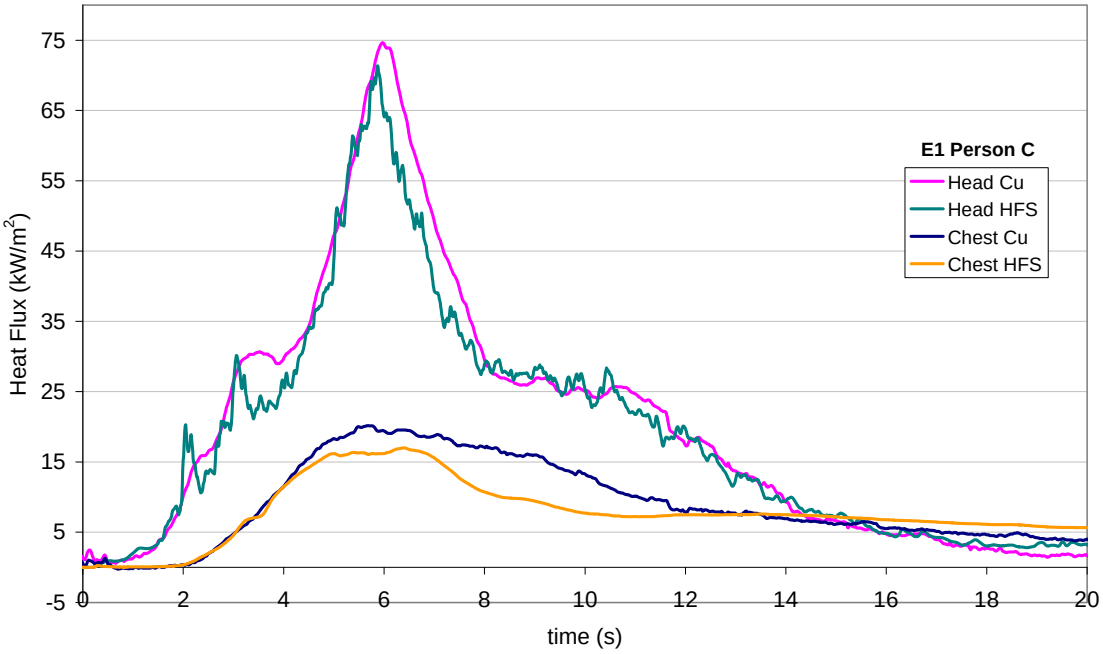

Figure 64: Omega HS-4 (HFS) and copper disc (Cu) heat flux measurement comparison for Experiment 1, (cont.)

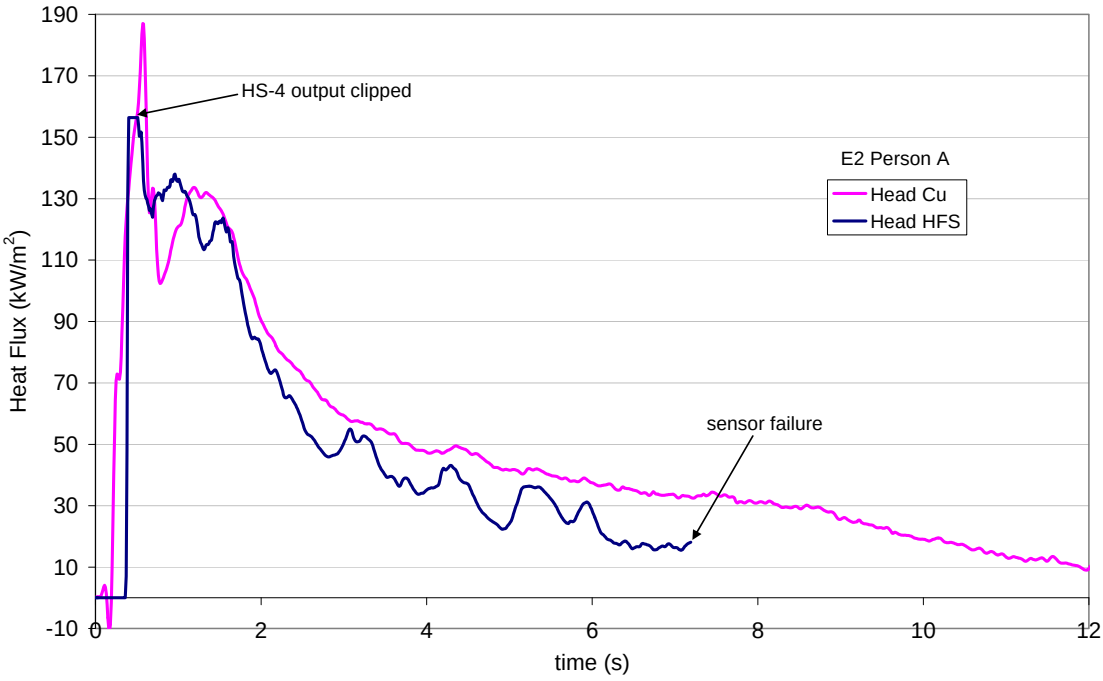

Figure 65: Omega HS-4 (HFS) and copper disc (Cu) heat flux measurement comparison for Experiment 2

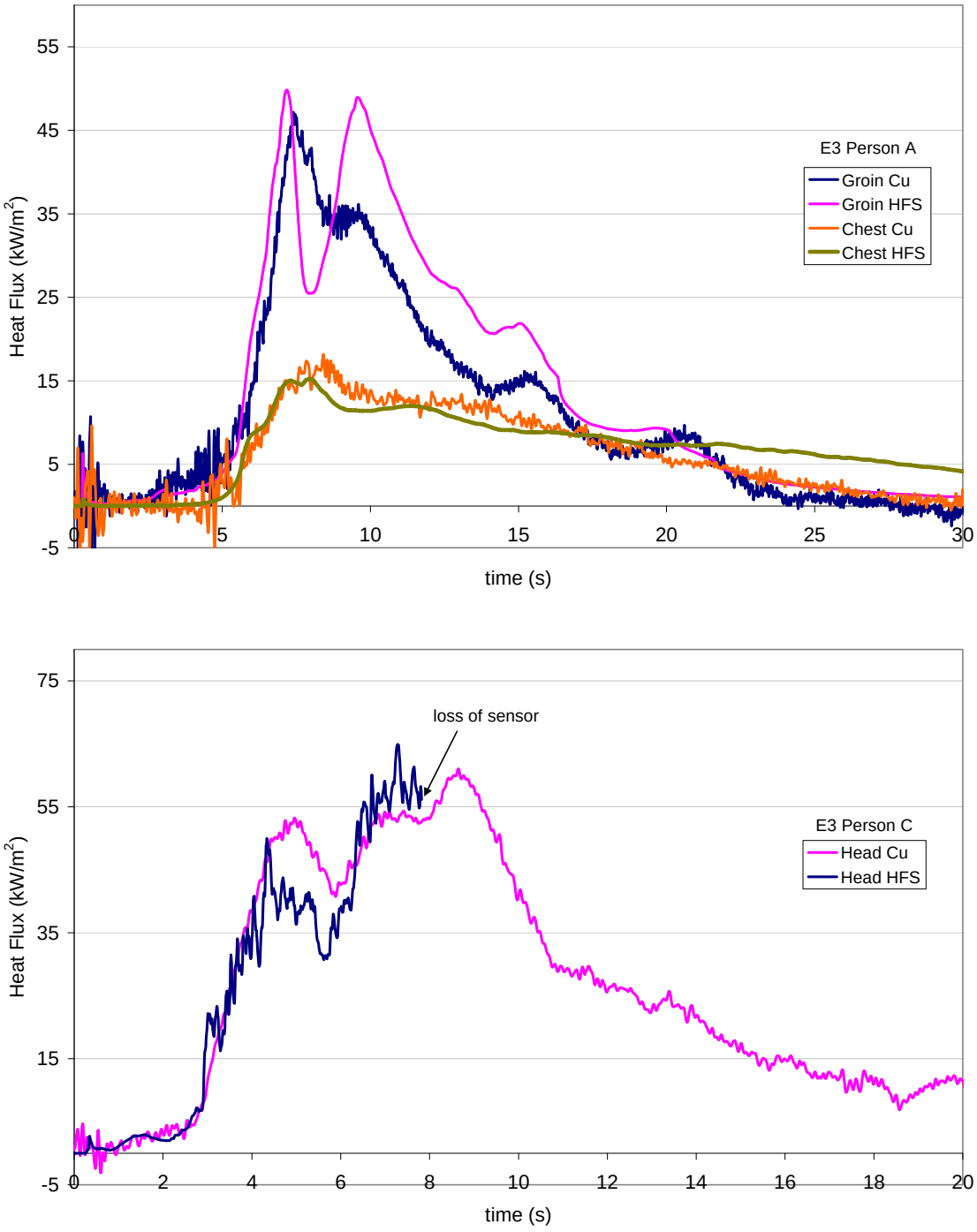

Figure 66: Omega HS-4 (HFS) and copper disc (Cu) heat flux measurement comparison for Experiment 3

Appendix C: Alternative Thermal Criteria

Section 3.1 lists heuristics, proposed by the US Army Surgeon General, for predicting 2nd degree burns, quoting a 10 s energy absorption level of 160 kJ/m². Figure 67 summarises sustained burn levels as a function of 10 s energy absorption for the experiments conducted in the trial. The presented data indicates the onset of 2nd and 3rd degree burns at 10 s energy absorption levels of 70 and 275 kJ/m² respectively, with these thresholds being depicted on the graph with horizontal dashed lines. The quoted 160 kJ/m² lies in the middle of the 2nd degree burn level energy absorption range and so can be considered a useful 2nd degree burn prediction tool providing that data is available to quantify the level of energy absorbed. In the absence of any other data, Figure 67 indicates that a 10 s energy absorption level of 275 kJ/m² could be used as a threshold value for the onset of 3rd degree burns.

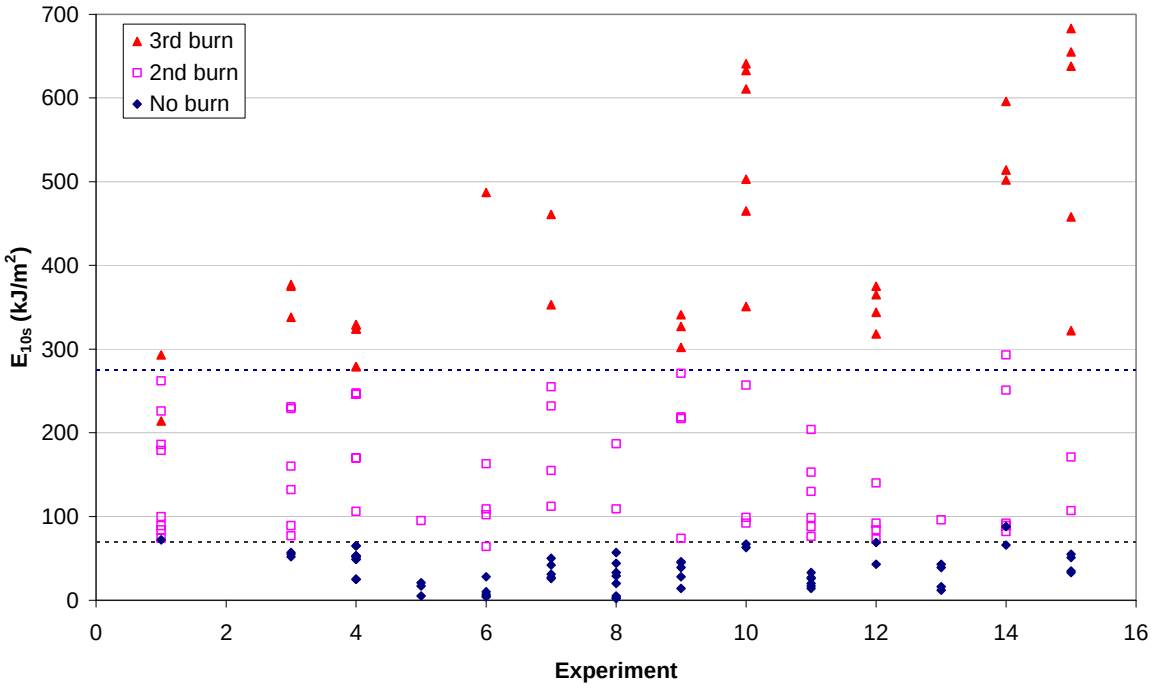

Figure 67: 10 s energy absorption levels for 2nd and 3rd degree burns

A comparison between the time to 2nd degree burns as determined using the developed burn prediction model, with the time for 2nd degree burns based on a *T-t* integral of 1316°C.s over a maximum 10 s period, as quoted by the US Army Surgeon General, is provided in Figure 68. The *T-t* integral was evaluated using the average of *T1* and *T2*. In the figure, the burn model average was taken as the average time for the onset of 2nd degree burns for all body positions where heat flux measurements were made. In instances where a sensor was damaged prior to 10 s and before 2nd degree burns were sustained, it was necessary to assume a 2nd degree burn time. This was done by comparison with other analogous experiments conducted in the trial and by considering the heat flux profiles at other body positions in the experiment in question. Where such assumptions are made, a degree of error is introduced into the average

time to 2nd degree burns. Notwithstanding this, Figure 68 displays reasonable agreement for the majority of experiments where the 1316°C.s *T-t* integral was reached in the first 10 s of the event.

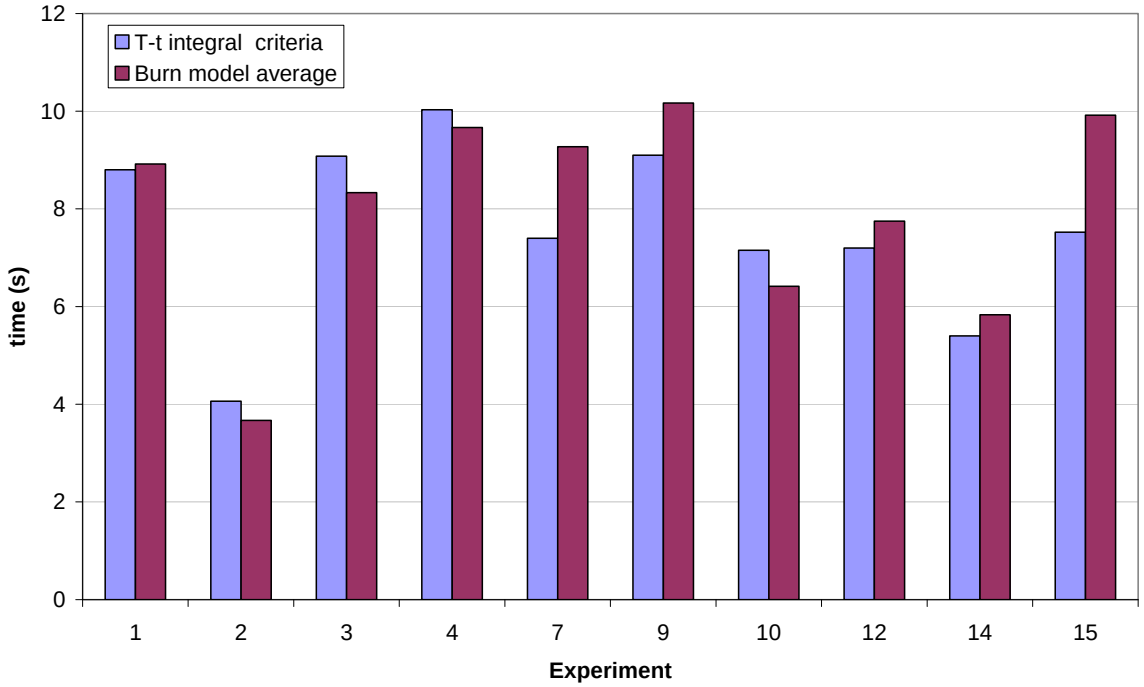

Figure 68: Comparison between T-t integral 2nd degree burn predictions and the burn prediction model based on the experimental data from the trial

For the experiments where a comparative assessment was possible, the difference between the 2nd degree burn time as calculated from the burn model, compared with the time based on the *T-t* integral is summarised in Figure 69. The average standard deviation for the residuals presented in the figure is 0.6 s. As for the case with the 10 s energy absorption heuristics, the *T-t* integral heuristics appear to be a reasonable tool to use for a cursory assessment of 2nd degree burn damage, providing the burn occurs within the first 10 s of the event.

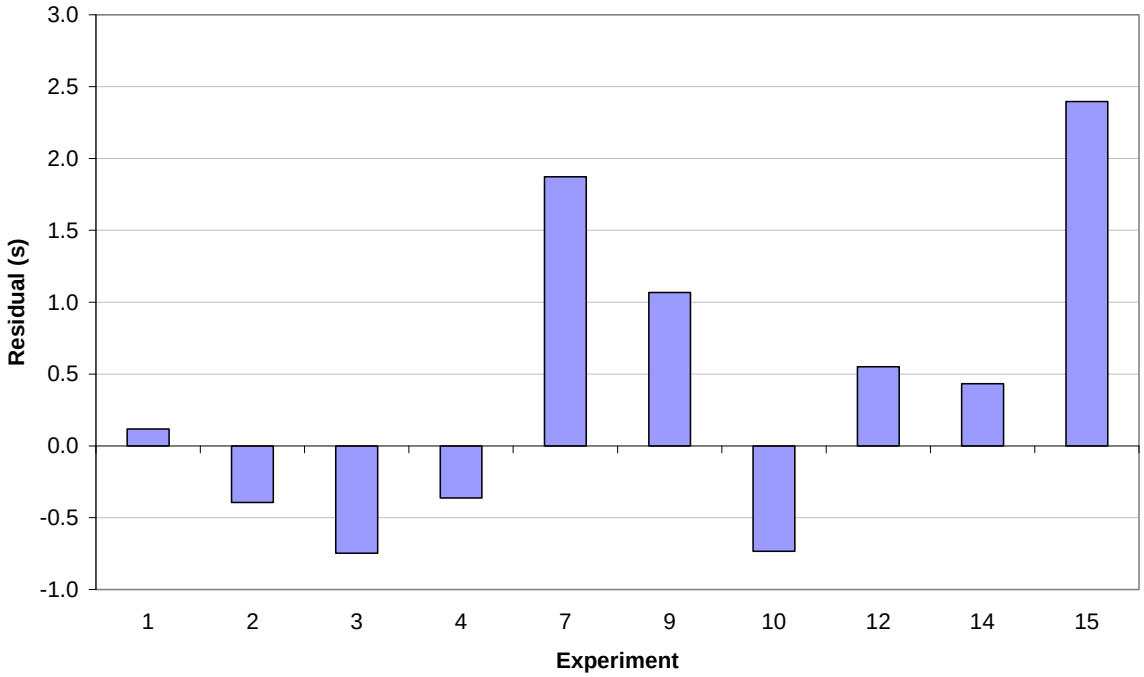

Figure 69: Difference between the burn model 2nd degree burn prediction and the T-t integral 2nd degree burn heuristics by experiment

Appendix D: Intrathoracic Overpressure Model Solution

Appendix D summarises the solution technique used to solve the non-linear second-order ordinary differential equation (ODE) developed by Axelsson and Yelverton to determine the effects of intrathoracic overpressure on CWV, see section 3.2. As an exact solution does not exist for equation (9), a numerical method must be used to solve the equation. For this work, the improved Euler method was used.

$$M\frac{d^2x}{dt^2}+J\frac{dx}{dt}+Kx=A\left[P(t)+P_o-P_o\left(\frac{V}{V-Ax}\right)^{\gamma}\right] \tag{9}$$

Denote $\frac{d^2x}{dt^2}$ and $\frac{dx}{dt}$ as x'' and x' respectively.

Convert equation (9) into two first order ODE's by defining a new variable, y.

$$y=x' \tag{20}$$

Substituting equation (18) into equation (9) and rearranging in terms of y' gives:

$$y'=\frac{A}{M}\left[P(t)+P_o-P_o\left(\frac{V}{V-Ax}\right)^{\gamma}\right]-\frac{J}{M}y-\frac{K}{M}x \tag{21}$$

Using the initial values at t=0 of $P(t)=x=x'=y=y'=0$, equations (20) and (21) are solved for each time step, i. In equations (22) to (24), subscript p refers to predictor values and subscript c refers to corrected values. The step-size between calculations is denoted as h.

Predictor values:

$$y_{p,i+1}=y_{c,i}+h\left\{\frac{A}{M}\left[P(t_i)+P_o-P_o\left(\frac{V}{V-Ax_{c,i}}\right)^{\gamma}\right]-\frac{J}{M}y_{c,i}-\frac{K}{M}x_{c,i}\right\} \tag{22}$$

Corrected values:

$$x_{c,i+1}=x_{c,i}+\frac{h}{2}\left(y_{c,i}+y_{p,i+1}\right) \tag{23}$$

$$y_{c,i+1} = y_{c,i} + \frac{h}{2}\left\{\beta + \frac{A}{M}\left[P\left(t_{i+1}\right) + P_o - P_o\left(\frac{V}{V - Ax_{c,i+1}}\right)^{\gamma}\right] - \frac{J}{M}y_{p,i+1} - \frac{K}{M}x_{c,i+1}\right\} \quad (24)$$

Where, in equation (24):

$$\beta = \frac{A}{M}\left[P\left(t_i\right) + P_o - P_o\left(\frac{V}{V - Ax_{c,i}}\right)^{\gamma}\right] - \frac{J}{M}y_{c,i} - \frac{K}{M}x_{c,i}$$

The solution for $y_{c,i+1}$ gives the *CWV* at the corresponding time step, *i+1*. The maximum calculated chest velocity (CWV_{max}) is then used in equation (8), repeated below, to predict the sustained intrathoracic injury level.

$$ASII = \left(0.124 + 0.117CWV_{\max}\right)^{2.63} \quad (8)$$

The values for the constants in these equations are provided in Table 3, section 3.2.

DEFENCE SCIENCE AND TECHNOLOGY ORGANISATION
DOCUMENT CONTROL DATA

1. PRIVACY MARKING/CAVEAT (OF DOCUMENT)

2. TITLE

Survivability of a Propellant Fire inside a Simulated Military Vehicle Crew Compartment: Part 1 - Baseline Study

3. SECURITY CLASSIFICATION (FOR UNCLASSIFIED REPORTS THAT ARE LIMITED RELEASE USE (L) NEXT TO DOCUMENT CLASSIFICATION)

Document	(U)
Title	(U)
Abstract	(U)

4. AUTHOR(S)

Andrew H. Hart, Blair Lade and Garry Hale

5. CORPORATE AUTHOR

DSTO Defence Science and Technology Organisation
PO Box 1500
Edinburgh South Australia 5111 Australia

6a. DSTO NUMBER	6b. AR NUMBER	6c. TYPE OF REPORT	7. DOCUMENT DATE
DSTO-RR-0392	AR-015-620	Research Report	June 2013

8. FILE NUMBER	9. TASK NUMBER	10. TASK SPONSOR	11. NO. OF PAGES	12. NO. OF REFERENCES
2012/1016112/1	CDG 09/0007	CDG	111	34

13. DSTO Publications Repository

http://dspace.dsto.defence.gov.au/dspace/

14. RELEASE AUTHORITY

Chief, Weapons and Countermeasures Division

15. SECONDARY RELEASE STATEMENT OF THIS DOCUMENT

Approved for public release

OVERSEAS ENQUIRIES OUTSIDE STATED LIMITATIONS SHOULD BE REFERRED THROUGH DOCUMENT EXCHANGE, PO BOX 1500, EDINBURGH, SA 5111

16. DELIBERATE ANNOUNCEMENT

No Limitations

17. CITATION IN OTHER DOCUMENTS Yes

18. DSTO RESEARCH LIBRARY THESAURUS

Hazard analysis, Risk assessment, Risk mitigation, Crew environments, Modelling, Survivability

19. ABSTRACT

A number of combat vehicles carry their propelling charges and high explosive filled projectiles inside the crew compartment. Such arrangements give rise to questions about the prospects of crew survival in an unplanned munitions initiation event owing to co-habitation of the crew with an on-board magazine. DSTO has undertaken an experimental study to investigate this concern. A trials structure was developed whereby a a range of propelling charge types and storage configurations were initiated in a simulated military vehicle crew compartment. The trials structure was fitted out with simulated personnel instrumented to enable the threats from the thermal, ejecta and pressure environment created by the propelling charge event to be assessed. The trial results indicated that the thermal and ejecta threats posed the greatest risk to crew survival. The effectiveness of a range of hazard mitigation techniques was also assessed and this is addressed in Part 2 of this report.